Physics of the Earth and Planetary Interiors 202-203 (2012) 27–55

Contents lists available at SciVerse ScienceDirect

Physics of the Earth and Planetary Interiors

journal homepage: www.elsevier.com/locate/pepi

Mechanisms for the generation of plate tectonics by two-phase grain-damage and pinning

David Bercovici [a,*], Yanick Ricard [b]

[a] Yale University, Department of Geology & Geophysics, New Haven, CT, USA
[b] Laboratoire des Sciences de la Terre, CNRS, ENS, Université de Lyon, Lyon, France

ARTICLE INFO

Article history:
Received 7 August 2011
Received in revised form 17 May 2012
Accepted 18 May 2012
Available online 30 May 2012
Edited by Mark Jellinek

Keywords:
Plate generation
Mantle convection
Damage mechanics

ABSTRACT

Weakening and shear localization in the lithosphere are essential ingredients for understanding how and whether plate tectonics is generated from mantle convection on terrestrial planets. We present a new theoretical model for the mechanism of lithospheric weakening and shear-localization and hence plate generation through damage, grain evolution and Zener pinning in two-phase (polycrystalline) lithospheric rocks. Grain size evolves through the competition of coarsening, which drives grain growth, with damage, which drives grain reduction. However, in a two-phase medium the interface between phases induces Zener pinning, which impedes grain growth and facilitates damage. The size of the pinning surfaces is given by the roughness of the interface, and damage to the interface causes smaller pinning surfaces, which in turn drive down the grain-size, forcing the rheology into the grain-size-dependent diffusion creep regime. This process allows damage and rheological weakening to co-exist, which is normally considered impossible in single phase assemblages. Moreover pinning greatly inhibits grain-growth and shear-zone healing, which is much faster in single phase materials. Hence, the resulting shear-localization is rapid (less than 1 Myr), but the healing time for a dormant weak zone is very slow (greater than 100 Myrs); these effects therefore permit rapidly forming and long-lived plate boundaries. The model therefore provides a key ingredient and predictive theory for the generation of plate tectonics on Earth and other planets.

1. Introduction

The unique occurrence of plate tectonics on Earth amongst all terrestrial planets in our solar system is one of the major enigmas in Earth and planetary science. Although it is now widely recognized that plate tectonics is an expression of mantle convection – wherein subducting slabs both drive plates and cool the planet (Davies and Richards, 1992; Bercovici, 2003) – how plate tectonics arises self-consistently from convective motions has been the subject of study for over 30 years (e.g., Kaula, 1980; Hager and O'Connell, 1979, 1981; Ricard and Vigny, 1989; Vigny et al., 1991; Bercovici, 1993, 1995; Tackley, 1998, 2000b,c; Bercovici and Ricard, 2005; van Heck and Tackley, 2008; Foley and Becker, 2009); see reviews by Bercovici et al. (2000), Gurnis et al. (2000), Tackley (2000a) and Bercovici (2003). Even with significant progress, a comprehensive theory to explain the generation of plate tectonics has yet to be achieved.

That Earth has plate tectonics but her ostensible twin Venus does not has been one of the key mysteries in the plate-generation problem, and it has motivated much speculation about planetary conditions, including the requirement of liquid water, for plate tectonics to exist. While a traditional view has been that water lubricates plates by, for example, introduction of sediments at subduction zones or serpentinization along faults (e.g., Tozer, 1985; Lenardic and Kaula, 1994; Korenaga, 2007; Hilairet et al., 2007), the Earth's lithosphere might be as dry as that of Venus, because of dehydration melting at ridges (Hirth and Kohlstedt, 1996); this has lead some to speculate that water's role is in keeping Earth's surface temperature cool enough to permit plate boundary formation by failure (Lenardic et al., 2008) or damage (Landuyt and Bercovici, 2009b). That plate tectonics is also presumed to be a necessary condition for a temperate climate – by the negative carbon dioxide feedbacks associated with erosion, weathering and volcanism (Walker et al., 1981) – implies that a habitable climate and plate tectonics are mutually required. Plate tectonics may also be necessary for the existence of life by providing a source of thermodynamic disequilibrium through continuous recycling of the surface (e.g., Southam and Westall, 2007; Martin et al., 2008). The discovery of many terrestrial planets in other solar systems over the last fifteen years (e.g., Charbonneau et al., 2009) has, therefore, emphasized the importance of understanding the conditions for plate tectonics as one (although perhaps not a unique)

* Corresponding author. Tel.: +1 2034323168.
E-mail addresses: david.bercovici@yale.edu (D. Bercovici), yanick.ricard@ens-lyon.fr (Y. Ricard).

0031-9201/$ - see front matter © 2012 Elsevier B.V. All rights reserved.
http://dx.doi.org/10.1016/j.pepi.2012.05.003

requirement for liquid water and presumed habitability. Of course the only readily available observation of terrestrial exo-planets is their mass, which has caused some debate as to whether size is more or less conducive to plate tectonics (Valencia et al., 2007; Valencia and O'Connell, 2009; O'Neill and Lenardic, 2007), although recent studies suggest that other factors such as surface conditions are equally or more important (Korenaga, 2010; van Heck and Tackley, 2011; Foley et al., 2012), which corresponds to the Earth-Venus comparison. However, this debate has highlighted the importance of understanding the physics of plate generation in order to predict how planetary conditions facilitate or inhibit plate tectonic formation.

The primary candidates for predictive theories of plate generation essentially belong to two classes, that from some perspectives are not so far from each other. First, a widely used approach is the "plasticity" formalism in which plates are assumed to be generated – i.e., an otherwise cold and strong lithosphere develops weak plate boundaries – when convective stresses exceed a certain yield stress (e.g., Trompert and Hansen, 1998; Tackley, 2000b; Richards et al., 2001; Stein et al., 2004; van Heck and Tackley, 2008; Foley and Becker, 2009). While this method is computationally facile, it requires an unusually low yield-stress (relative to the known strength of rocks). Furthermore, the plasticity method only allows plate boundaries to form so long as they are being deformed and are above the yield stress, and thus it does not produce one of the major observations of plate tectonics: dormant plate boundaries which are long-lived and can be re-activated (Gurnis et al., 2000), and are thus probably key to initiation of new subduction zones in cold lithosphere (Toth and Gurnis, 1998; Lebrun et al., 2003; Hall et al., 2003).

The other method of plate generation is to presume that plate boundaries are the sites of damage zones that undergo shear-localization and weakening during deformation, and that subsequent material damage survives for geologically extensive periods even after deformation ceases (Bercovici, 1998; Tackley, 2000c; Bercovici et al., 2001a,b; Auth et al., 2003; Bercovici and Ricard, 2003; Bercovici and Ricard, 2005; Ricard and Bercovici, 2003, 2009; Landuyt et al., 2008; Landuyt and Bercovici, 2009a; Rozel et al., 2011). Given the need for deep lithospheric shear localization, simple brittle failure and/or weakening by fluid pore pressure are implausible. Observations of localized shear in mantle peridotites, i.e., mylonites, where extensive grain-size reduction has occured (White et al., 1980; Etheridge and Wilkie, 1979; Jin et al., 1998; Furusho and Kanagawa, 1999) has prompted much activity in exploring grain-size shear-localizing feedback mechanisms (e.g., Kameyama et al., 1997; Braun et al., 1999; Montési and Hirth, 2003). In this case the self-weakening positive feedback occurs because of the interaction of grain-size dependent rheologies (such as diffusion creep or grain-boundary sliding; see Hirth and Kohlstedt (2003)) and grain-reduction driven by deformation through dynamic recrystallization (e.g., Karato et al., 1980; Urai et al., 1986; Derby and Ashby, 1987; Doherty et al., 1997; Shimizu, 1998; Lee et al., 2002).

However, this localizing feedback mechanism is problematic for several reasons. First, grain-reduction by recrystallization is coincident with dislocation creep while rheological softening by grain-reduction occurs in other creep mechanisms like diffusion creep (Etheridge and Wilkie, 1979; De Bresser et al., 1998, 2001) (c.f. Faul et al., 2011); thus the necessary components of the feedback mechanism ostensibly occur in exclusive domains of deformation space (e.g., on a stress-grain-size deformation map). This problem has recently been examined by considering the evolution of grain-size distributions wherein a rock sample has a mixture of rheological mechanisms simultaneously occuring, e.g., dislocation creep in large grains and diffusion creep for smaller grains (Ricard and Bercovici, 2009; Rozel et al., 2011); however, even here localization appears to be weak because eventually the grain-size distribution will evolve mostly to one region of deformation space or the other hence mitigating any feedback.

Second, while the physics of recrystallization is understood from experiments on the microscopic scale and is known to be associated with the propagation of dislocations and development of subgrains leading to subgrain rotation, the macroscopic expression of recrystallization in the evolution of mean-grain-size is not always well articulated and usually based on empirical relationships for how strain-rate drives dislocation density (e.g., Karato et al., 1980; Bercovici and Karato, 2003; Montési and Hirth, 2003) although this is not necessarily drawn from physical conservation laws. However, thermodynamic considerations from damage theory suggest that grain-size reduction invariably entails an increase in surface free energy, which is drawn from deformational work (Bercovici and Ricard, 2005; Landuyt et al., 2008; Ricard and Bercovici, 2009; Rozel et al., 2011) and this has been verified with experiments and the "paleowattmeter" relations of Austin and Evans (2007).

Finally, while localization due to grain-reduction causes material damage with some history and longevity, grain-growth by coarsening (e.g., Lifshitz and Slyozov, 1961; Hillert, 1965; Atkinson, 1988) and hence healing of weak zones in single mineral or single-phase systems is quite fast (Karato, 1989). Indeed, using parameters for grain-growth tabulated in Rozel et al. (2011) for 1 mm grains at 1000 K temperature, erasure of fine-grained weak zones in the lower lithosphere would occur in less than a million years.

These problems with grain-size weaking mechanisms have been a major barrier to progress on understanding lithospheric localization and plate generation. However, many of these problems are due to the assumption of single-phase mineral assemblages, whereas actual lithosphere is at least two major components or phases, i.e., while peridotite is mostly olivine (about 60% by volume) it has a major second component of pyroxene. Secondary phases are known to retard grain-growth and coarsening because of the impedance of grain-boundary migration by secondary phase obstructions (e.g., Herwegh et al., 2005; Warren and Hirth, 2006; Mehl and Hirth, 2008), otherwise known as Zener pinning (Smith, 1948). Zener pining itself is an active area of metallurgical research because of its control on grain evolution and recrystallization (e.g., Doherty et al., 1997; Manohar et al., 1998; Couturier et al., 2003; Harun et al., 2006; Roberts, 2008, and references therein).

In this paper we examine grain growth and damage in a two-phase material such as peridotite; we hypothesize that the interaction (e.g., via Zener pinning) between grain evolution and the evolution of pinning surfaces and/or inclusions is key to lithospheric localization and plate generation. The size and shape of pinning surfaces are represented generically by the interface between phases, which is implicitly the surface obstructing grain boundary migration. The density of interfacial area (i.e., interface area per unit volume) is a proxy for the concentration of pinning surfaces that obstruct grain growth. More specifically, the interface density is a measure of the dispersal of the phases or mixture homogeneity. If the mixture were completely segregated such that the phases were separated by one continuous and smooth (flat or spherical) interface, then the interface area density would be minimal and there would be no pinning of grains within each phase. However if one phase were dispersed through the mixture in tiny inclusions then interface area density approaches its maximum value (being the dissolution limit), in which case pinning of the other phase's grains would be prevalent.

Therefore, if the interface between phases undergoes deformation, stretching and break-up by damage (e.g., Holyoke et al., 2006; Skemer et al., 2009), then interface area density and curvature are increased (e.g., smaller inclusions; see Fig. 1). The greater concentration of obstructing surfaces pins or constrains the mineral grains

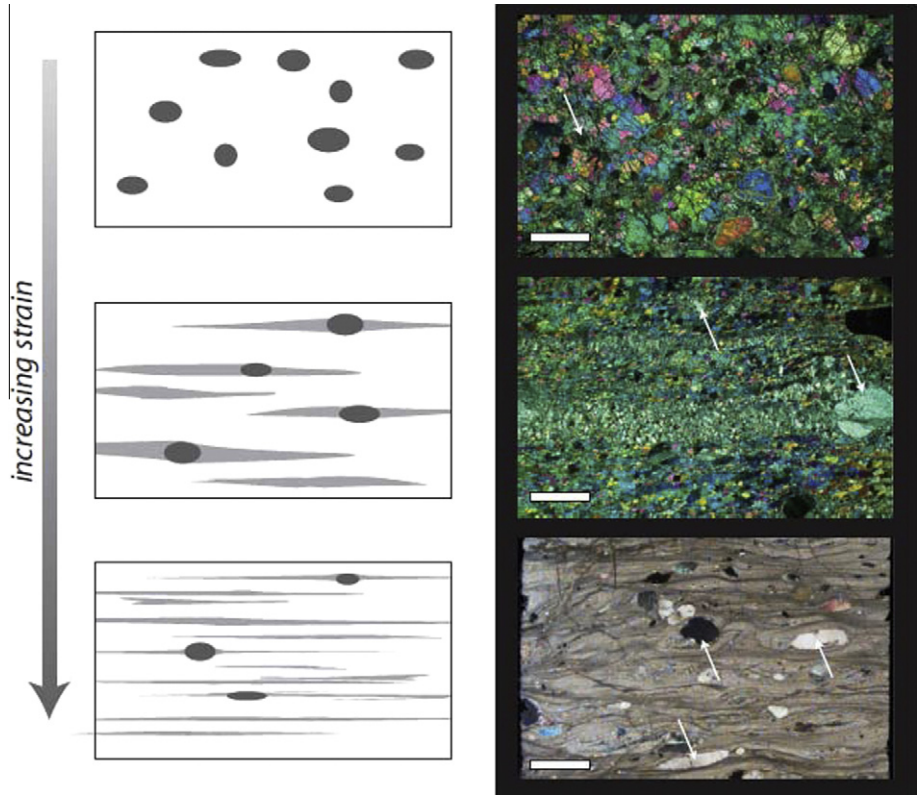

Fig. 1. A sketch, left column, from (Skemer et al. (2009), Fig. 7) of deformation of a peridotitic mylonite of an olivine phase (white) surrounding a secondary orthopyroxene phase (grey). With increasing deformation and shear (indicated on the far left), the orthopyroxene porphyroclasts or inclusions of multiple grains are deformed and even disaggregated into sharper features and smaller inclusions, as well as mixed and dispersed through the primary olivine phase. Deformation initially drives grainsize reduction for large grains in both phases by dynamic recrystallization. However, deformation, shearing and mixing also increase the complexity and curvature of the interface between the two phases (i.e., they drive "interface damage"), which facilitates Zener pinning of grains. The resulting pinning not only retards grain growth but can, as theorized in this paper, facilitate grain-damage and even reverse coarsening. Corresponding examples of natural assemblages are shown in micrographs in the right column (white arrows indicate corresponding orthopyroxene porphyroclasts or inclusions) with the top two frames from Skemer et al. (2009) and the bottom one from Warren and Hirth (2006).

to ever smaller sizes, which forces the rheology to remain in diffusion creep (also experimentally inferred by, Etheridge and Wilkie, 1979; Warren and Hirth, 2006; Mehl and Hirth, 2008), while also blocking grain growth. This mechanism therefore potentially solves two major obstacles to grain-damage theory: (1) it allows damage and grain-reduction to occur simultaneously with grain-size weakening and (2) grain growth and healing are greatly slowed down if not blocked entirely by interfacial barriers, thereby leading to long-lived dormant weak zones. While the concept that Zener pinning imposes permanent diffusion creep while blocking grain growth is well known, the new but necessary ingredient needed to permit the localization feedback is that damage occurs directly to the interface and inclusions, which indirectly (e.g., through pinning) drives grain-size reduction.

We therefore develop a continuum theory for grain evolution in a two-phase deformable medium, allowing for the interaction between inclusion (i.e., interface area) and grain evolution through Zener pinning. This paper combines the two-phase theory of compaction and damage of Bercovici et al. (2001a), Ricard et al. (2001), Bercovici et al. (2001b), Bercovici and Ricard (2003) and Ricard and Bercovici (2003), and the two-phase treatment of grain-damage of Bercovici and Ricard (2005), Landuyt et al. (2008) and Landuyt and Bercovici (2009a) with the grain-evolution and damage theory of Ricard and Bercovici (2009) and Rozel et al. (2011). Although the physics of the system is intrinsically complex, we use the self-similarity assumptions of Rozel et al. (2011) to develop a final simple theory that involves a few new coupled evolution equations for grain-size and interface curvature. This theory is compared to grain-growth experiments and applied to some simple-shear test cases to examine (1) the implied effective rheology, and whether it permits weakening and localization, and (2) the evolution of a damaged zone during deformation (i.e., to examine the rapidity of plate boundary formation) and after deformation ceases (i.e., to test plate boundary longevity after dormancy). Although more experimental research is needed to better understand interface growth and damage, the essential physics robustly demonstrates that localization and plate-boundary formation via this mechanism is significant, rapid and semi-permanent.

2. Model

The theoretical model of a two-phase grained continuum undergoing damage as well as Zener pinning at the interface between phases is developed completely in Appendices A–G. However, we describe here the essence of the model and provide the simplest set of governing equations that can be used to compare to experiments and for geodynamic applications.

2.1. Phases, grains and interfaces

The two-phase grained continuum is representative of, for example, mantle peridotite made of olivine and pyroxene minerals. The two phases are of comparable (though not identical) densities, viscosities and other properties, which are combined into a non-dilute mixture (e.g., 60%–40% mixture by volume). Phases are denoted by the subscript i where $i = 1$ or 2. For example the phase volume fractions are ϕ_i where $\sum_i \phi_i = 1$; since the volume fractions are

dependent (i.e., $\phi_2 = 1 - \phi_1$) we will often refer to just one fraction $\phi = \phi_1$, which we usually ascribe to the volume fraction of the minor phase (e.g., ϕ is the pyroxene volume fraction, and $1 - \phi$, the olivine one; see also Appendix A).

The phases are also assumed to be grained materials with unique grain-size distributions. The generic grain-size is denoted by R, which acts as the independent variable in "grain-size space", and each phase's grain-size distribution defines an average grain-size $\mathcal{R}_i$. The grains of each phase evolve separately through the competition between surface-tension driven coarsening, which acts to increase grain-size, and damage (i.e., the application of deformational work toward creating new grain boundary area and energy), which acts to reduce grain-size. The continuum grain-growth theory for a single phase is thoroughly described by Ricard and Bercovici (2009) and Rozel et al. (2011), and the two-phase derivation is presented in Appendices B–E.

The phases are separated by an interface, which we assume to be isotropic, and is thus described by a scalar interface density α, i.e., the interfacial area per unit volume of the mixture (Bercovici et al., 2001a). The interface density is associated with the interface morphology, and in particular a characteristic coarseness, or radius of curvature of the interface r such that $\alpha \sim 1/r$; i.e., for a given mixture, the more tortuous, distorted or disaggregated its interface, the smaller will be the interface coarseness r and the larger will be the interface density α (see Fig. 2). Moreover, damage is also applied to the interface wherein deformational work creates more interface area and energy by, for example, rending, stretching and stirring.

Finally, both grain growth and grain damage are affected by the interface between phases, which acts like a blocking or pinning surface that limits grain growth and distorts the grain boundaries. (The pinning effects are described qualitatively below in Section 2.2 and more thoroughly in Appendix C.) Most importantly, damage to the interface causes ever finer pinning surfaces, which in turn drive grains to smaller sizes (by both reversing coarsening and enhancing damage), and into a permanent diffusion creep regime. Therefore damage to the interface forces grain-size reduction to occur simultaneously with diffusion creep and associated grain-size-dependent viscosity, which leads to a strong shear-localizing feedback mechanism.

2.2. Zener pinning

As grain boundaries in either phase move (e.g., by grain growth) they can impinge on the interface between phases, which acts as a barrier that pins the grain boundary. The pinning is caused because the deflection of the grain boundary around an obstruction creates more grain boundary area and surface energy and thus requires extra work to move the grain boundary past the obstacle. The interfacial density α and related interface curvature $1/r$ determine the extent of grain boundary pinning; indeed the characteristic radius of curvature r of the interface can be treated as a proxy for obstacle size (see Appendix A).

2.2.1. Zener pinning force

The classical relation for pinning force was derived by Zener as reported by Smith (1948) for a flat grain boundary of one phase moving and impinging on a small inclusion of the other phase (Fig. 3); since then the theory has been developed and explored at length to adjust some of the original simplifying assumptions (e.g., Hellman and Hillert, 1975; Wörner and Cabo, 1987; Rios, 1987; Hillert, 1988; Harun et al., 2006; Roberts, 2008). In the simplest case, the net surface tension force of a single spherical inclusion of size r pulling normal to the grain boundary and thereby pinning it, is

$$f_n = \gamma_i 2\pi r \cos\theta \sin\theta \tag{1}$$

where γ_i is the grain-boundary surface tension in phase i and θ is defined in Fig. 3 (see also Appendix C). The net force due to an ensemble of such inclusions touching the grain-boundary of area $\breve{A} = 4\pi R^2$ is shown in Appendix C to have the form of

$$F_n = \frac{3\gamma_i(1-\phi_i)\breve{A}}{2r}\mathcal{P}(R/r) \tag{2}$$

where $\mathcal{P}(U)$ is a positive and monotonically increasing function, and any quantity accented like $\breve{Q}$ is specific to a grain of size R. Although this force relation has been derived assuming that pinning is due to small particles or impurities on the grain boundaries, it is also basically applicable to pinning in assemblages of minerals with comparable volume fractions and grain-sizes (see Appendices C.3 and G.2).

2.2.2. Grain boundary distortion

As shown in Appendix C.2, the work done in changing grain-size against this pinning force can be used to infer the distortional effects of Zener pinning. For example, with pinning and resultant distortion, the effective grain-boundary curvature and surface area become, respectively,

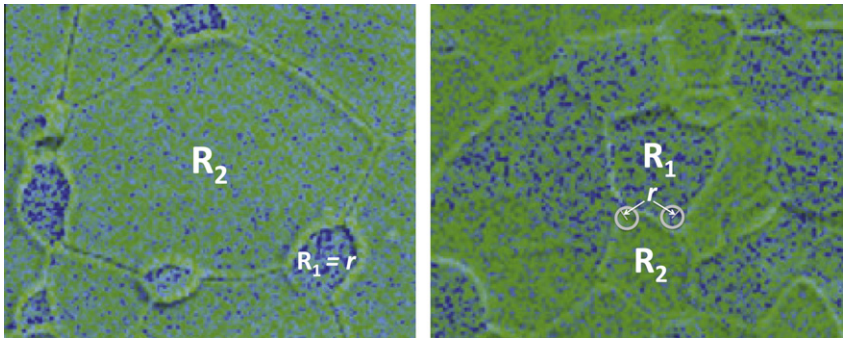

Fig. 2. A sketch, showing interpretations of grainsize R and interface coarseness or radius of curvature r on micrographs of synthetic peridotites from Hiraga et al. (2010). The left panel shows a mixture of 91% forsterite (green [light grey]) in which the grainsize is $R = R_2$, and 9% enstatite (blue [dark grey]) in which $R = R_1$ (adapted from, Hiraga et al. (2010), Fig. 2b); in this case the grains are dispersed, r is essentially equal to the grainsize of the minor phase R_1, and Zener pinning occurs more through the classical mechanism of small particles pinning a large grain boundary (see Appendix C.1). The right panel is for a mixture of 42% enstatite and 58% forsterite (adapted from, Hiraga et al. (2010), Fig. 2f) in which grains are clustered and r is mostly set by the maximum curvature on the interface that occurs through distortions; in this case distortions and pinning occur by grain-boundary splitting (see Appendix C.3). The scale of both frames is approximately 5 μm. (For interpretation of the references to colour in this figure legend, the reader is referred to the web version of this article.)

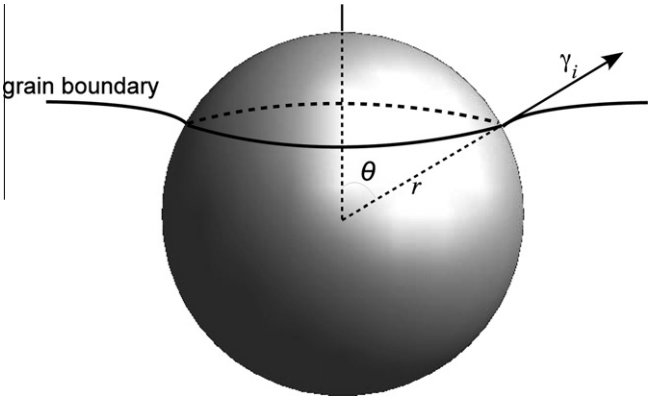

Fig. 3. Sketch of Zener pinning configuration in which a grain boundary of one phase moves past an inclusion composed of the other phase. The surface tension of the grain boundary γ_i acts on the intersection between the inclusion and the grain boundary. See Appendix C, and in particular Fig. C.1, for more detailed development.

$$\breve{\mathcal{C}}_i = \frac{2}{\mathsf{R}} + \frac{3(1-\phi_i)}{2r}\mathcal{P}(\mathsf{R}/r) \tag{3a}$$

$$\breve{\mathcal{A}}_i = \breve{\mathsf{A}} + \frac{3(1-\phi_i)}{2r}\int_0^{\mathsf{R}} \mathcal{P}(\mathsf{R}'/r)\breve{\mathsf{A}}'d\mathsf{R}' \tag{3b}$$

Thus as R/r becomes large, grains become more distorted and thus have increasing effective curvature and surface area. Moreover, the pinning effect implies that bigger grains are more distorted than smaller ones (for a given r), which has a profound influence on both grain growth and damage. In particular, coarsening is normally driven by small grains with large curvature, and hence large internal pressure and chemical potential, diffusing mass into large grains with smaller curvature (thus large grains grow at the expense of small ones). However, with pinning, large grains are more distorted than smaller ones, thus the contrast in curvature and chemical potential is reduced and mass diffusion retarded; if the large grains are severely distorted (e.g., by pinning surfaces with very small r) then the curvature contrast and direction of diffusion can be reversed causing grain reduction instead (small grains grow at the expense of large ones). Likewise, damage to grains also depends on the contrast in surface energy between a large grain before induced damage and fission, and that of the multiple grains after fission. Since multiple grains have more surface area than the single grain of the same net volume, the change in surface energy during fission requires energy, which is obtained from deformational work. However, if pinning and distortion increase the large grain's surface area more than it does for the multiple smaller grains, then the energy contrast is smaller, hence less deformational work is required to induce fission and thus damage is facilitated. These grain-boundary distortion effects appear as a Zener pinning factor in the grain-growth law, which thus couples grain evolution to the evolution of interface curvature, both of which are affected by damage.

2.3. Governing equations

The theoretical model is developed fully in the Appendices, but we summarize the essential equations here. Although the model is derived for a general viscous two-phase mixture with a general grain-size distribution in each phase, the final governing equations involve two key assumptions. First, since both mineral phases are solid-state their relative motion is likely to be negligible and thus at a given point in space we assume they have the same velocity $\mathbf{v}$. Second, as done by Rozel et al. (2011), we assume the grain-size distribution is close to a self-similar distribution in that it always retains the same shape and its mean, variance and amplitude are uniquely determined by a characteristic grain-size $\mathcal{R}_i$ in each phase i.

The essential governing equations for our two-phased continuum with grain-damage and Zener pinning are

$$\frac{\partial\phi}{\partial t} + \mathbf{v}\cdot\boldsymbol{\nabla}\phi = 0 \quad \text{and} \quad \boldsymbol{\nabla}\cdot\mathbf{v} = 0 \quad \text{mass conservation} \tag{4a}$$

$$0 = -\boldsymbol{\nabla}\overline{\Pi} + \boldsymbol{\nabla}\cdot\bar{\underline{\boldsymbol{\tau}}} + \bar{\rho}\mathbf{g} + \boldsymbol{\nabla}(\gamma_{\mathrm{I}}\alpha) \quad \text{momentum conservation} \tag{4b}$$

$$\underline{\dot{\boldsymbol{\varepsilon}}} = \left(a_i\tau_i^{n-1} + \frac{\lambda_{3-m}}{\lambda_3}\frac{b_i}{\mathcal{R}_i^m}\right)\underline{\boldsymbol{\tau}}_i \quad \text{rheological law} \tag{4c}$$

$$\frac{Dr}{Dt} = \frac{\eta G_{\mathrm{I}}}{qr^{q-1}} - \frac{\mathrm{f}_{\mathrm{I}} r^2}{\gamma_{\mathrm{I}}\eta}\overline{\Psi} \quad \text{interface curvature evolution} \tag{4d}$$

$$\frac{D\mathcal{R}_i}{Dt} = \frac{G_i}{p\mathcal{R}_i^{p-1}}\mathcal{Z}_i - \frac{\lambda_3}{\lambda_2}\frac{\mathcal{R}_i^2}{3\gamma_i}\mathrm{f}_{\mathrm{G}}(1-\mathrm{f}_{\mathrm{I}})\Psi_i\mathcal{Z}_i^{-1} \quad \text{grain-size evolution} \tag{4e}$$

where ρ_i, Π_i, and $\underline{\boldsymbol{\tau}}_i$ are the density (assumed constant), effective pressure (including the effect of grain-boundary surface tension) and deviatoric stress tensor of each phase, respectively, and the volume average of any quantity q is defined as $\bar{q} = \sum_i \phi_i q_i$. Moreover, γ_i is the surface tension on the boundary between grains of the same phase, γ_{I} is the interface surface tension (i.e., on the boundary between grains of different phases), and the interface area density (interface area per unit volume) α is given by

$$\alpha = \frac{\eta(\phi)}{r} \tag{5}$$

where $\eta(\phi)$ is a function that vanishes at $\phi = 0$ and 1 (e.g., for spherical inclusions, $\eta = 3\phi_1\phi_2 = 3\phi(1-\phi)$); see Appendix A. The constitutive law relation (4c) between stress $\underline{\boldsymbol{\tau}}_i$ and strain-rate

$$\underline{\dot{\boldsymbol{\varepsilon}}} = \frac{1}{2}(\boldsymbol{\nabla}\mathbf{v} + [\boldsymbol{\nabla}\mathbf{v}]^{\dagger}) \tag{6}$$

is a composite rheology describing dominance of dislocation creep at large grain-sizes and the prevalence of diffusion creep at small grain-sizes; the coefficients a_i and b_i are rheological compliance coefficients for phase i (see Appendix F.7).

The evolution equations for interface roughness (or radius of curvature) r and mean grain-size $\mathcal{R}_i$, (4d) and (4e), describe the competition between coarsening and damage (first and last terms on the right side of each equation, respectively). Coarsening represents the tendency toward minimum surface energy by increasing grain-size and/or interface coarseness, while damage represents the storage of deformational work as surface energy by grain reduction and/or interface rending and distortion. The coarsening terms contain various coefficients including growth rate constants G_i and G_{I} and exponents p and q. The damage terms involve the partition fraction f_{I} of deformational work going to create new interface area and energy; f_{G} is the remaining fraction of work going to create grain-boundary area and energy; and $\Psi_i = \boldsymbol{\nabla}\mathbf{v} : \tau_i$ is the deformational work on phase i and $\overline{\Psi} = \sum_i \phi_i\Psi_i = \boldsymbol{\nabla}\mathbf{v} : \bar{\tau}$. However, as stipulated by dynamic recrystallization theory, damage to grains only occurs in the fraction of the medium that is deforming by dislocation creep, which is prescribed by defining

$$\mathrm{f}_{\mathrm{G}} = \mathrm{f}_{\mathrm{G}}^{*}\left(1 + \frac{\lambda_{3-m}b_i}{\lambda_3 a_i\mathcal{R}_i^m\tau_i^{n-1}}\right)^{-1} \tag{7}$$

(see Appendix F.7). Damage to the interface does not necessarily follow this constraint since the interface can still be distorted and disaggregated even if the phases undergo diffusion creep.

Perhaps most significantly, the grain-size evolution equation contains the Zener pinning factor (see below Section 2.4)

$$\mathcal{Z}_i = 1 - c_{\mathrm{n}}(1-\phi_i)\left(\frac{\mathcal{R}_i}{r}\right)^{\mathrm{n}+1} \quad \text{where} \quad c_{\mathrm{n}} = \frac{3\mathrm{b}_{\mathrm{n}}\lambda_{\mathrm{n}+3}}{2(\mathrm{n}+3)\lambda_2} \tag{8}$$

and n and $\mathrm{b_n}$ are constants in the relation for the function $\mathcal{P}(\mathrm{R}/r)$ (see Appendix F.4).

Finally, several of the governing equations contain the factor λ_n, which is the nth moment of the normalized grain-size distribution (see (F.8)) but is simply $\lambda_n = e^{n^2\sigma^2/2}$ for a log-normal distribution (where we assume a dimensionless variance $\sigma = 0.8$); see Appendix F.6.

2.4. Influence of Zener pinning

The role of the Zener pinning factor $\mathcal{Z}_i$ appearing twice in the grain evolution law, (4e), warrants discussion. Similar Zener pinning factors have been noted in prior studies on grain-growth (see Harun et al., 2006; Roberts, 2008, and references therein); the effect of $\mathcal{Z}_i$ on damage, however, has not been previously determined.

The presence of $\mathcal{Z}_i$ in the coarsening term, e.g., the first term on the right side of (4e), shows that grain growth is limited by interface coarseness r; this implies that as damage to the interface reduces r and thus increases interface area density α according to (4d), grain growth is increasingly limited to smaller sizes. Clearly small grains will be limited in growth by Zener pinning as $\mathcal{Z}_i \to 0$ in (4e), which occurs as they approach the size $r/[c_\mathrm{n}(1-\phi_i)]^{\frac{1}{\mathrm{n}+1}}$ (see (8)). However, grains that are larger than that size will, in principle, be driven to shrink because of Zener pinning effects. In particular, Zener pinning adds to the effective surface energy of a large grain by distorting its boundary and increasing its effective curvature (see (3)), which consequently increases the grains internal pressure or free energy (i.e., chemical potential). The Zener pinning effect is more profound for larger grains than smaller ones, thus it is possible for bigger grains to have larger effective curvature – and hence pressure and chemical potential – than smaller grains, thereby causing them to diffuse mass to the smaller grains and shrink. Thus Zener pinning potentially works to both limit grain growth for small grains as well as drive grain-size reduction for large grains. If r itself is reduced by damage then the grains are driven to shrink further.

The factor of $\mathcal{Z}_i^{-1}$ in the damage term (second on the right side of (4e)) implies that Zener pinning facilitates damage. This can be understood physically by considering the work needed to cause grain fission, which is equivalent to the surface energy created in splitting a grain into smaller grains. A large grain experiencing Zener pinning has excess surface energy (relative to the undistorted grain of the same size), and when it is split the resulting smaller grains have less Zener pinning force on them. Thus, the difference in energy before and after splitting is not as large with Zener pinning as without it, therefore less work is required to damage and split the grain.

Therefore, Zener pinning effects captured by the factor $\mathcal{Z}_i$ in the grain evolution relation (4e), act to both slow down grain growth and even diffusively shrink grains as well as enhance grain damage, especially as r is reduced and interfacial area density increased by damage according to (4d).

3. Comparison with grain-growth experiments

Hiraga et al. (2010) experimentally measured grain-growth in various synthetic mixtures of forsterite and enstatite, and the results of their study are directly relevant to our model. In particular, we can apply our grain-growth relations without deformation and damage to the experimental data and constrain the form of the Zener pinning factor $\mathcal{Z}_i$ as well as the interface coarsening parameters. The growth laws (4d) and (4e) without damage, and using the form of $\mathcal{Z}_i$ given by (8), lead to

$$\frac{\mathrm{d}r^q}{\mathrm{d}t} = \eta G_\mathrm{I} \tag{9}$$

$$\frac{\mathrm{d}\mathcal{R}_i^p}{\mathrm{d}t} = G_i\left[1 - c_\mathrm{n}(1-\phi_i)\left(\frac{\mathcal{R}_i}{r}\right)^{\mathrm{n}+1}\right] \tag{10}$$

The data for mean grain-sizes versus time for each phase in various mixtures are reproduced from Hiraga et al. (2010) in Table 1. Hiraga et al. (2010) assumed the grain-sizes followed a power-law evolution of the form $\mathcal{R}_i^p - \mathcal{R}_0^p = k_i t$, where $\mathcal{R}_0$ is the mean grain-size at $t = 0$ and k_i is a growth rate. These authors then inferred that $\mathcal{R}_i(t)$ flattened in time because of a large value of $p = 4$ or 5, and that the effect of pinning was manifest in a ϕ-dependent k_i. However, in the limit of a pure single phase system $\phi \to 0$, one should recover the classic value of $p = 2$, which would suggest that p is also ϕ dependent. We instead propose that, according to (9) and (10), the grain evolution undergoes normal grain growth with $p = 2$ when pinning is insignificant (when the grains are small or equivalently when $\mathcal{Z}_i \approx 1$), and then transition to much slower grain growth when pinning ensues (i.e., as $\mathcal{Z}_i \to 0$). Once pinning dominates, the grain growth is dictated by the growth of the pinning radius or coarseness r, which follows a growth rate $\eta G_\mathrm{I} \ll G_i$. In this case the grain growth curves would flatten not because $p \geqslant 4$ but because they are pinned to the slow growth of r. Moreover, the time to transition to a pinned state is dependent on ϕ, as is the interface coarsening rate ηG_i; thus different growth rates for different mixtures are readily accounted for by our model.

We can examine the nature of the asymptotic pinned state at relatively large times to constrain the form of the Zener pinning factor $\mathcal{Z}_i$, as well as infer the nature of the interface coarseness r since it is not directly measured in the experiments. Using these constraints we can then compare the full grain and interface evolution predicted by the model to the experiments.

3.1. The "pinned state" limit

We can test whether and when the pinned state is reached in the experiments for both phases by setting $\mathcal{Z}_i \approx 0$ in (8); eliminating r between the resulting equations for $i = 1$ and 2, we define the function

$$\mathcal{X}(t, \mathrm{n}, \phi) = \frac{\phi_1 \mathcal{R}_2^{\mathrm{n}+1}(t)}{\phi_2 \mathcal{R}_1^{\mathrm{n}+1}(t)} - 1 \tag{11}$$

Table 1
Data from Hiraga et al. (2010) for mean grainsize versus time of forsterite and enstatite in a synthetic peridotite mixture; ϕ is the volume fraction of enstatite, t is time in hours, and $\mathcal{R}_i$ is the mean grainsize in μm , where $i = 1$ indicates enstatite and $i = 2$ indicates forsterite.

t	$\phi \approx 0$		$\phi = 0.03$		$\phi = 0.09$		$\phi = 0.15$		$\phi = 0.24$		$\phi = 0.34$		$\phi = 0.42$	
	$\mathcal{R}_2$	$\mathcal{R}_1$	$\mathcal{R}_2$	$\mathcal{R}_1$	$\mathcal{R}_2$	$\mathcal{R}_1$	$\mathcal{R}_2$	$\mathcal{R}_1$	$\mathcal{R}_2$	$\mathcal{R}_1$	$\mathcal{R}_2$	$\mathcal{R}_1$	$\mathcal{R}_2$	$\mathcal{R}_1$
0	2.8	0	1.5	0.5	1.0	0.4	0.6	0.3	0.6	0.4	0.4	0.3	0.5	0.5
0.5	3.7	0	1.6	0.5	1.1	0.5	1.1	0.5	1.0	0.6	0.5	0.4	0.6	0.6
1	4.4	0	1.5	0.7	1.6	0.4	1.3	0.5	1.1	0.4	0.6	0.5	0.9	0.7
3	4.9	0	2.4	0.8	1.9	0.6	1.6	0.6	1.4	0.6	0.7	0.5	1.1	0.8
10	5.7	0	3.6	1.2	2.3	0.9	2.0	0.8	1.7	1.0	0.9	0.6	1.3	1.2
50	6.3	0	4.9	1.1	3.0	1.1	2.9	1.1	2.1	1.4	1.3	1.0	2.1	1.7

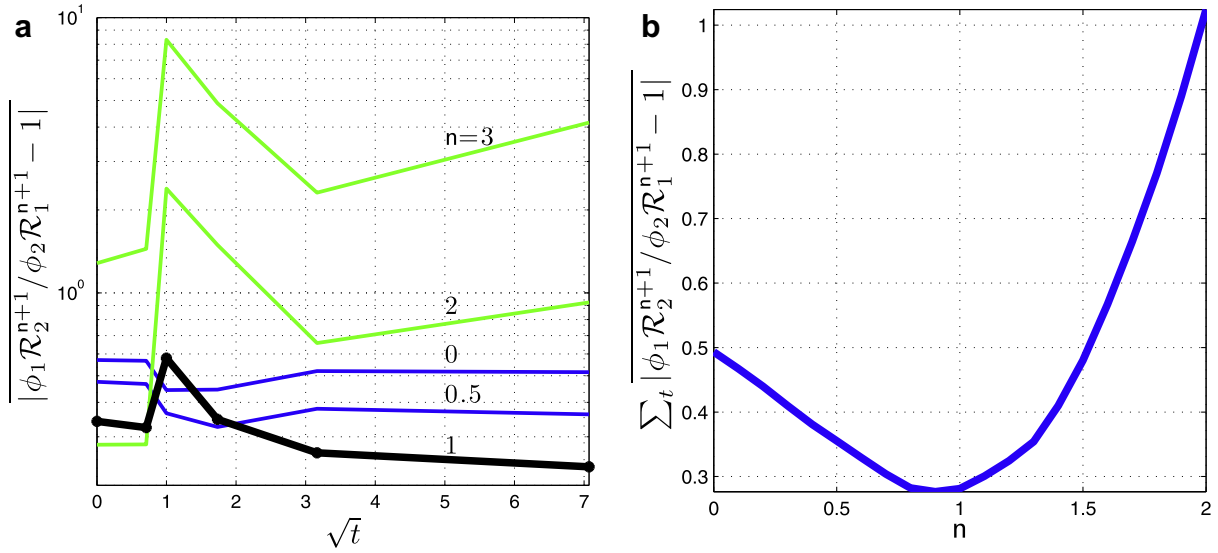

Fig. 4. A test of the pinned state conditions for which the Zener pinning factor defined in (8) reaches $\mathcal{Z}_i \approx 0$, or equivalently the function $\mathcal{X}$ defined in (11) goes to 0, in the experiments of Hiraga et al. (2010) as described in Section 3.1. Plots show (a) the value of $\mathcal{X}$ averaged over the experiments with different ϕ (excluding $\phi \approx 0$) versus time t (in hours) for different Zener factor exponents n defined in Section 8; and (b) the sum of this average value over the last three measured times ($t \geqslant 3$ h) versus n.

in which $\mathcal{X} = 0$ when $\mathcal{Z}_i = 0$ for both phases. The quantity $\mathcal{X}$ is unique to each experiment with a different volume fraction $\phi = \phi_1$ (see Table 1), as well as being a function of time t and the exponent n. We can examine the average $\mathcal{X}$ for all the experiments (excluding the case $\phi \approx 0$), $\overline{\mathcal{X}}$, through time and for various n (Fig. 4a) to infer that $\overline{\mathcal{X}} \to 0$ and hence $\mathcal{Z}_i \to 0$ for only the last 2 or 3 times in the experiment (i.e., $t \geqslant 3$ h), and only for $n \approx 1$. The sum of $\overline{\mathcal{X}}$ over the last 3 times in the experiments is only a function of n, and we indeed find $n \approx 1$ minimizes this quantity (Fig. 4b). Thus grain growth reaches the pinned limit of $\mathcal{Z}_i \to 0$ provided $n = 1$, and for sufficiently large times.

The experiments do not provide data on the coarseness r but we can deduce what the model should predict for r once the experiments reach the pinned state at large times. Again writing that $\mathcal{Z}_i \approx 0$ for $n = 1$, we determine that r^2 equals both $c_1\phi_2\mathcal{R}_1^2$ and $c_1\phi_1\mathcal{R}_2^2$, and thus its volume average is

$$\tilde{r} = \sqrt{c_1\phi_1\phi_2(\mathcal{R}_1^2 + \mathcal{R}_2^2)} \tag{12}$$

which we evaluate using the experimental data (Table 1) and compare to the full model evolution results discussed below (see Figs. 5–7, red curves).

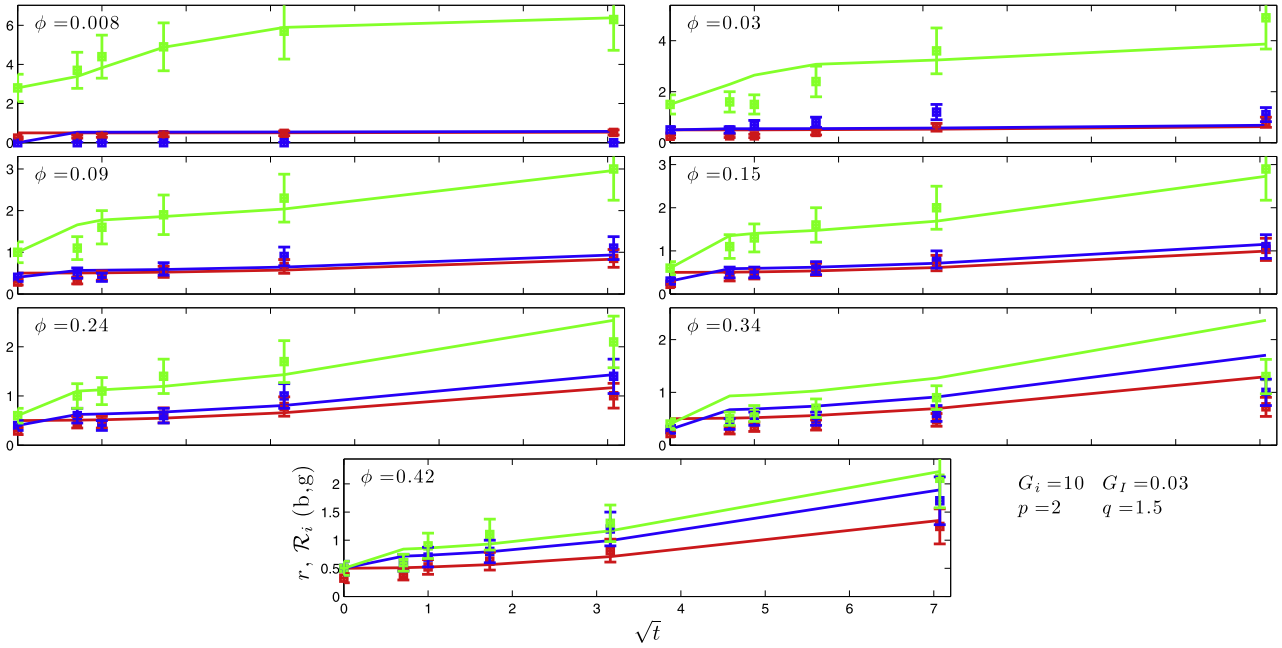

Fig. 5. A comparison of the theoretical model (curves) with the data (points) of Hiraga et al. (2010) as described in Section 3 for $q = 1.5$ and other parameters indicated. Green [light grey] is for the major phase (forsterite) grain-size $\mathcal{R}_2$, blue [dark grey] is for the minor phase (enstatite) grain-size $\mathcal{R}_1$, and red [medium grey] is for the interface coarseness r with data points $\tilde{r}$ inferred from (12). Note that r remains close to the minor phase grain-size $\mathcal{R}_1$ for small $\phi = \phi_1$, as expected, and is smaller than both grain-sizes for large ϕ. Grain-sizes and coarseness are in μm and time t is in hours. (For interpretation of the references to colour in this figure legend, the reader is referred to the web version of this article.)

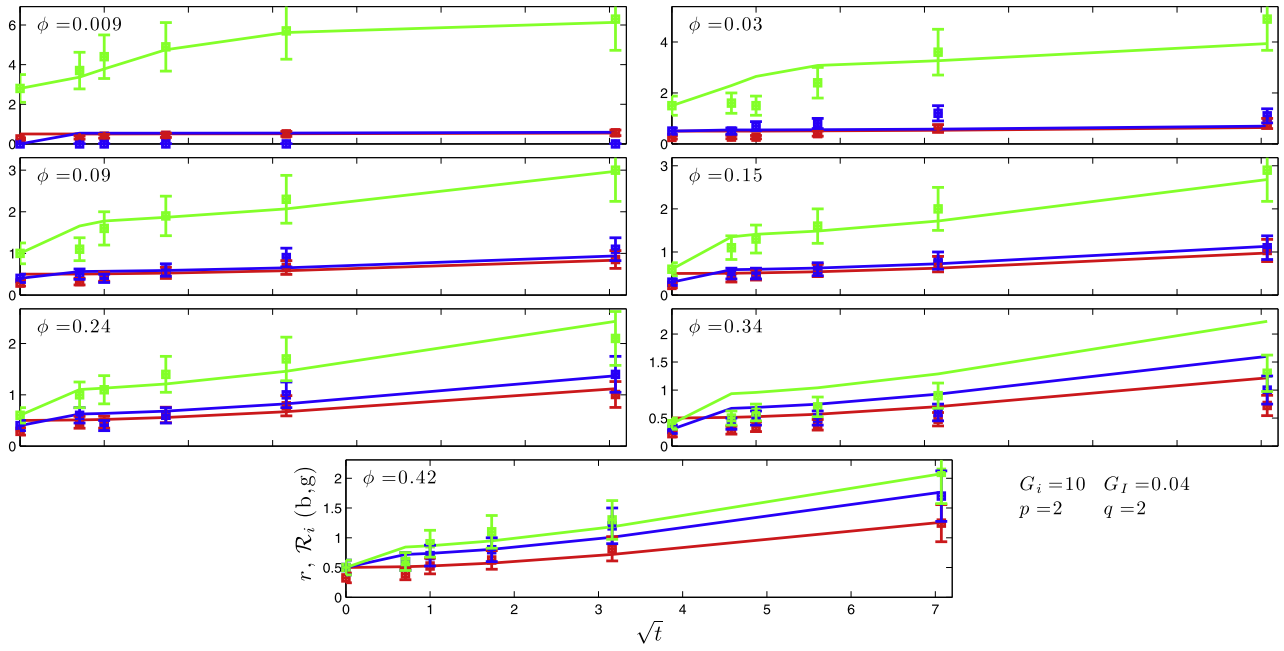

Fig. 6. Same as Fig. 5 except for $q = 2$, and other parameters indicated.

3.2. Full model comparison to experiments

We next compare model calculations for grain evolution with the experiments. We fix $n = 1$ and $p = 2$ and infer the basic grain-growth rate for the major phase $G_2 \approx 10\ \mu m^p/h$ from the experiment with $\phi \approx 0$ (i.e., $\phi_2 \approx 1$) at early times; we assume for simplicity that $G_1 \approx G_2$.

We integrate the model equations for the seven experimental volume fractions ϕ (see Table 1) for various G_i and q, assuming that $\eta = 3\phi_1\phi_2$. We use the experimental values of $\mathcal{R}_i$ at $t = 0$ for initial conditions, but then compare the model predictions to later experimental values.

Lacking data on the initial interface coarseness r, we integrate the model equations assuming r at $t = 0$ is comparable to a characteristic small grain-size, i.e., $r = 0.5\ \mu m$ at $t = 0$ for all cases. We can compare the model calculations for r to the inferred asymptotic data $\tilde{r}$ given in (12).

For the case of $\phi \approx 0$ the volume fraction of enstatite is not entirely zero (see Hiraga et al., 2010) and thus some pinning was seen to occur at later times; the value of ϕ in this case was below experimental resolution, thus we simply assume $\phi \leqslant 10^{-2}$ and adjust it slightly to match that experiment.

To infer possible values of q and G_i, we simply attempt to fit the model calculations to the "mantle peridotite" case of $\phi = 0.42$. We

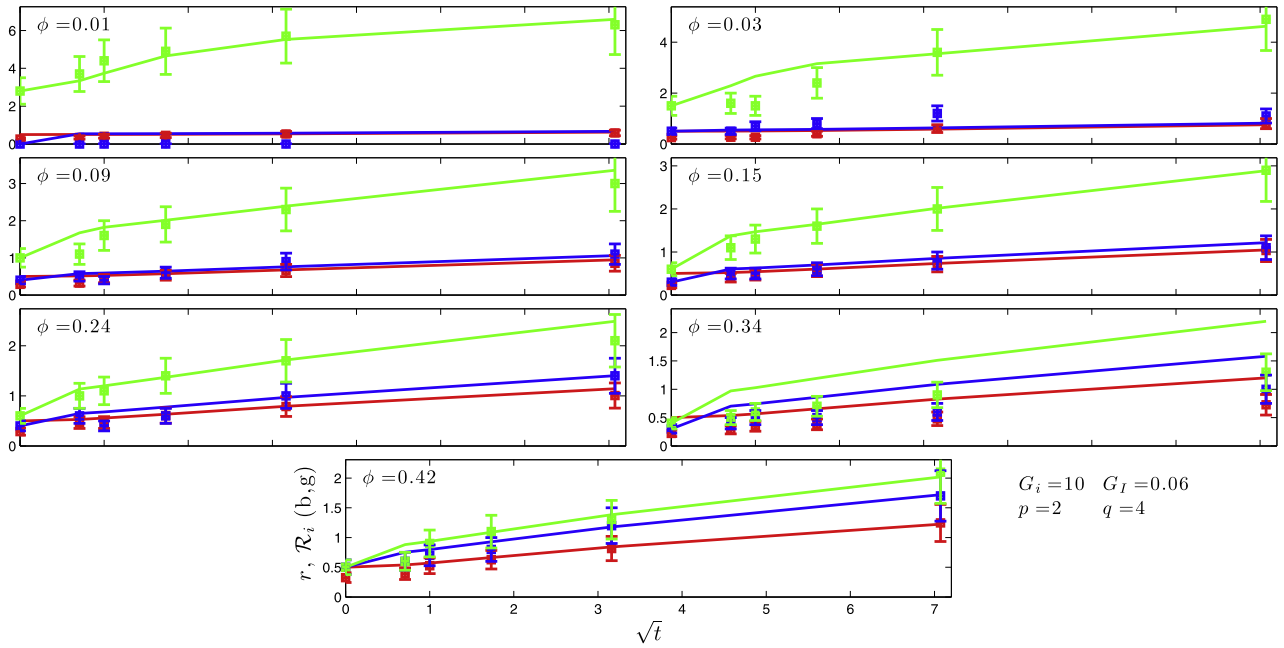

Fig. 7. Same as Fig. 5 except for $q = 4$, and other parameters indicated.

then use these parameters for all other cases to test the generality of the model. Thus, we do not try to minimize the misfit for all case, only the ones with lowest and highest ϕ. One could, of course, adjust other assumptions and parameters (e.g., the initial values of r) and provide closer fits to the experiments. However we only wish to see how well the model can predict the basic trends with the simplest assumptions, and what are the likely ranges of G_1 and q.

In comparing the model to the experimental data, we also approximate uncertainty in the experimental mean grain-sizes from the grain-size distributions (see Hiraga et al., 2010, Fig. 5). These distributions have nearly self-similar shapes, whose full half-widths (i.e., the full width of the distribution at half the amplitude) are approximately equal to the mean grain-size $\mathcal{R}_i$. Moreover, the scatter in the distribution peak (i.e., the location of the mode) is roughly over the $\mathcal{R}_i/2$. We thus assume that the uncertainty in the mean grainsize is $\pm\mathcal{R}_i/4$.

Figs. 5–7 display model versus experimental data for various G_1 and q. The best fitting curve is probably for $q = 4$ which would explain the inference that $p > 4$ by Hiraga et al. (2010), and this can be readily seen by fitting the pseudo-data for $\tilde{r}$ given by (12). However, the pinned state, and the dominance of the evolution in r, only occurs for the last 2 or 3 time steps, and given the additional uncertainty in the mean grain-sizes, other values of q are permissible, including values slightly less than 2 and as large as 5 or 6. Different values of q provide varying fits to the data for intermediate values of $0 < \phi < 0.42$; the fit to the data is reasonable for these intermediate cases except for the case $\phi = 0.34$, which no model is able to fit (at least, with our assumption that all experiments share the same initial r).

For each q, the values of G_1 are much smaller than G_i, although the exact value of G_1 depends slightly on q as is to be expected (given that q also determines the dimensions of G_1).

In the end, using the grain-growth model that allows for evolving pinning surfaces, we find that the same grain-growth parameters $G_i = 10\ \mu m^2/h$ and $p = 2$ can be used for all experiments with different ϕ, and that the slowing of grain-growth occurs as the system approaches the pinning limit, not because $p \geqslant 4$. The eventual grain-growth in both phases is governed by the interface evolution equation for r with $1.5 \leqslant q \leqslant 5$ (and $q = 4$ possibly being the best fit), and $G_1/G_i \leqslant 10^{-2}$.

Finally, we contend that extracting the normal growth parameters p and G_i from experiments with natural polycrystalline samples is elusive and probably of limited interest for geophysical applications. In particular, various choices of p and G_i could be used to match the $\phi \approx 0$ experiments at early times, but the match to all other experiments depends only on q and G_1. Thus, in our interpretation, the grain growth in peridotite in geological settings is controlled by the rate of evolution of the interface between phases, hence by the parameters q and G_1, not by the grain coarsening of the individual phases. Even in the experiments with nominally pure olivine case of Hiraga et al. (2010), the presence of less than 1% of the enstatite minor phase constrained the grain growth by Zener pinning after only a few hours.

4. Simple shear applications with damage and deformation

We examine several sample applications of the full evolution equations with damage, including (a) steady-state simple-shear flow to infer the effective rheology of the continuum under viscometric motion; and (b) evolution of grain-size and interface coarseness in simple shear. Multi-dimensional flows will be examined in later papers (e.g., Bercovici and Ricard, in preparation).

4.1. One-dimensional simple shear and damage: governing equations

For the basic one-dimensional simple-shear model, we assume the medium is contained in a horizontal layer of finite width L in y and infinite and uniform in x. Velocity boundary conditions are applied so that $\mathbf{v} = u(y)\hat{\mathbf{x}}$, which according to (4a) implies that the volume fraction $\phi = \phi_1 = 1 - \phi_2$ is constant; therefore assuming ϕ is initially uniform it must remain uniform.

Given the simple shear assumption, the only component of the strain-rate tensor is $\dot{e} = \frac{1}{2}\frac{\partial u}{\partial y}$, and thus the only component of the stress tensor is the shear stress τ_i given by (4c) or simply

$$\dot{e} = a_i \tau_i^n + \frac{\flat_i}{\mathcal{R}_i^m}\tau_i \tag{13}$$

where $\flat_i = (\lambda_{3-m}/\lambda_3)b_i$. Thus the strain-rate $\dot{e}$ can be treated as the imposed simple-shear that determines both stresses τ_1 and τ_2 in each phase, given mean grain-sizes $\mathcal{R}_i$ and rheological constants a_i and $\flat_i$ in each phase. Assuming that the power-law exponent for each phase is $n = 3$ then (13) is invertible and thus

$$\tau_i(\dot{e}) = E_i - \frac{1}{E_i}\frac{\flat_i}{3a_i\mathcal{R}_i^m} \quad \text{where} \quad E_i = \left(\sqrt{\left(\frac{\flat_i}{3a_i\mathcal{R}_i^m}\right)^3 + \left(\frac{\dot{e}}{2a_i}\right)^2} + \frac{\dot{e}}{2a_i}\right)^{1/3} \tag{14}$$

In this case the deformational work on phase i is simply

$$\Psi_i = 2\dot{e}\tau_i \quad \text{and thus} \quad \overline{\Psi} = \sum_i \phi_i \Psi_i = 2\dot{e}\sum_i \phi_i \tau_i \tag{15}$$

The momentum Eq. (4b) implies that both $\bar{\tau} = \sum_i \phi_i \tau_i$ and $\gamma_1\eta(\phi)/r - \overline{\Pi}$ are uniform in y; these conditions are satisfied assuming τ_i, r, Π_i and thus $\mathcal{R}_i$ (since Π_i includes squeezing from grain-boundary surface tension) are uniform in y, which then implies by (13) that $\dot{e}$ is uniform as well. In this case all quantities are only functions of time t, and the 1-D time dependent relations for interface curvature and grain size, become, following (4d) and (4e),

$$\frac{\mathrm{d}r^q}{\mathrm{d}t} = \eta G_1 - \frac{\mathrm{f}_1 q r^{q+1}}{\gamma_1\eta}\overline{\Psi} \tag{16}$$

$$\frac{\mathrm{d}\mathcal{R}_i^p}{\mathrm{d}t} = G_i\left[1 - \mathrm{h}_i\frac{\mathcal{R}_i^2}{r^2}\right] - \frac{\lambda_3}{\lambda_2}\frac{p\mathcal{R}_i^{p+1}}{3\gamma_i}\frac{\mathrm{f}_G(1-\mathrm{f}_1)\Psi_i}{\left[1 - \mathrm{h}_i\frac{\mathcal{R}_i^2}{r^2}\right]} \tag{17}$$

where f_G is variable as defined in (7). Given the comparison to experiments in Section 3, and all the implicit assumptions therein, we use the Zener pinning factor defined in (8) with $\mathrm{n} = 1$, for which

$$\mathrm{h}_i = c_1(1 - \phi_i) \tag{18}$$

where c_n is also defined in (8) (see also Appendix F.4).

4.1.1. Dimensionless relations

We use classical dimensional analysis (Bridgman, 1922) to scale stress, strain-rate, time and length (for both interface radius of curvature and grain-size) according to

$$\tau_i = \tau_s \tau_i' \tag{19}$$

$$\dot{e} = \bar{a}\tau_s^n \dot{e}' \tag{20}$$

$$t = \frac{1}{\overline{G}}\left(\frac{\bar{\flat}}{\bar{a}\tau_s^{n-1}}\right)^{p/m} t' \tag{21}$$

$$(r, \mathcal{R}) = \left(\frac{\bar{\flat}}{\bar{a}\tau_s^{n-1}}\right)^{1/m}(r', \mathcal{R}') \tag{22}$$

where the stress scale is

$$\tau_s = \left(\frac{3\lambda_2}{\lambda_3}\frac{\overline{G\gamma}}{p\mathrm{f}_G^*(1-\mathrm{f}_1)\bar{a}}\left(\frac{\bar{a}}{\bar{\flat}}\right)^{\frac{p+1}{m}}\right)^{\frac{m}{n(m-p-1)+m+p+1}} \tag{23}$$

and again recall that the average of any quantity Q is $\overline{Q} = \sum_i \phi_i Q_i$.

One can estimate these scales for the Earth's lithosphere by using the material properties for olivine summarized by (Rozel

et al., 2011, Table 1, drawn from various sources referenced therein). At a lower lithospheric temperature of $T = 1000$ K, and for $p = 2$ and $n = m = 3$, we obtain $\tau_s \approx 800$ MPa, and thus the scale for strain-rate is $10^{-14}\,\mathrm{s}^{-1}$, while the length (grain-size) scale is 50 μm, and the time scale is about 130 yrs. Given the sensitivity of kinetic effects on temperature, which thus affect viscosity and grain-growth, the stress and strain-rate scales are likewise variable with temperature; e.g., for a deeper lithospheric temperature of $T = 1200$ K, the stress and strain-rate scale are 140 MPa, and $2 \times 10^{-12}\,\mathrm{s}^{-1}$, respectively, while the length scale becomes 60 μm and the time scale drops to 3 yrs.

Using these scales, we arrive at the dimensionless governing equations, which (after dropping the primes on dimensionless variables) become

$$\dot{e} = \mathfrak{a}_i \tau_i^n + \mathfrak{b}_i \tau_i / \mathcal{R}_i^m \tag{24}$$

$$\frac{\mathrm{d}r^q}{\mathrm{d}t} = \varpi(\mathcal{Q} - r^{q+1}\overline{\Psi}) \tag{25}$$

$$\frac{\mathrm{d}\mathcal{R}_i^p}{\mathrm{d}t} = \mathcal{G}_i\left[1 - \mathfrak{h}_i \frac{\mathcal{R}_i^2}{r^2}\right]\left(1 - \frac{\mathcal{R}_i^{p+1}}{\Upsilon_i\left[1 - \mathfrak{h}_i \frac{\mathcal{R}_i^2}{r^2}\right]^2} \frac{\Psi_i}{\left[1 + \frac{\mathfrak{b}_i}{\mathfrak{a}_i \mathcal{R}_i^m \tau_i^{n-1}}\right]}\right) \tag{26}$$

where $\mathfrak{a}_i = a_i/\bar{a}$, $\mathfrak{b}_i = \flat_i/\bar{\flat}$, $\mathcal{G}_i = G_i/\overline{G}$, $\Upsilon_i = G_i\gamma_i/\overline{G\gamma}$, Ψ_i and $\overline{\Psi}$ are still defined as in (15), and

$$\mathcal{Q} = \frac{\lambda_3}{3\lambda_2} \frac{G_\mathrm{I}\gamma_\mathrm{I}\eta^2}{\overline{G\gamma}} \frac{p\mathfrak{f}_\mathrm{G}^*(1-\mathfrak{f}_\mathrm{I})}{q\mathfrak{f}_\mathrm{I}} \left(\frac{\bar{\flat}}{\bar{a}\tau_s^{n-1}}\right)^{\frac{p-q}{m}} \tag{27}$$

$$\varpi = \frac{3\lambda_2}{\lambda_3} \frac{q\mathfrak{f}_\mathrm{I}}{p\mathfrak{f}_\mathrm{G}^*(1-\mathfrak{f}_\mathrm{I})} \frac{\overline{G\gamma}}{\eta\bar{G}\gamma_\mathrm{I}} \tag{28}$$

Neither the grain-boundary energy γ_i nor the grain-growth coefficient G_i are expected to differ much between phases, and thus $\mathcal{G}_i \approx \Upsilon_i \approx 1$. If the phases do not differ appreciably rheologically either then $\mathfrak{a}_i \approx 1$ and $\mathfrak{b}_i \approx 1$ as well. However, even if the phases had identical mechanical properties, the difference in volume fraction ϕ_i still demands different grain-size solutions from (26).

The parameter $\mathcal{Q}$ represents the rate of interface coarsening relative to grain-growth rate. Since the interface density and curvature is, for example, due to inclusions of one phase separated by the other phase, the interface coarsening rate is associated with the mass transfer between inclusions across an immiscible phase, which is necessarily extremely slow (given that is is diffusion limited) and we assume that at best $\mathcal{Q} < 1$ and more likely $\mathcal{Q} \ll 1$; this is also in agreement with the comparison to experiments in Section 3. Given the lack of direct measurements of G_I (our indirect inference in Section 3 not withstanding), we will explore the effects of varying $\mathcal{Q}$.

4.2. Steady-state simple-shear and an effective shear-localizing rheology

In steady-state the dimensionless governing equations become

$$\dot{e} = \mathfrak{a}_i \tau_i^n + \mathfrak{b}_i \tau_i / \mathcal{R}_i^m \tag{29}$$

$$r^{q+1}\overline{\Psi} - \mathcal{Q} = 0 \tag{30}$$

$$\mathcal{R}_i^{p+1}\Psi_i\left[1 + \frac{\mathfrak{b}_i}{\mathfrak{a}_i \mathcal{R}_i^m \tau_i^{n-1}}\right]^{-1} - \Upsilon_i\left[1 - \mathfrak{h}_i \frac{\mathcal{R}_i^2}{r^2}\right]^2 = 0 \tag{31}$$

Eqs. (29)–(31) are solved for a given range of strain-rates $\dot{e}$ to find τ_i, r and $\mathcal{R}_i$. For all cases, we assume the phases do not differ much in their material properties and thus $\mathfrak{a}_i = \mathfrak{b}_i = \mathcal{G}_i = \Upsilon_i = 1$. The results are displayed as (a) effective constitutive curves for the average stress $\bar{\tau} = \sum_i \phi_i \tau_i$ versus $\dot{e}$, and theoretical deformation maps of interface radius of curvature r versus mean stress $\bar{\tau}$, and mean grain-size $\bar{\mathcal{R}} = \sum_i \phi_i \mathcal{R}_i$ versus $\bar{\tau}$ (Figs. 8 and 9). The stress–strain-rate plots also show the relation for pure dislocation creep $\bar{\tau} = \dot{e}^{1/n}$ (assuming $\mathfrak{a}_i = 1$) for comparison to a medium undergoing no damage and grain-reduction. The deformation maps of $\overline{\mathcal{R}}$ versus $\bar{\tau}$ further display a transition curve between diffusion and dislocation creep wherein $\mathfrak{a}_i \tau_i^n = \mathfrak{b}_i \tau_i / \mathcal{R}_i^m$; this implies a mean transitional grain size (see also (F.34))

$$\mathcal{R}_c = \sum_i \phi_i \left(\frac{\mathfrak{b}_i}{\mathfrak{a}_i \tau_i^{n-1}}\right)^{1/m} \approx \mathrm{fnc}(\bar{\tau}) \tag{32}$$

which we use to delineate diffusion creep ($\overline{\mathcal{R}} < \mathcal{R}_c$) (shaded in the figures) from dislocation creep ($\overline{\mathcal{R}} > \mathcal{R}_c$). However, it should be noted that while this transition is distinct for a single grain, in a medium with a grain-size distribution both diffusion and dislocation mechanisms occur simultaneously.

In general, the effective rheological behavior has very weak (or non-existent) dependence on the grain-growth exponent p. As shown by Rozel et al. (2011), if grain-damage in a single-phase material only occurs by dislocations, as per (7), then the effective rheology remains close to the dislocation creep regime and there is little weakening or grain-size reduction. Moreover, in a two-phase

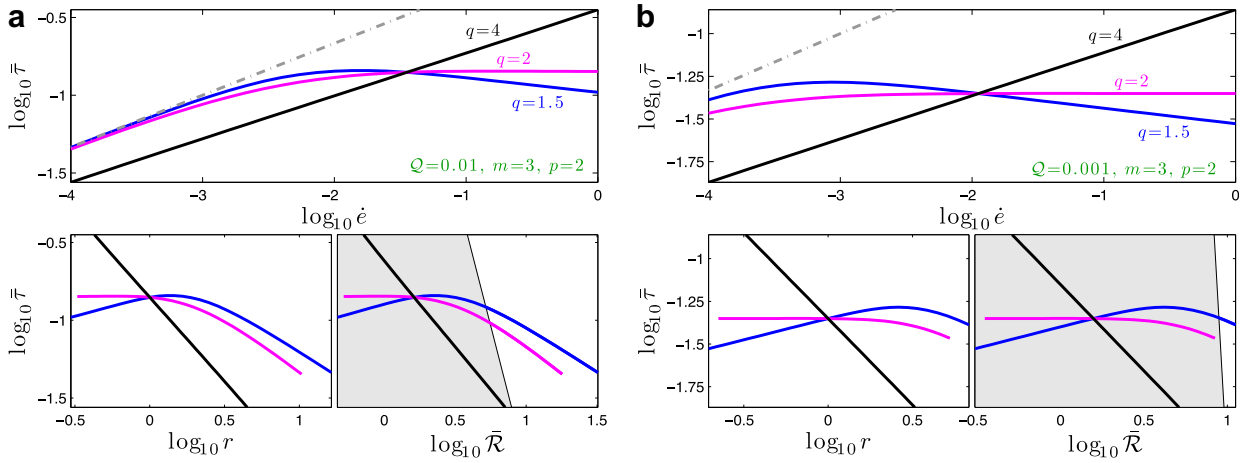

Fig. 8. Dimensionless effective stress–strain-rate constitutive law (top frame) interface coarseness or radius of curvature r (bottom left frame), and mean grainsize $\overline{\mathcal{R}} = \sum_i \phi_i \mathcal{R}_i$ (bottom right frame). The pure dislocation creep constitutive relation $\bar{\tau} = \dot{e}^{1/n}$ is also displayed (dashed-dot curve). Shading in the $\bar{\tau}$ vs $\overline{\mathcal{R}}$ deformation map indicates diffusion creep (gray shading) and dislocation creep (no shading), with the boundary defined by (32), computed with $q = 2$ (using $q = 1.5$ or $q = 4$ has little effect on the boundary); This plot shows the effect of various q for different values of $\mathcal{Q}$ (a and b), and fixed values of m and p, as indicated, and the volume fraction set to $\phi_1 = \phi = 0.4$.

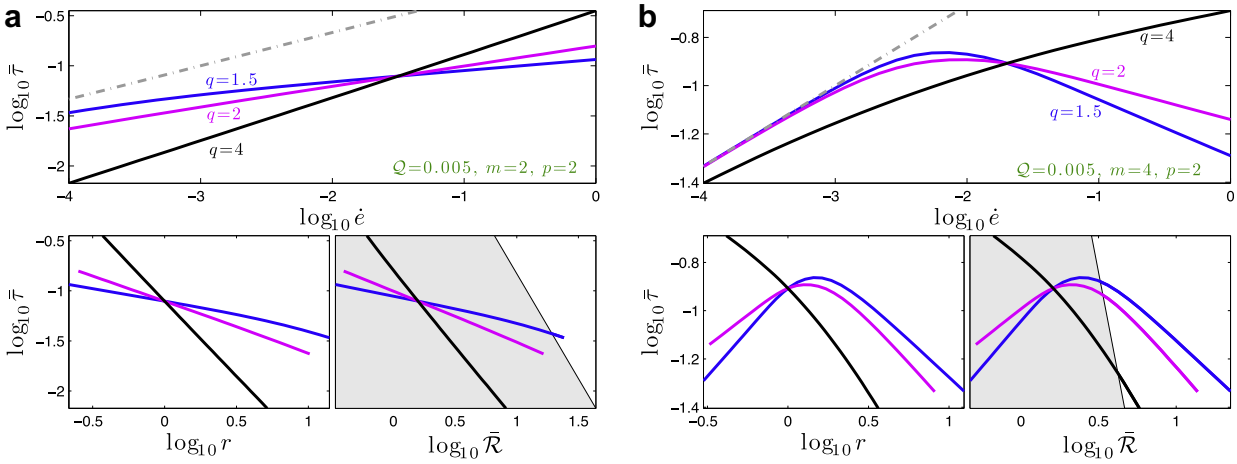

Fig. 9. Same as Fig. 8, except for showing the effect of various q for two values of m (bracketing $m = 3$), given a fixed $\mathcal{Q} \ll 1$, and p as indicated.

medium, grain-growth is largely stalled by pinning (which is exacerbated when interface damage reduces r) and grain-size eventually tracks the evolution of the interface coarseness r (e.g., see Section 3). Thus, in total, the influence of the grain evolution equation and in particular of p is weak.

However, the effective rheology displays a variety of behaviors, depending strongly on the size of the interface coarsening exponent q and relative coarsening rate $\mathcal{Q}$. For small q (e.g., $q \leqslant 2$ for the cases shown in Fig. 8) at small strain-rates, the medium is highly viscous and in the dislocation creep regime. For these same q and large strain-rates the medium is driven well into the diffusion creep regime and can either display plastic yielding for "intermediate" q (i.e., $q = 2$ for the cases shown) or velocity weakening at "smaller" q (i.e., $q < 2$). The transition from viscous to either plastic or velocity-weakening clearly occurs at the transition from dislocation to diffusion creep given by $\mathcal{R}_c(\bar{\tau})$. For "larger" q (e.g., $q = 4$ in the cases shown) the medium displays a monotonic power-law behavior without plasticity or velocity-weakening; however, the material is in the diffusion creep regime with small grains even at low strain-rates and is thus always considerably weaker than if it were in pure dislocation creep. Thus even with "large" q, a shear zone experiencing grain-reduction via interface damage and pinning will be weaker and/or more highly deformed than a neighboring zone with large grains in dislocation creep.

The parameter $\mathcal{Q}$ primarily affects where in deformation space the transition from viscous to plastic or velocity-weakening behavior occurs for "small" q, and the strength of the material relative to that in dislocation creep for "larger" q (Fig. 8). Decreasing $\mathcal{Q}$ causes the transition to weakening behavior to occur at smaller strain-rate $\dot{e}$, which is to be expected since a lower strain-rate or stress is sufficient to drive damage and softening behavior when interface coarsening or "healing" is slow. Likewise the strength of the material at larger q is reduced for smaller $\mathcal{Q}$ because r (and thus $\mathcal{R}_i$) must be reduced much more before healing can balance damage.

The effect of varying both q and the grain-size sensitivity on rheology, represented by the exponent m, indicates that the difference between q and m determines whether plastic or velocity-weakening behavior occurs (Fig. 9). For grain-volume (Nabarro-Herring) diffusion creep with $m = 2$, the medium tends toward power-law viscous behavior without plasticity or velocity weakening, although the medium is still driven into diffusion creep and is weaker than if it were in dislocation creep. For more strongly grain-size sensitive creep (such as grain-boundary diffusion or Coble creep with $m = 3$), the medium can more readily experience plasticity or velocity weakening.

As shown in the scaling analysis in the Appendices (Appendix H.1) the sign of the slope of the high-strain rate branch depends simply on the sign of $q - m + 1$. Thus low q and/or high m promotes plasticity or velocity-weakening at high strain-rates. While large $q > m - 1$ leads to power-law type behavior, it also promotes a weak diffusion creep rheology at all strain-rates.

In summary, what dominates the deformation behavior is interface damage and the subsequent influence of interface curvature on grain evolution by Zener pinning, and thence the effect of grain-size on rheology. In particular, interface damage and the increase in interfacial curvature drives the grain-size down by pinning, until the rheology is dominated by self-softening grain-size-dependent diffusion creep. Thus the increase in interface curvature through damage combined with Zener pinning allows damage and grain-size-dependent deformation to co-exist, unlike the traditional dynamic recrystallization mechanisms in a single phase.

4.3. Evolution of grains and interface with damage in simple shear

The steady-state solutions and effective rheology determined by our model predict the existence of localized mylonitic-type (small grain-size) weak zones, given the feedback between grain-size and interface dynamics. However, two key questions remain with regard to the evolution of weak zones. First, how much time is needed to reach a steady state weak zone from pristine conditions? Second, how long will a damaged shear zone persist after deformation ceases? If the shear zone develops in a time much longer than the maximum age of a tectonic plate (O(100) Myrs), then the weakening mechanism is not particularly relevant. Likewise if an inactive shear-zone vanishes in a time much shorter than the age of a plate then the mechanism is also not geologically pertinent (i.e., for predicting the existence of long-lived dormant weak zones or plate boundaries).

We can address the above questions by numerically integrating (with standard adaptive Runge-Kutta ordinary-differential equation solvers) (25) and (26) given an imposed strain-rate – and stress and deformational work derived from (24) – until the steady-state is reached. After steady state is reached the strain-rate is set to zero and the system is allowed to evolve back to its original conditions (Fig. 10)

Numerical solutions show that grains initially grow while the interface coarseness or radius of curvature r shrinks, until the Zener pinning effect becomes significant and starts to drive grain reduction also; eventually the low-stress steady state is reached wherein healing balances damage. For example, in the case for

$q = 2$ and nondimensional strain-rate $\dot{e} = 10^{-2}$, steady-state is reached within a dimensionless time of about 10^4 (Fig. 10a). After a steady state is reached and the driving strain-rate removed, the original conditions are recovered within a dimensionless time of 10^6. Thus, for this case, shear-zone development is roughly 100 times faster than shear-zone erasure. For $q = 4$ the shear-zone is developed in the same amount of time, but erasure takes roughly four orders of magnitude longer (Fig. 10c). Although not shown, cases with $q = 1.5$ differ little from the case with $q = 2$, with the erasure time being somewhat faster. Thus, for example, with a lower lithosphere at about 1000 K temperature, the time scale is approximately 100 yrs (see Section 4.1.1), and thus it takes about 1 Myrs for a shear-zone to develop, and after deformation ceases about 100 Myrs for the shear-zone to vanish for $q = 2$, and 1 Tyrs for $q = 4$.

For a larger more tectonically active strain rate $\dot{e} = 10$, the localization time (time to reach steady state) is much shorter (by about two orders or magnitude) for both $q = 2$ and 4; however, the healing time remains unchanged (Fig. 10b and d). Although not shown, cases with smaller $\mathcal{Q}$ (i.e., $\mathcal{Q} = 10^{-3}$ as opposed to those shown with $\mathcal{Q} = 10^{-2}$), the weakening is more dramatic (i.e., the stress drop is deeper) and the time for the weak zone to vanish is proportionally longer.

For the cases shown with $\mathcal{Q} = 10^{-2}$, the low strain-rate systems involve a stress drop during shear-zone formation of less than an order of magnitude, but by about an order of magnitude for the high strain-rate cases. The stress drop is slightly stronger for the secondary phase than the primary one because pinning tends to be more effective on the secondary phase. Moreover, the stress drop is slightly larger for $q = 4$ than for $q = 2$ at low strain rates, and vice-versa at large strain rates. For smaller $\mathcal{Q} = 10^{-3}$, the stress drops roughly 2 orders of magnitude at high strain-rate. Again, for a 1000 K lower lithosphere, the stress scale is about 800 MPa (see Section 4.1.1) and so stress drops by two orders of magnitude will reach tectonic stresses. For all cases the grain-sizes and interface courseness drop by 2-3 orders of magnitude during shear-zone development, and with a grain scale of about 50 μm, the grain-size will drop to a several tenths of a μm.

Approximate analytic solutions are derived in Appendix H.2 and verified by comparison to the numerical results (see Fig. H.2), which allows us to explore the dependence of damage and localization time as well as healing and recovery time on both strain-rate $\dot{e}$ and interface coarsening rate $\mathcal{Q}$; in using the analytic solutions we fix the parameters $m = n = 3$ and $q = 2$ (since the recovery time for $q = 4$ is astronomically long). A useful quantity

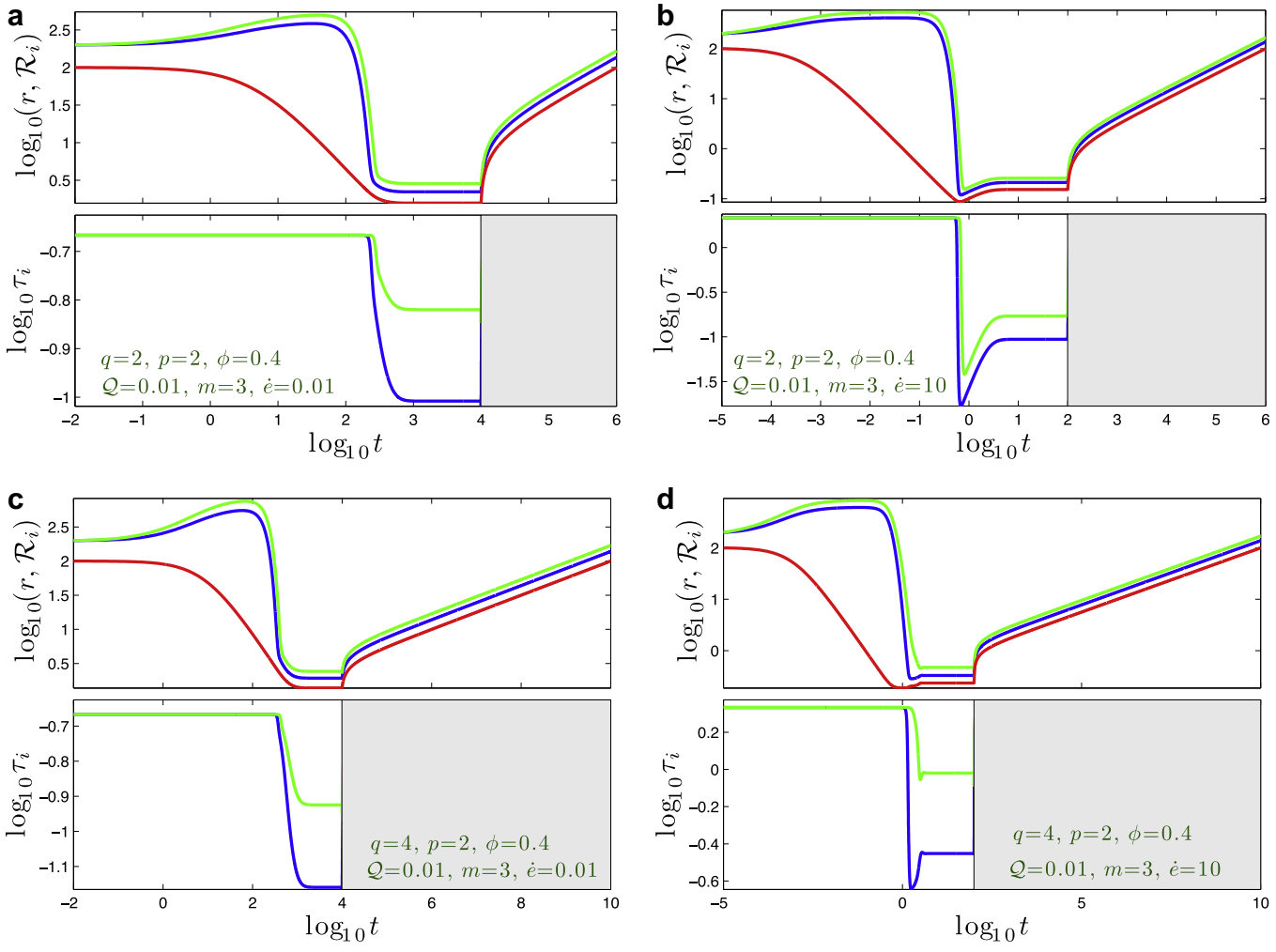

Fig. 10. Dimensionless grainsizes $\mathcal{R}_i$, interface radius of curvature r and stresses in each phase τ_i versus time (for parameters indicated). The four frames a–d are for two different q each for two different strain-rates $\dot{e}$ as indicated; other parameters such as $\mathcal{Q}, p, m$, and ϕ are also indicated (the parameter $\varpi = 1$ in all cases). Blue [dark grey] curves are for the minor phase $i = 1$ (i.e., with $\phi_1 = \phi = 0.4$) and the green [light grey] curves are for major phase $i = 2(\phi_2 = 1 - \phi = 0.6)$; red [medium grey] curves are for r. In these calculations, strain-rate $\dot{e}$ is imposed until steady-state is reached in order to gauge the time needed to reach a shear-localized low-stress state. Once steady-state is reached $\dot{e}$ is set to zero (hence stress is zero, indicated by grey region) and the system is allowed to evolve back to its initial state in r, which measures the healing time or longevity of the weak zone. (For interpretation of the references to colour in this figure legend, the reader is referred to the web version of this article.)

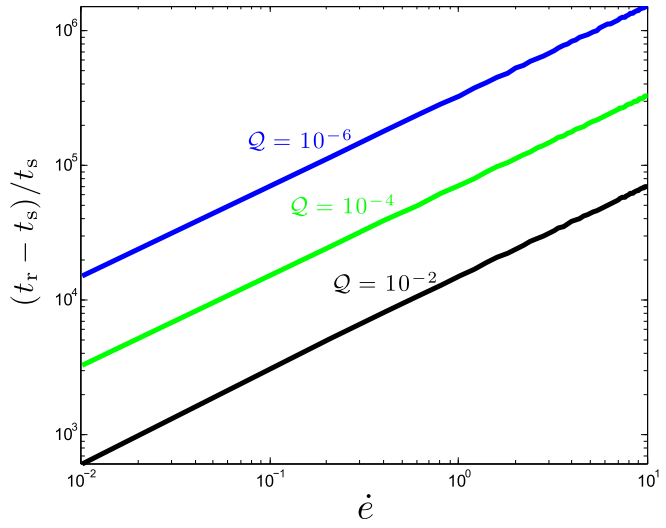

Fig. 11. Ratio of healing and recovery time (from a localized damage state back to the initial state, from (H.10)) to the localization and damage time (from the initial state to the steady damaged state, i.e., t_s which arises from the sum of (H.7) and (H.8)) versus dimensionless strain-rate $\dot{e}$ for several values of the interface coarsening rate $\mathcal{Q}$. Recovery and localization times are based on the approximate analytic solutions from Appendix H.2. Solutions are for $q = 2, m = n = 3$, and are largely insensitive to the parameter ϖ and initial interface radius of curvature r_o.

to consider is the ratio of healing and recovery time to damage and localization time, i.e., $(t_r - t_s)/t_s$ (where t_s is the time for the shear zone to develop and reach steady state, and t_r is the total final time after the strain-rate has been turned off for $t > t_s$ and for r to return to its original state); this ratio indicates the longevity of a weak zone after formation relative to its actual formation time (Fig. 11). The ratio is always several powers of 10, and increases with increasing strain-rate significantly; for the chosen q, m and n, the ratio increases with $\dot{e}$ to the power 2/3 (see Appendix H.2). In the end, model solutions demonstrate that the formation time for weak zones or plate boundaries is typically much much shorter than their recovery and erasure, or healing time. In total, this mechanism readily explains both rapid formation and extended longevity of plate boundaries.

5. Discussion

One of the key aspects of our two-phase model of grain-damage is that damage is mostly imposed on the interface between phases, while direct damage to grains is greatly reduced when they are small and in the diffusion creep regime. However, damage increases interface density and curvature, which in turn drives down mean grain-size by Zener pinning (see Section 2.4) into the "permanent" diffusion creep state. In this way, damage co-exists with grain-size induced weakening, thereby allowing the requisite feedback for shear-localization. Moreover, if deformation ceases and the localized zone becomes dormant, Zener pinning blocks healing and grain growth, forcing it to follow coarsening of the interface which is implicitly much slower.

Recent studies by Warren and Hirth (2006) and Skemer et al. (2009) on deformation in natural peridotites are relevant to the predictions of our model, and analyses of lower crustal materials display similar behavior (Mehl and Hirth, 2008). (It should also be noted that aside from grain-size feedbacks, self-softening can also occur due to shearing and interconnection of very soft secondary phases e.g., see Holyoke et al. (2006) for analysis of crustal rocks.) Both peridotite studies observe continuous deformation and breakdown of pyroxene inclusions and suggest a strong controlling effect of the secondary phase. Indeed, Warren and Hirth (2006) note that fine-grained olivine shear zones in mylonites are consistently correlated with populations of small pyroxene and spinel inclusions, and attribute this to pinning (see also Mehl and Hirth, 2008); they also infer that pinning forces olivine grains into a "permanent" diffusion creep regime as found by our theoretical analysis. Experimental deformation maps, however, still tend to be presented in terms of stress and the grain-size for the major phase (olivine), and the influence of interface density is only indirectly evident in the grain-size data by qualitative distortion of regime boundaries. Direct data on the size distribution of interface coarseness and its evolution are lacking, and this is the information perhaps most essential for testing the theory presented here. However, our theory at least provides some guiding hypothesis for future experiments. For example, one of the more speculative aspects of the current theory regards the phenomenological laws for the evolution of interface density (comparison to grain-growth experiments in Section 3 not withstanding), which we demonstrate is a key component of the theory; it is thus very important to understand at a micro-physical scale what controls both processes of interface coarsening and damage.

Coarsening of the interface likely occurs both by grain-growth in each phase (and therefore is limited by the slowest grain-growth rate of the two phases), and by smoothing of interface distortions, a process which is necessarily slow as it implies diffusion along a contorted interface path or across another phase (see Solomatov et al., 2002, and references therein). Thus interface coarsening is certain to be much slower than that for grains of like composition that are in contact with each other (which is also implied by the comparison to grain-growth experiments in Section 3).

Since interface coarsening involves diffusive mass flux of the secondary phase along the interface itself or across the primary phase, then its rate is thermally controlled by standard diffusion kinetics (e.g., Herwegh et al., 2005). The diffusive mobility of the secondary phase might also be facilitated by its solubility in the primary phase, as with Ostwald ripening (see Voorhees, 1992; Solomatov et al., 2002), which also increases with increased temperature. Thus the enhanced lithospheric healing (relative to damage) on hotter planets like Venus would still hold, consistent with the climatic explanation for why Earth has plate tectonics and Venus does not (Lenardic et al., 2008; Landuyt and Bercovici, 2009b), and how surface temperature influences the likelihood of plate tectonics occurring on super-Earths (Foley et al., 2012). In particular, an increase in the interface coarsening coefficient G_I, or its dimensionless version $\mathcal{Q}$, with higher temperature suppresses localization and weakening (Fig. 8) and greatly reduces the healing recovery time (Fig. 11). In the end, the coarsening coefficient G_I likely depends on various properties, including composition and temperature, and needs to be further examined experimentally or possibly by molecular dynamics models.

Damage to the interface at a microscopic scale is likely to be a complex process relying on several possible mechanisms. Warren and Hirth (2006) suggest that secondary phase inclusions break down by translation of grains via grain-boundary sliding, which implies basic disaggregation of inclusions into their component grains. Disaggregation and mixing of grains does not necessarily require propagation of dislocations and recrystallization of new grains, and thus could proceed regardless of rheological mechanisms (as is assumed in the theory here). If inclusions exist as or are reduced to single grains, it is possible they could only be broken down further by dislocations and recrystallization (Skemer et al., 2009), which would cease once they left the dislocation creep regime. However, even if single-grain inclusions deform by diffusion creep, they and the interface around them will still deform and be stretched into shapes with greater surface area and mean curvature, without changing volume or mean size; e.g., a spherical inclusion stretched into a needle shape is likely to cause more

Zener pinning on grains around it. Further experiments clearly need to be carried out to track the evolution of both grain-size and interface morphology, although the data may exist already from past experiments.

Regardless of experimental studies, field measurements might provide a test for the shear-localizing mechanism proposed here, or in general any grain-size related localizing mechanism. In particular, taken at face value, our model predicts that ultra-low-strain-rate diffuse plate boundaries (e.g., Gordon, 2000) would occur on the non-localizing branch of the constitutive curves (see Figs. 8 and 9), while sharper shear zones would be associated with the high-strain-rate localizing or weakening branch of the the same curves. The low strain-rate curves generally correlate with dislocation creep (with some exceptions) while the high-strain rate curves correlate with grain-size sensitive diffusion creep with grain-reduction. Since lattice-preferred orientation in olivine occurs in the dislocation creep regime, the dominant rheology should be reflected in shear-wave splitting measurements. Grain damage theory would thus predict that diffuse plate boundaries would involve more seismic anisotropic fabric in the deep lithosphere than sharper shear boundaries, although a comparison of such boundaries would ideally be for similar stress environments, such as within the same plate, and assuming that other effects, such as shape-preferred orientation in a sharp shear zone, can be separated out.

6. Conclusion

Shear localization and weakening through grain-size reduction has been considered one of the key mechanisms for plate generation because it can exist in the deep lithosphere, involves material damage that permits dormant weak zones, and has observational support in mylonitic mantle rocks. However, theories of grain-size reduction have been problematic because of the exclusive rheological domains that preclude the co-existence of grain reduction by damage and weakening by grain-size-dependent diffusion creep; without coupling of both mechanisms it is difficult to sustain a positive shear-localizing feedback. Moreover, grain growth in single-phase (mono-minerallic) materials is rapid and would, by itself, not be able to sustain a dormant weak zone.

However, actual lithospheric materials are at least two-phase (polyminerallic), such as peridotites with olivine (as the major phase) and pyroxenes (as the secondary phase). In these materials, grain growth in both phases is retarded because of effects like Zener pinning; in particular, the interface between the phases acts like an obstacle to grain growth. This interface itself evolves because of deformation and coarsening and is thus likely to have a dynamic influence on grain evolution. We have therefore developed from classical first principles a continuum theory of two-phase grain-damage allowing for the interaction between grains and interface through Zener pinning.

We find that, depending on its density or curvature, the interface between phases does indeed retard grain-growth and even tends to make grains more susceptible to damage (see Sections 2.2.2 and 2.4) although direct damage to grains is self-limited when the grains enter the diffusion creep regime. However, the most profound effect is that damage causes an increase in interface area density and curvature (e.g., size reduction or stretching of pinning inclusions), which, through Zener pinning, drives down the size of grains into the diffusion creep regime. This mechanism therefore allows grain-size reduction via damage (albeit indirectly) to coexist with grain-size–dependent softening, thus leading to the weakening or shear-localizing feedback needed to generate plate boundaries.

Equally profound is that grain growth is dictated by coarsening of the interface, which is extremely slow, and orders of magnitude slower than the formation time for weak zones. Indeed analysis of our model shows that while weak zones are likely to develop to a steady state in 1 Myrs or less, dormant zones will take several 100 Myrs or more to vanish. This effect thus permits long-lived weak zones along dormant plate boundaries to exist at least as long as a typical plate age.

The theory presented herein is a culmination of two-phase damage theories and grain-damage models that capture the essential physics of plate generation. With further testing and refinement, this framework will (we hope) provide understanding for the origin of plate tectonics on Earth, as well as predictions for the conditions for plate tectonics and all its attendant phenomena on terrestrial planets in other solar systems.

Acknowledgments

The authors thank Mark Jellinek, John Hernlund and two anonymous referees for extremely helpful comments and reviews. Support was provided by the National Science Foundation (NSF, Grant EAR-1015229), the Agence Nationale de la Recherche (Labex LIO), the Yale Amity Geophysical Annex (YAGA) and Le Garon Foundation for Supine Geophysics (GFSG).

Appendix A. Phases, interfaces and mass conservation

The model continuum is a mixture of two immiscible components, or phases, each of which has, at a point in space, a unique grain-size distribution. In treating the separate phases (irrespective of grains), we identify them by a phase distribution function φ_i, which is 1 where phase i exists and 0 where it does not (see Bercovici et al., 2001a). The volume of phase i within the control volume δV is

$$\delta V_i = \int_{\delta V} \varphi_i dV = \phi_i \delta V \tag{A.1}$$

where ϕ_i is the volume fraction of phase i in the control volume δV, and $\sum_{i=1}^{2} \phi_i = 1$. Moreover, if we have any quantity or property at a point in space within phase i called $\tilde{q}_i$, then its volume average q_i over the phase is defined such that

$$\int_{\delta V} \tilde{q}_i \varphi_i dV = q_i \phi_i \delta V \tag{A.2}$$

It is often convenient to refer to one of the volume fractions simply as ϕ, and we choose (arbitrarily) $\phi_1 = \phi$, in which case $\phi_2 = 1 - \phi$.

We can also use the function φ_i to define the interfacial area between phases

$$\delta A_{\mathrm{I}} = \int_{\delta V} \|\nabla \varphi_i\| dV = \alpha \delta V \tag{A.3}$$

where α is the interfacial area density (interfacial area per unit volume of the mixture) which is independent of phase index i since $\nabla \varphi_1 = -\nabla \varphi_2$ (see Bercovici et al., 2001a).

The interface density α is an important property of this model because it governs the density of surfaces that block grain-growth by Zener pinning, as discussed in Section 2.2. The interface density has been prescribed previously (Ganesan and Poirier, 1990; Bercovici et al., 2001a; Bercovici and Ricard, 2005) to be an isotropic function of volume fraction $\phi = \phi_1$ and interface fineness $\mathcal{F}$, which is the inverse of coarseness represented by the interface mean radius of curvature r (Bercovici and Ricard, 2005; Landuyt and Bercovici, 2009a). Clearly for a given interface radius of curvature, the interface density must vanish as $\phi \to 0$ or 1. But, also, for a given ϕ the interface density can vary depending on homogeneity of the mixture, e.g., on the size of inclusions of one phase inside the other (each inclusion itself being composed of an ensemble of

grains of like phase). For example, in a dilute mixture of spheres of phase 1 each of radius r and surrounded by phase 2, we readily find $\alpha = 3\phi/r$; however, we generalize this to non-dilute systems by assuming

$$\alpha = \mathcal{F}\eta(\phi) = \frac{\eta(\phi)}{r} \tag{A.4}$$

such that η vanishes at $\phi = 0$ and *1* and r is now a mean radius. Thus, for a given a mixture of spherical inclusions of mean radius r of both phases, η can be assumed to take the symmetric form $\eta = 3\phi_1\phi_2 = 3\phi(1-\phi)$, which captures both dilute limits $\phi \to 0$ or 1.

When we consider the two-phase medium to be a simple mixture of grains of two components, then the interface radius of curvature r can be partially characterized by grain-sizes in some statistical mixture (see Appendix G). However, r is also governed by grain clumping, stretching, flattening, and/or squeezing of grains in between other grains (see Appendix C.3 as well as Fig. 2); thus in any interface treatment of a two-phased grained medium, r is independent of (or not uniquely dependent on) each phase's grain-size.

A.1. Mass conservation

Even though the two rock phases in the continuum are grained, the grains are assumed to be in complete contact, i.e., there are no gaps, voids or fluids on the grain boundaries, and thus the grains fill all space. The effect of damage on void generation and the presence of fluids has been covered elsewhere; this form of damage has been shown to be a poor candidate for shear-localization across most of the lithosphere (Bercovici and Ricard, 2005; Landuyt and Bercovici, 2009a), although it is in good agreement with failure envelopes for porous rocks (Ricard and Bercovici, 2003). The phases are also assumed to be incompressible such that the density of phase i (where $i = 1,2$) ρ_i is a constant; moreover, there is no exchange between phases. These assumptions lead to the classical mass conservation equation for two-phase continua:

$$\frac{\partial \phi_i}{\partial t} + \nabla\cdot(\phi_i \mathbf{v}_i) = 0 \tag{A.5}$$

where the velocities of each phase $\mathbf{v}_i$ are potentially different.

However, since the two phases in our typical applications to mantle dynamics are both solid-state minerals, phase separation is likely negligible, which argues for assuming that the phase velocities are the same, i.e., $\mathbf{v}_1 = \mathbf{v}_2$. If $\mathbf{v}_1 = \mathbf{v}_2 = \mathbf{v}$ then the volume averaged velocity is also $\bar{\mathbf{v}} = \sum_i \phi_i \mathbf{v}_i = \mathbf{v}$, and thus the sum of (A.5) over i shows that $\mathbf{v}$ is solenoidal. Therefore the mass conservation relation (A.5) can be recast as

$$\frac{\partial \phi}{\partial t} + \mathbf{v}\cdot\nabla\phi = 0 \quad \text{and} \quad \nabla\cdot\mathbf{v} = 0 \tag{A.6}$$

which is also reproduced as (4a) in Section 2.3.

However, for much of the following development we employ independent phase velocities for the sake of generality, but remark as needed on the effect of assuming $\mathbf{v}_i = \mathbf{v}$.

Appendix B. Grain distributions and evolution

B.1. Grain distributions and average properties

The exact number of grains per unit volume between the sizes of R and R + dR in phase i at a point in space at position $\mathbf{x}$ is $\breve{\nu}_i(\mathrm{R},\mathbf{x},t)d\mathrm{R}$. The total number of grains in phase i within the control volume δV is thus

$$\delta N_i = \int_{\delta V} \varphi_i \left(\int_0^\infty \breve{\nu}_i d\mathrm{R}\right) dV = \int_0^\infty \left(\int_{\delta V} \varphi_i \breve{\nu}_i dV\right) d\mathrm{R}$$
$$= \delta V \phi_i \int_0^\infty \nu_i d\mathrm{R} \tag{B.1}$$

where $\nu_i d\mathrm{R}$ is the average number of grains between R and R + dR over the volume of phase i within the control volume δV, and φ_i and ϕ_i are defined above in Appendix A. The total number of grains in phase i within a macroscopic volume V is

$$N_i = \int_V \int_0^\infty \nu_i d\mathrm{R}\phi_i dV \tag{B.2}$$

The volume of the phase i can be determined either by integrating over the distribution function φ_i as in (A.1), or equivalently by adding up the volumes of all the grains in the phase. The volume of a single grain of size R is $\breve{\mathrm{V}} = \frac{4}{3}\pi\mathrm{R}^3$ where in fact π can represent either the classical value of 3.14159... or a geometric factor for a regular polyhedral shape (Ricard and Bercovici, 2009). The volume of phase i in the control volume δV is thus

$$\delta V_i = \int_{\delta V} \varphi_i \int_0^\infty \breve{\mathrm{V}}\breve{\nu}_i d\mathrm{R}dV = \left(\int_0^\infty \breve{\mathrm{V}}\nu_i d\mathrm{R}\right)\phi_i \delta V \tag{B.3}$$

and hence by equivalence to (A.1) we obtain

$$\int_0^\infty \breve{\mathrm{V}}\nu_i d\mathrm{R} = 1 \tag{B.4}$$

as inferred by Ricard and Bercovici (2009) for a single-phase medium.

Having introduced $\breve{\mathrm{V}}$, we also note that any variable $\breve{Q}$ similarly accented defines a quantity or property specific to a grain of size R.

The density of phase i is ρ_i, which is assumed a constant (i.e., the phases are incompressible). The mass of a grain of size R in phase i is thus $\breve{\mathrm{m}}_i = \rho_i \breve{\mathrm{V}}$. The total mass of phase i in the control volume δV is

$$\delta M_i = \int_{\delta V} \rho_i \varphi_i dV = \rho_i \phi_i \delta V \tag{B.5}$$

but also

$$\delta M_i = \int_{\delta V} \int_0^\infty \breve{\mathrm{m}}_i \breve{\nu}_i d\mathrm{R}\varphi_i dV = \left(\int_0^\infty \breve{\mathrm{m}}_i \nu_i d\mathrm{R}\right)\phi_i \delta V \tag{B.6}$$

and hence

$$\int_0^\infty \breve{\mathrm{m}}_i \nu_i d\mathrm{R} = \rho_i \tag{B.7}$$

which is a useful relation, although in fact is really just equivalent to (B.4).

B.2. Grain-size and grain quantity evolution

The number of grains of phase i within a portion of distribution space from R_1 to R_2 and over a finite control volume ΔV is

$$n_i = \int_{\Delta V} \int_{\mathrm{R}_1}^{\mathrm{R}_2} \nu_i d\mathrm{R}\phi_i dV \tag{B.8}$$

The control volume ΔV is assumed fixed and open, and likewise the portion of grain-size space between R_1 and R_2 is fixed and open to transfer of mass from other populations from the surrounding distribution. In this case, the rate of change of grain numbers is

$$\frac{\partial n_i}{\partial t} = \int_{\Delta V}\int_{\mathrm{R}_1}^{\mathrm{R}_2} \frac{\partial \nu_i \phi_i}{\partial t} d\mathrm{R}dV$$
$$= -\int_{\Delta A}\int_{\mathrm{R}_1}^{\mathrm{R}_2} \nu_i d\mathrm{R}\phi_i \mathbf{v}_i\cdot\hat{\mathbf{n}}dA - \int_{\Delta V}[\nu_i \dot{\mathrm{R}}_i]_{\mathrm{R}_1}^{\mathrm{R}_2}\phi_i dV$$
$$+ \int_{\Delta V}\int_{\mathrm{R}_1}^{\mathrm{R}_2} \Gamma_i d\mathrm{R}\phi_i dV \tag{B.9}$$

where ΔA is the surface area of the control volume, $\hat{\mathbf{n}}$ is the unit normal to a surface area element dA, $\dot{\mathrm{R}}_i$ is the growth rate of a grain of size R in phase i, Γ_i accounts for discontinuous or distal transfer

of grain numbers from non-neighboring populations within the grain-size distribution (i.e., from breaking or fusing of grains), and we have used the fact that $\mathbf{v}_i$ and ϕ_i are independent of grain-size. Allowing the volume ΔV to be arbitrary, taking the limit that $\mathsf{R}_2 - \mathsf{R}_1 = d\mathsf{R} \to 0$ and using Stokes theorem, we arrive at

$$\frac{\partial \phi_i v_i}{\partial t} + \boldsymbol{\nabla}\cdot(\mathbf{v}_i \phi_i v_i) + \phi_i \frac{\partial}{\partial \mathsf{R}}(\dot{\mathsf{R}}_i v_i) = \Gamma_i \phi_i \tag{B.10}$$

Using (A.5), the above Eq. (B.10) becomes

$$\frac{\partial v_i}{\partial t} + \mathbf{v}_i \cdot \boldsymbol{\nabla} v_i + \frac{\partial}{\partial \mathsf{R}}(\dot{\mathsf{R}}_i v_i) = \Gamma_i \tag{B.11}$$

which is the same as for a single phase material as shown by Ricard and Bercovici (2009).

Let us now consider the rate of change of a quantity Θ_i in phase i within a closed and deformable volume ΔV; Θ_i could represent the mass or internal energy of phase i. Likewise this quantity exists per grain as $\breve{\theta}_i$, which, for example, could be the mass or internal energy of a single grain of size R in phase i. The macroscopic and grain-scale quantities are related according to

$$\Theta_i = \int_{\Delta V}\int_0^\infty \breve{\theta}_i(\mathsf{R}) v_i d\mathsf{R}\phi_i dV \tag{B.12}$$

The rate of change of Θ_i moving with phase i in this closed deforming control volume is

$$\frac{D_i\Theta_i}{Dt} = \int_{\Delta V}\int_0^\infty \left(\frac{D_i\breve{\theta}_i v_i \phi_i}{Dt} + \breve{\theta}_i v_i \phi_i \boldsymbol{\nabla}\cdot\mathbf{v}_i\right) d\mathsf{R}dV \tag{B.13}$$

where the $\boldsymbol{\nabla}\cdot\mathbf{v}_i$ term represents the rate that the volume of phase i in ΔV expands. The above equation can be recast – using (A.5) and (B.11) – as

$$\begin{aligned}\frac{D_i\Theta_i}{Dt} &= \int_{\Delta V}\int_0^\infty \left(v_i\frac{D_i\breve{\theta}_i}{Dt} + \breve{\theta}_i\frac{D_i v_i}{Dt}\right) d\mathsf{R}\phi_i dV \\ &= \int_{\Delta V}\int_0^\infty \left(v_i\frac{D_i\breve{\theta}_i}{Dt} + \breve{\theta}_i(\Gamma_i - \frac{\partial \dot{\mathsf{R}}_i v_i}{\partial \mathsf{R}})\right) d\mathsf{R}\phi_i dV \\ &= \int_{\Delta V}\int_0^\infty \left(v_i\left[\frac{D_i\breve{\theta}_i}{Dt} + \dot{\mathsf{R}}_i\frac{\partial\breve{\theta}_i}{\partial\mathsf{R}}\right] - \frac{\partial}{\partial\mathsf{R}}\left(\dot{\mathsf{R}}_i\breve{\theta}_i v_i\right) + \breve{\theta}_i\Gamma_i\right) d\mathsf{R}\phi_i dV\end{aligned} \tag{B.14}$$

Defining the full derivative in grain space as

$$\frac{\mathrm{d}_i}{\mathrm{d}t} = \frac{D_i}{Dt} + \dot{\mathsf{R}}_i\frac{\partial}{\partial\mathsf{R}} \tag{B.15}$$

and assuming that $\dot{\mathsf{R}}_i\breve{\theta}_i v_i \to 0$ as $\mathsf{R}\to 0$ or ∞ (i.e., the distribution vanishes above a maximum grain-size, and since $\breve{\theta}_i$ is an extensive grain property, e.g., grain mass, energy, etc., it also vanishes at zero grain-size), then (B.14) becomes

$$\frac{D_i\Theta_i}{Dt} = \int_{\Delta V}\int_0^\infty \left(v_i\frac{\mathrm{d}_i\breve{\theta}_i}{\mathrm{d}t} + \Gamma_i\breve{\theta}_i\right) d\mathsf{R}\phi_i dV \tag{B.16}$$

Thus for example, if $\Theta_i = M_i$, the mass of phase i, then,

$$\frac{D_i M_i}{Dt} = \int_{\Delta V}\int_0^\infty \left(v_i\frac{\mathrm{d}_i\breve{m}_i}{\mathrm{d}t} + \Gamma_i\breve{m}_i\right) d\mathsf{R}\phi_i dV \tag{B.17}$$

Since the volume is closed, $\frac{D_iM_i}{Dt} = 0$, and since the volume is arbitrary, then we require

$$\int_0^\infty \left(v_i\frac{\mathrm{d}_i\breve{m}_i}{\mathrm{d}t} + \Gamma_i\breve{m}_i\right) d\mathsf{R} = 0 \tag{B.18}$$

However, we assume that the processes of mass transport by continuous transfer between neighboring grain populations (e.g., due to diffusion of mass between grains and continuous coarsening) and that due to discontinuous transfer between non-neighboring populations (breaking or fusion of grains) are decoupled, in which case we specify that

$$\int_0^\infty \frac{\mathrm{d}_i\breve{m}_i}{\mathrm{d}t} v_i d\mathsf{R} = 0 \quad \text{and} \quad \int_0^\infty \breve{m}_i\Gamma_i d\mathsf{R} = 0 \tag{B.19}$$

which is similar to the case for a single phase as specified in Ricard and Bercovici (2009).

In some instances it is convenient to define the linear differential operator

$$\frac{\mathfrak{D}_i}{\mathfrak{D}t} = \frac{\mathrm{d}_i}{\mathrm{d}t} + \frac{\Gamma_i}{v_i} \equiv \frac{D_i}{Dt} + \dot{\mathsf{R}}_i\frac{\partial}{\partial\mathsf{R}} + \frac{\Gamma_i}{v_i} \tag{B.20}$$

in which case we can rewrite (B.16) and (B.17) as

$$\frac{D_i\Theta_i}{Dt} = \int_{\Delta V}\int_0^\infty \frac{\mathfrak{D}_i\breve{\theta}_i}{\mathfrak{D}t} v_i d\mathsf{R}\phi_i dV \tag{B.21}$$

and

$$\frac{D_i M_i}{Dt} = \int_{\Delta V}\int_0^\infty \frac{\mathfrak{D}_i\breve{m}_i}{\mathfrak{D}t} v_i d\mathsf{R}\phi_i dV = 0 \tag{B.22}$$

Appendix C. Zener pinning force and work

C.1. Classical Zener pinning

The classical relation for pinning force was derived by Zener as reported by Smith (1948) for a flat grain boundary of one phase impinging on an inclusion of the other phase (see Fig. 3); see also Hellman and Hillert (1975), Wörner and Cabo (1987), Rios (1987), Hillert (1988), Harun et al. (2006) and Roberts (2008). In this treatment, the grain boundary intersects the surface of the inclusion of radius r and the grain boundary surface tension γ_i (force per unit length) pulls on the inclusion tangent to the grain boundary and all along the intersection curve. Assuming local dynamic equilibrium at the intersection itself, then the grain boundary intersects at the wetting angle; since surface tension γ_1 on the interface between phases is the same on either side of this intersection, the wetting angle would be 90°; i.e., at the intersection, the grain boundary would be normal to the inclusion's surface. The net force from the grain boundary surface tension, integrated around the intersection curve of length $2\pi r\sin\theta$ (where θ is defined in Fig. 3 or Fig. C.1), is only along the symmetry axis and thus normal to the grain boundary, with a net force of

$$f_n = \gamma_i 2\pi r\cos\theta\sin\theta \tag{C.1}$$

This force is often assumed to be at its maximum regardless of the intersection or contact position (Smith, 1948; Harun et al., 2006), which occurs at $\theta = 45°$; however this assumption merely gives a scaling law for the magnitude of the normal force f_n and is not readily justified. The actual normal force can act in opposite directions on the grain boundary depending on whether the boundary is above or below the mid-plane of the inclusion; indeed the inclusion is known to pull up on the boundary initially on first contact (Smith, 1948; Harun et al., 2006) and then pin the boundary only as it moves past the inclusion. The net pinning force is only due to the fact that the initial contact of a moving boundary with an inclusion is asymmetric with its departure from the inclusion. In particular, first contact occurs when the grain boundary is a distance r from the inclusion's center, while departure occurs when the boundary is a distance significantly greater than r from the inclusion center, since the grain boundary is already stuck to the inclusion. Moreover, the curvature of the grain boundary itself (assumed to be zero in Zener's original theory) breaks the symmetry of the approach and

departure (Hellman and Hillert, 1975; Wörner and Cabo, 1987; Harun et al., 2006).

The derivation of the total pinning force that the inclusion exerts on the grain boundary as it passes around the inclusion is complex and we only summarize it here (seeHellman and Hillert, 1975; Wörner and Cabo, 1987, for details). If s is the distance between the center of the inclusion and the unperturbed grain boundary (see Fig. C.1), then the pinning force is a function of $U = \mathrm{R}/r$ and $u = s/r$. During passage around the inclusion the average pinning force is obtained after expressing $\theta(U,u)$ and computing

$$\langle f_n \rangle = \frac{1}{\mathrm{R}_M - \mathrm{R}_m} \int_{\mathrm{R}_m}^{\mathrm{R}_M} f_n ds = \frac{\gamma_i \pi r^2}{\mathrm{R}_M - \mathrm{R}_m} \int_{U_m}^{U_M} \sin(2\theta(U,u)) du \qquad \text{(C.2)}$$

where $U_m = \mathrm{R}_m/r$ and $U_M = \mathrm{R}_M/r$ are the minimum and maximum relative radii at which the grain boundary is in contact with the inclusion; i.e., if the outwardly moving grain boundary has a radius less than R_m then it has not yet made contact with the inclusion in which case it is spherical and the inclusion is outside the grain; if the grain boundary has a radius R_M it has departed from the grain, it is also spherical and the inclusion is now inside the grain. If the grain boundary were to pass around the inclusion without sticking to it then $\mathrm{R}_M - \mathrm{R}_m$ would equal $2r$; however because sticking causes the first contact of the grain boundary with the inclusion to differ from departure, then $\mathrm{R}_M - \mathrm{R}_m > 2r$. This complex problem has a simple solution because the shape of the spherical interface around the single spherical inclusion is given by a catenoidal shape (Hellman and Hillert, 1975) and thus the function $\theta(U,u)$ is analytic.

However, we require the net Zener pinning force on an ensemble of inclusions. Assuming that inclusion size is tightly distributed around the size r, then the number of inclusions in a control volume ΔV dispersed through phase i is approximately $N = (1-\phi_i)\Delta V/(\frac{4}{3}\pi r^3)$ and thus the number of inclusions per unit volume is simply $n = 3(1-\phi_i)/(4\pi\ r^3)$. Assuming inclusions are randomly distributed, then the number of inclusions within range of touching the grain boundary with area $\breve{\mathrm{A}}$ is $n\breve{\mathrm{A}}(\mathrm{R}_M - \mathrm{R}_m) = 3(1-\phi_i)\breve{\mathrm{A}}(\mathrm{R}_M - \mathrm{R}_m)/(4\pi r^3)$. The total average component of force acting normal to the grain boundary (and thus like an effective pressure force resisting boundary migration) due to all inclusions touching the grain boundary is thus

$$F_n = \langle f_n \rangle n\breve{\mathrm{A}}(\mathrm{R}_M - \mathrm{R}_m) = \frac{3\gamma_i(1-\phi_i)\breve{\mathrm{A}}}{4r} \int_{U_m}^{U_M} \sin(2\theta(U,u)) du$$
$$= \frac{3\gamma_i(1-\phi_i)\breve{\mathrm{A}}}{2r} \mathcal{P}(\mathrm{R}/r) \qquad \text{(C.3)}$$

where $\mathcal{P}(U) = \frac{1}{2}\int_{U_m}^{U_M} \sin(2\theta(U,u)) du$.

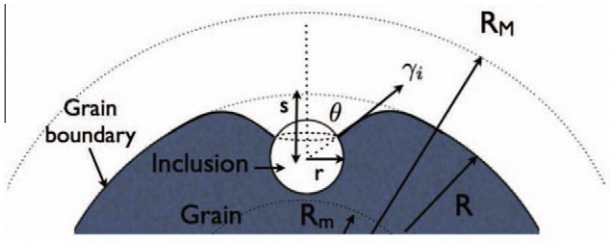

Fig. C.1. Sketch of Zener pinning configuration in which a grain boundary of one phase moves past an inclusion composed of the other phase. As opposed to Fig. 3, which shows the simple and classical flat-boundary configuration (Smith, 1948), this figure shows the configuration with a curved grain boundary and in which the first contact and departure distances between grain boundary and inclusion are delineated. In either case the surface tension of the grain boundary γ_i acts on the intersection between the inclusion and the grain boundary. The grain boundary first connects with the inclusion when it reaches a size $\mathrm{R} = \mathrm{R}_m$ and departs from the inclusion when it reaches $\mathrm{R} = \mathrm{R}_M$.

The seminal Zener-pinning paper of Smith (1948) assumed that approach and departure distances between the grain boundary and inclusion are effectively symmetric, but that the inclusion exerts the maximal pinning force, in which case $U_M = (\mathrm{R}+r)/r$, $U_m = (\mathrm{R}-r)/r$ and $\sin(2\theta) = 1$, which leads to a constant $\mathcal{P}(\mathrm{R}/r) = 1$. Subsequent papers, however, have shown $\mathcal{P}$ to be a positive and monontonically increasing function of R/r (Hellman and Hillert, 1975; Wörner and Cabo, 1987), which implies that Zener pinning is more efficient for large grains than for small ones, which is verified experimentally (see Wörner and Cabo, 1987; Harun et al., 2006). A large number of forms for $\mathcal{P}(U)$ have been proposed from experiments or simulations in the metallurgical literature (see Manohar et al., 1998); however, we find in Section 3 that a simple linear $\mathcal{P}(U)$ provides the best fit to experimental data for grain growth in synthetic peridotites (see also Appendix F.4).

Finally, it should be noted that the classical Zener pinning arguments are most relevant for small minor-phase impurities on the major phase grain boundaries, as occurs in metallurgical applications; in this limit r would be uniquely described by the minor phase characteristic or mean grain-size $\mathcal{R}_j$, where j indicates the phase for which $\phi_j \ll 1$. This limit is also born out in our comparison with experiments in Section 3. For larger secondary phase volume fractions the classic model and assumptions are less valid; in this case the pinning radius r is likely independent or not uniquely dependent on grain-size, as illustrated below and also with a statistical mixture model in Appendix G. However, the essential form of the macroscopic Zener pinning force is largely independent of these model assumptions.

C.2. Zener pinning: effective grain boundary shape and energy

Although the thermodynamics of our system is explored fully in Appendix E, we briefly discuss the energy contribution of Zener pinning here. In particular, given the pinning force F_n exerted by the interface on a given grain boundary by (2), then the work done by the grain boundary to grow against this force over a distance $d\mathrm{R}$ is $F_n d\mathrm{R}$. The total increment in grain-boundary energy during grain growth by $d\mathrm{R}$ and involving an increase in grain-boundary area $d\breve{\mathrm{A}}$ is therefore

$$d\breve{\xi}_i = \gamma_i \left(d\breve{\mathrm{A}} + \frac{3(1-\phi_i)}{2r} \mathcal{P}\breve{\mathrm{A}} d\mathrm{R} \right) \qquad \text{(C.4)}$$

and the rate of change of grain-boundary energy is

$$\frac{\mathrm{d}_i \breve{\xi}_i}{dt} = \gamma_i \left(\frac{\mathrm{d}_i \breve{\mathrm{A}}}{dt} + \frac{3(1-\phi_i)}{2r} \mathcal{P}\breve{\mathrm{A}} \frac{\mathrm{d}_i \mathrm{R}}{dt} \right) = \gamma_i \breve{\mathcal{C}}_i \frac{\mathrm{d}_i \breve{\mathrm{V}}}{dt} \qquad \text{(C.5)}$$

where

$$\breve{\mathcal{C}}_i = \frac{2}{\mathrm{R}} + \frac{3(1-\phi_i)}{2r} \mathcal{P} \qquad \text{(C.6)}$$

is an effective grain-boundary curvature, and we have used the identities $d\breve{\mathrm{A}}/d\breve{\mathrm{V}} = 2/\mathrm{R}$, and $\breve{\mathrm{A}} d\mathrm{R} = d\breve{\mathrm{V}}$ (i.e., using $\breve{\mathrm{A}} = 4\pi\mathrm{R}^2$ and $\breve{\mathrm{V}} = \frac{4}{3}\pi\mathrm{R}^3$). Likewise the total energy stored on the grain boundary during growth of the entire grain is

$$\breve{\xi}_i = \gamma_i \left(\breve{\mathrm{A}} + \frac{3(1-\phi_i)}{2r} \int_0^{\mathrm{R}} \mathcal{P}\breve{\mathrm{A}} d\mathrm{R} \right) = \gamma_i \breve{\mathcal{A}}_i \qquad \text{(C.7)}$$

where $\breve{\mathcal{A}}_i$ is an effective grain boundary surface area. Note that

$$\breve{\mathcal{C}}_i = \frac{\partial \breve{\mathcal{A}}_i}{\partial \breve{\mathrm{V}}} = \left(\frac{d\breve{\mathrm{V}}}{d\mathrm{R}} \right)^{-1} \frac{\partial \breve{\mathcal{A}}_i}{\partial \mathrm{R}} = \frac{1}{\breve{\mathrm{A}}} \frac{\partial \breve{\mathcal{A}}_i}{\partial \mathrm{R}} \qquad \text{(C.8)}$$

which recovers (C.6).

These thermodynamic relations show that pinning acts to increase the grain-boundary's curvature and surface area by

distorting it (see also (3)). The increased curvature induces a larger effective grain-boundary surface tension force that increases the grain's internal pressure and hence chemical potential; this consequently enhances diffusion of atoms out of the grain, thereby hindering grain growth and even promoting shrinkage. The distortional effect on surface area similarly facilitates damage by reducing the surface energy contrast between a large grain before fission and the smaller resulting grains after fission (see Section 2.2.2 for further discussion). These effects are essential to how Zener pinning is incorporated into a continuum macroscopic theory.

Finally, throughout this paper we generally assume that the surface energies for grain boundaries of a single phase γ_i, and between different phases along their interface γ_1 are constants. In principle they might be functions of temperature and chemical composition, which then invokes surface entropies and chemical potentials (i.e., rather than the surface energy only involving reversible work). However, these effects are not critical for our purposes and are therefore neglected.

C.3. Pinning force due to grain-boundary splitting

The classical approach of Zener pinning assumes that the impeding force is due to small particles and impurities on the grain boundaries; however, this assumption is not necessarily applicable to pinning in assemblages of minerals with commensurate volume fractions and grain-sizes. Large grains of one phase impinging on smaller grains of the other phase do appear to undergo boundary distortions analogous to the traditional Zener pinning assumption (e.g., see Fig. 2, left panel). In assemblages of, for example, natural and synthetic peridotite (Hiraga et al., 2010), where the grain-size and/or volume fractions of minerals are comparable, the grains of different minerals appear to grow along each other's grain-boundaries, effectively splitting the boundaries and squeezing in between each others grains, without ever engulfing opposite grains (Fig. C.2). In this case, the grains growing along the opposite phase's grain boundaries develop protuberances or ridges, which experience resistive forces comparable to the pinning force. The force of resistance to growth of these sharp features can be examined by a simple model of a ridge-like protuberance extending into the opposite phase's grain boundary, as illustrated in Fig. C.2.

For simplicity and physical scaling, we consider a single spherical grain composed of phase i growing into the grain boundaries of surrounding phase j. The protuberances are assumed to be triangular ridges of height y, inner angle 2θ, and an arc-length given by how the phase j grains are in contact with the single phase i grain. For example, in the model considered in Fig. C.2, the spherical grain has sectoral contact surfaces with four grains of phase j, and thus has four ridges of arc-length $\pi \mathsf{R}_i$ (where R_i is identified as the radius of grain of phase i).

The total surface tension force resisting growth of one ridge is $(2\gamma_1 \cos\theta - \gamma_j)\pi \mathsf{R}_i$. An equilibrium dihedral angle θ is reached if there were no other forces and this surface tension force is zero. However since the grain is growing, it is in disequilibrium and we assume the ridge has grown past the dihedral-angle equilibrium point and the surface tension forces on the ridge are resisting further growth (before reaching this dihedral-angle point, surface tension on the ridge would accelerate growth by drawing the ridge into the grain boundary, i.e., drive "wetting" of the grain boundary). The number of ridges on the spherical grain is the number of grains of phase j in contact with the grain of phase i, and this is approximately the number density of grains of phase j times the volume in which they might be in contact with the single grain, i.e., $\phi_j/(\frac{4}{3}\pi \mathsf{R}_j^3) \times \breve{\mathsf{A}}_i \mathsf{R}_j = 3(1-\phi_i)\breve{\mathsf{A}}_i/\breve{\mathsf{A}}_j$ given that $\breve{\mathsf{A}}_j = 4\pi \mathsf{R}_j^2$. The total force resisting grain growth on the single grain of phase i is thus

$$F_n = (2\gamma_1 \cos\theta - \gamma_j)\pi \mathsf{R}_i \frac{3(1-\phi_i)\breve{\mathsf{A}}_i}{\breve{\mathsf{A}}_j} \tag{C.9}$$

However, we wish to pose the force F_n in terms of the interface area density α. The interface area due to one grain of phase j in contact with the spherical grain of phase i is the resulting ridge surface area $2y\pi \mathsf{R}_i/\cos\theta$ plus any "flat" contact area, which we write as $c\breve{\mathsf{A}}_i$ where $c < 1$. The total interface surface area in volume V is this single contact area $(2y\pi \mathsf{R}_i/\cos\theta + c\breve{\mathsf{A}}_i)$ times the number of ridges on the spherical grain $(3(1-\phi_i)\breve{\mathsf{A}}_i/\breve{\mathsf{A}}_j)$ times the number of similar spherical grains of phase i in the volume $(\phi_i V/(\frac{4}{3}\pi \mathsf{R}_i^3))$. Thus the interface area per volume is

$$\alpha = (2y\pi \mathsf{R}_i/\cos\theta + c\breve{\mathsf{A}}_i)\frac{3(1-\phi_i)\breve{\mathsf{A}}_i}{\breve{\mathsf{A}}_j}\frac{3\phi_i}{\mathsf{R}_i\breve{\mathsf{A}}_i} \tag{C.10}$$

We can thus write the force resisting grain growth as

$$F_n = (2\gamma_1 \cos\theta - \gamma_j)\frac{\alpha}{3\phi_i}\breve{\mathsf{A}}_i \frac{\mathsf{R}_i}{2y/\cos\theta + 4c\mathsf{R}_i} \tag{C.11}$$

The surface tensions γ_1, γ_i and γ_j are related or commensurate and thus we assume that the resisting force $2\gamma_1 \cos\theta - \gamma_j > 0$ is a fraction of the grain-boundary surface tension, i.e., equals $b\gamma_i$ where $0 < b < 1$. Moreover, as discussed in Appendix A we define $\alpha = \mathcal{F}\eta(\phi) = \eta/r$ (see (A.4)) and assume $\eta = 3\phi_i\phi_j = 3\phi_i(1-\phi_i)$. Taking these assumptions together the force resisting grain growth is

$$F_n = \frac{b\gamma_i(1-\phi_i)\breve{\mathsf{A}}_i}{r} Y(\mathsf{R}_i) \tag{C.12}$$

where we generalize $\mathsf{R}_i/(2y\cos\theta + 4c\mathsf{R}_i)$ to be a monotonically increasing function $Y(\mathsf{R})$ as is $\mathcal{P}$ in the simple Zener pinning model.

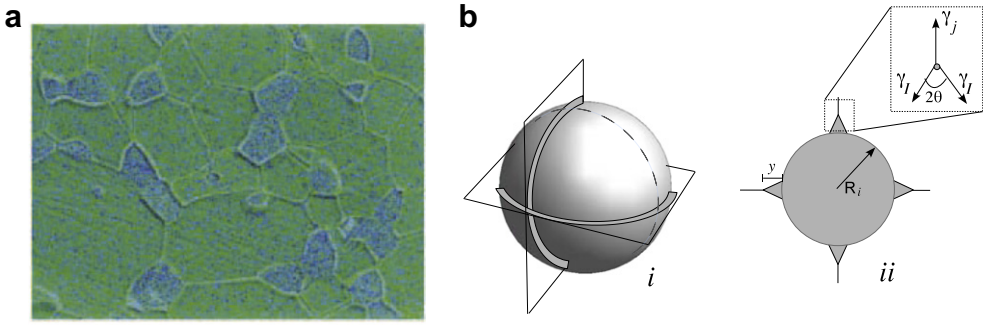

Fig. C.2. Grain growth in assemblages of two minerals with comparable grain size and/or volume fraction occurs along the opposite minerals grain boundaries. Growing grains develop polygonal or polyhedral shapes with protuberances splitting the opposite mineral's grain boundary, as shown in an example of synthetic peridotite (a) from Hiraga et al. (2010) where blue [dark grey] is enstatite/pyroxene, green [light grey] is forsterite/olivine, and the average grainsize is approximately 1 μm. A simple model (b) illustrates these protuberances as ridges circumscribing a spherical grain growing between four other grains (i) with a cross section corresponding to the dashed line, and a force vector diagram showing surface tension forces on one cross-section of a ridge (ii) which is used to estimate the force resisting grain growth. (For interpretation of the references to colour in this figure legend, the reader is referred to the web version of this article.)

In a mixture of grains of comparable volume fractions and grain-sizes this model of grain growth inhibition by grain-boundary splitting should be symmetric between phases (i.e., each of their grains grow against some combination of Zener pinning and grain boundary splitting). The final relation for this effective blocking or pinning force (C.12) is not exactly the same as that obtained for the classical Zener pinning model with small inclusions (C.3), but the form and dependence on interface density α (or interface roughness r), on volume fraction of opposing phase $1-\phi_i$, and on grain-size R are comparable. The consistency between this model of grain boundary splitting with the Zener pinning model argues for employing a single general law for the grain pinning or impeding force as shown by (2).

Appendix D. Momentum conservation

Conservation of momentum for creeping two-phase flow has been dealt with extensively in previous studies (McKenzie, 1984, 1985, 1987; McKenzie and Holness, 2000; Spiegelman, 1993a,b,c; Bercovici et al., 2001a; Bercovici and Ricard, 2003; Katz, 2008). Allowing for each phase to have internal grain boundaries with surface energy γ_i yields an additional effective pressure due to the squeezing of grains by their own grain-boundary (Ricard and Bercovici, 2009); the total force balance equation is thus

$$0 = -\nabla(\phi_i P_i) + \nabla(\phi_i\gamma_i\mathcal{K}_i) + \nabla\cdot(\phi_i\underline{\boldsymbol{\tau}}_i) + \rho_i\phi_i\mathbf{g} + \mathbf{h}_i \tag{D.1}$$

where P_i is the pressure in phase i, $\underline{\boldsymbol{\tau}}_i$ is the viscous stress, $\mathbf{g}$ is gravity, $\mathbf{h}_i$ is the interphase interaction force, and $\mathcal{K}_i = \int_0^\infty \breve{C}_i\breve{V} v_i d\mathrm{R}$ is the average grain-boundary curvature in phase i (Ricard and Bercovici, 2009).

In general, and as specified in Bercovici et al. (2001a) and Bercovici and Ricard (2003), the interaction force is

$$\mathbf{h}_i = c\Delta\mathbf{v}_i + P^*\nabla\phi_i + \omega_i\nabla(\gamma_\imath\alpha) \tag{D.2}$$

where c is a drag coefficient, P^* is an effective interface pressure, α is the interface area density as defined already in (A.3) and (A.4); $\gamma_\imath$ is now, in the continuum formulation, the effective surface tension on the interface between phases, which differs slightly from the microscopic description (see Appendix E.1), and ω_i is the weighting factor for how much the interface surface tension and energy are embedded in phase i (where $\sum_{i=1}^2\omega_i = 1$). Moreover, we prescribe, for any quantity Q, that $\Delta Q_i = (\overline{Q} - Q_i)/(1-\phi_i)$ where $\overline{Q} = \sum_i\phi_i Q_i$ so that $\Delta Q_1 = Q_2 - Q_1$ and $\Delta\ Q_2 = Q_1 - Q_2$.

Following the same arguments for determining the interface pressure P^* as in Bercovici et al. (2001a) and Bercovici and Ricard (2003), and defining an effective internal pressure $\Pi_i = P_i + \gamma_i\mathcal{K}_i$, Eq. (D.1) becomes

$$\begin{aligned} 0 = &-\nabla(\phi_i\Pi_i) + \nabla\cdot(\phi_i\underline{\boldsymbol{\tau}}_i) + \rho_i\phi_i\mathbf{g} + c\Delta\mathbf{v}_i \\ &+ \left(\sum_j(1-\omega_j)\Pi_j\right)\nabla\phi_i + \omega_i\nabla(\gamma_\imath\alpha) \end{aligned} \tag{D.3}$$

or equivalently

$$\begin{aligned} 0 = &-\phi_i\nabla\Pi_i + \nabla\cdot(\phi_i\underline{\boldsymbol{\tau}}_i) + \rho_i\phi_i\mathbf{g} + c\Delta\mathbf{v}_i \\ &+ \omega_i(\Delta\Pi_i\nabla\phi_i + \nabla(\gamma_\imath\alpha)) \end{aligned} \tag{D.4}$$

For a specific mixture of solid silicates as in peridotite we eventually assume that $\Delta\mathbf{v}_i \approx 0$. In this case, since there is only one velocity $\mathbf{v}_i = \mathbf{v}$, we need only one momentum equation, in particular the sum of (D.3) over i:

$$0 = -\nabla\overline{\Pi} + \nabla\cdot\bar{\underline{\boldsymbol{\tau}}} + \bar{\rho}\mathbf{g} + \nabla(\gamma_\imath\alpha) \tag{D.5}$$

which is as also shown in (4b). Although we would only use $\bar{\underline{\boldsymbol{\tau}}} = \sum_i\phi_i\underline{\boldsymbol{\tau}}_i$, the stresses $\underline{\boldsymbol{\tau}}_i$ are still determined by the rheology of each phase according to (4c).

Appendix E. Thermodynamics of two-phase grained media

E.1. Energy conservation

The total energy of both phases inside a control volume ΔV is

$$E = \int_{\Delta V}\left(\sum_i\phi_i\int_0^\infty\left(\breve{m}_i\breve{\mathcal{E}}_i + \gamma_i\breve{\mathcal{A}}_i\right)v_i d\mathrm{R} + (\tilde{\gamma}_\imath - \sum_i\gamma_i)\alpha\right)dV \tag{E.1}$$

where $\breve{\mathcal{E}}_i$ is the specific internal energy (energy per mass) of a grain inside phase i, $\breve{\mathcal{A}}_i$ is the effective grain-boundary surface area as defined in (C.7).

Moreover, $\tilde{\gamma}_\imath$ is the true interface surface tension, and we remove the grain-boundary energy that has been replaced by interface (the $-\sum_i\gamma_i\alpha$ term). These two interface effects however add simply, which allows us to define an effective interface energy $\gamma_\imath = \tilde{\gamma}_\imath - \sum_i\gamma_i$; we assert that $\gamma_\imath$ is positive or else complete mixing would be a minimum energy state and hence spontaneous (i.e., the phases would be miscible in each other). Lastly, we have neglected kinetic energy to be consistent with the assumption of creeping flow.

The rate of change of this energy, assuming the control volume is closed and deformable, and also employing (B.16) and (C.5), is

$$\begin{aligned} \frac{DE}{Dt} &= \int_{\Delta V}\left(\sum_i\phi_i\int_0^\infty\left[\left(\frac{\mathrm{d}_i\breve{m}_i\breve{\mathcal{E}}_i}{\mathrm{d}t} + \gamma_i\breve{C}_i\frac{\mathrm{d}_i\breve{V}}{\mathrm{d}t}\right)v_i + \left(\breve{m}_i\breve{\mathcal{E}}_i + \gamma_i\breve{\mathcal{A}}_i\right)\Gamma_i\right]d\mathrm{R} + \gamma_\imath\frac{\tilde{D}\alpha}{Dt}\right)dV \\ &= \int_{\Delta V}\left(\sum_i\phi_i\int_0^\infty\frac{\mathfrak{D}_i}{\mathfrak{D}t}\left(\breve{m}_i\breve{\mathcal{E}}_i + \gamma_i\breve{\mathcal{A}}_i\right)v_i d\mathrm{R} + \gamma_\imath\frac{\tilde{D}\alpha}{Dt}\right)dV \end{aligned} \tag{E.2}$$

where we have used the definition of $\mathfrak{D}_i/\mathfrak{D}t$ from (B.20) and we prescribe

$$\frac{\tilde{D}}{Dt} = \sum_i\omega_i\frac{D_i}{Dt} \tag{E.3}$$

as the material derivative traveling with the interface between phases (see Bercovici and Ricard, 2003), and we have used the assumption that the phases are incompressible (i.e., $D(dV)/Dt = 0$).

Alternatively the Gibbs relationship for an energy increment in the same control volume is (see Ricard and Bercovici, 2009)

$$\begin{aligned} dE = \int_{\Delta V}\Bigg(\sum_i\phi_i\int_0^\infty\Big[&\left(Td(\breve{m}_i\breve{\mathcal{S}}_i) - \breve{P}_i d(\breve{m}_i/\rho_i) + \breve{\mu}_i d\breve{m}_i + \gamma_i d\breve{\mathcal{A}}_i\right)v_i \\ &+\left(T\breve{m}_i\breve{\mathcal{S}}_i - \breve{P}_i\breve{m}_i/\rho_i + \breve{\mu}_i\breve{m}_i + \gamma_i\breve{\mathcal{A}}_i\right)\Gamma_i dt\Big]d\mathrm{R} + \gamma_\imath d\alpha\Bigg)dV \end{aligned} \tag{E.4}$$

where $\breve{\mathcal{S}}_i$ is the specific entropy of a grain in phase i, $\breve{P}_i$ is the pressure inside a grain, $\breve{\mu}_i$ is chemical potential in a grain, and T is the temperature within the control volume, the components of which are assumed to be in local thermal equilibrium. Using (E.4) to write DE/Dt and subtracting this from (E.2) yields

$$\begin{aligned} \int_{\Delta V}\Bigg(\sum_i\phi_i\int_0^\infty\Bigg[&\breve{m}_i\left(\frac{\mathrm{d}_i\breve{\mathcal{E}}_i}{\mathrm{d}t} - T\frac{\mathrm{d}_i\breve{\mathcal{S}}_i}{\mathrm{d}t} + \breve{P}_i\frac{\mathrm{d}_i(1/\rho_i)}{\mathrm{d}t}\right) \\ &+\frac{\mathfrak{D}_i\breve{m}_i}{\mathfrak{D}t}\left(\breve{\mathcal{E}}_i - T\breve{\mathcal{S}}_i + \breve{P}_i/\rho_i - \mu_i\right)\Bigg]v_i d\mathrm{R}\Bigg)dV = 0 \end{aligned} \tag{E.5}$$

Allowing for each parenthetical term in the integrand to be zero independently (see Ricard and Bercovici, 2009) leads to a Gibbs relation for individual grain energy

$$\frac{\mathrm{d}_i\breve{\mathcal{E}}_i}{\mathrm{d}t} = T\frac{\mathrm{d}_i\breve{\mathcal{S}}_i}{\mathrm{d}t} - \breve{P}_i\frac{\mathrm{d}_i(1/\rho_i)}{\mathrm{d}t} \quad \text{or} \quad d\breve{\mathcal{E}}_i = Td\breve{\mathcal{S}}_i - \breve{P}_i d(1/\rho_i) \tag{E.6}$$

and the grain chemical potential

$$\breve{\mu}_i = \breve{\mathcal{E}}_i - T\breve{\mathcal{S}}_i + \breve{P}_i/\rho_i \tag{E.7}$$

respectively. Since the phases are incompressible, then $d\rho_i = 0$ and $d\breve{\mathcal{E}}_i = Td\breve{\mathcal{S}}_i$. Assuming expansion of scales applies within a grain then $\breve{\mathcal{E}}_i = T\breve{\mathcal{S}}_i$ in which case $\breve{\mu}_i = \breve{P}_i/\rho_i$.

The conservation of energy, accounting for sources of work and heat acting on or within a fixed but open control volume ΔV with surface ΔA, requires that (see also Bercovici and Ricard, 2003; Ricard and Bercovici, 2009)

$$\begin{aligned}\frac{\partial E}{\partial t} &= \int_{\Delta V}\left(\sum_i\int_0^\infty\left(\frac{\partial(\breve{m}_i\breve{\mathcal{E}}_i\phi_i v_i)}{\partial t}+\gamma_i\frac{\partial(\breve{\mathcal{A}}_i\phi_i v_i)}{\partial t}\right)d\mathrm{R}+\gamma_1\frac{\partial\alpha}{\partial t}\right)dV\\ &= -\int_{\Delta A}\left(\sum_i\phi_i\int_0^\infty(\breve{m}_i\breve{\mathcal{E}}_i+\gamma_i\breve{\mathcal{A}}_i)v_i d\mathrm{R}\mathbf{v}_i\cdot\hat{\mathbf{n}}+\gamma_1\alpha\tilde{\mathbf{v}}\cdot\hat{\mathbf{n}}\right)dA\\ &\quad+\int_{\Delta V}\sum_i\mathbf{v}_i\cdot\mathbf{g}\rho_i\phi_i dV+\int_{\Delta A}\sum_i\mathbf{v}_i\cdot(-\Pi_i\underline{\mathbf{I}}+\underline{\boldsymbol{\tau}}_i)\cdot\hat{\mathbf{n}}dA\\ &\quad+\int_{\Delta A}\gamma_1\alpha\tilde{\mathbf{v}}\cdot\hat{\mathbf{n}}dA+\int_{\Delta V}Q dV-\int_{\Delta A}\mathbf{q}\cdot\hat{\mathbf{n}}dA\end{aligned}\tag{E.8}$$

where $\tilde{\mathbf{v}}=\sum_i\omega_i\mathbf{v}_i$ is the effective velocity of the interface between phases, and we include the work done by grain boundary surface tension on the surface of the control volume within the work done by the effective pressure Π_i. Moreover, while both the heat production Q and heat flow $\mathbf{q}$ might be different for separate phases (e.g., Q could be written as $\sum_i\phi_i Q_i$) we only retain these terms symbolically until we drop them later, since they are not crucial for our intended application.

In the standard method of reducing the energy balance law, we invoke Green's integral theory to remove the volume integral (since the volume ΔV is arbitrary), employ (A.5) and (B.11) to contract the Reynolds transport terms, and use $\sum_i\mathbf{v}_i\cdot$ of (D.3) to eliminate mechanical work terms, eventually arriving at

$$\begin{aligned}&\sum_i\phi_i\int_0^\infty\frac{\mathfrak{D}_i}{\mathfrak{D}t}\left(\breve{m}_i\breve{\mathcal{E}}_i+\gamma_i\breve{\mathcal{A}}_i\right)v_i d\mathrm{R}+\gamma_1\frac{\widetilde{D}\alpha}{Dt}=c(\Delta v)^2\\ &\quad+\sum_i\phi_i\underline{\boldsymbol{\tau}}_i:\nabla\mathbf{v}_i-\Delta\Pi\frac{\widetilde{D}\phi}{Dt}+Q-\nabla\cdot\mathbf{q}\end{aligned}\tag{E.9}$$

where recall that $\phi=\phi_1$ (and $\phi_2=1-\phi$) and we have again used (B.20), and we note that $(\Delta v)^2=\Delta\mathbf{v}_i\cdot\Delta\mathbf{v}_i$ while $\Delta\Pi=\Delta\Pi_1=\Pi_2-\Pi_1$. Employing the Gibbs relation (E.4), written more compactly with the operator $\mathfrak{D}_i/\mathfrak{D}t$, (E.9) becomes

$$\begin{aligned}&\sum_i\phi_i\int_0^\infty\left(T\frac{\mathfrak{D}_i(\breve{m}_i\breve{\mathcal{S}}_i)}{\mathfrak{D}t}-\breve{P}_i\frac{\mathfrak{D}_i(\breve{m}_i/\rho_i)}{\mathfrak{D}t}+\breve{\mu}_i\frac{\mathfrak{D}_i\breve{m}_i}{\mathfrak{D}t}+\gamma_i\frac{\mathfrak{D}_i\breve{\mathcal{A}}_i}{\mathfrak{D}t}\right)v_i d\mathrm{R}\\ &\quad+\gamma_1\frac{\widetilde{D}\alpha}{Dt}=c(\Delta v)^2+\overline{\Psi}-\Delta\Pi\frac{\widetilde{D}\phi}{Dt}+Q-\nabla\cdot\mathbf{q}\end{aligned}\tag{E.10}$$

where

$$\overline{\Psi}=\sum_i\phi_i\underline{\boldsymbol{\tau}}_i:\nabla\mathbf{v}_i\tag{E.11}$$

is the total deformational work done on a point in space (i.e., an infinitesimal control volume). We have not included the drag work $c(\Delta v)^2$ in $\overline{\Psi}$ since this accounts for how the actual work exerted on the volume is transmitted internally between phases, and thus does not constitute an external source of work and energy. In later sections we will also refer to deformational work within each phase $\Psi_i=\underline{\boldsymbol{\tau}}_i:\nabla\mathbf{v}_i$ such that $\overline{\Psi}=\sum_i\phi_i\Psi_i$, as well as to work within each grain $\breve{\Psi}_i=\underline{\breve{\boldsymbol{\tau}}}_i:\nabla\mathbf{v}_i$ such that

$$\overline{\Psi}=\sum_i\phi_i\int_0^\infty\breve{\Psi}_i\breve{\mathcal{V}}v_i d\mathrm{R}\tag{E.12}$$

where $\underline{\breve{\boldsymbol{\tau}}}_i$ can be, in principle, distinct between grains because of the grain-size dependent viscosity.

E.2. Entropy production

We use the energy balance equation derived in the previous section along with the Second Law of Thermodynamics to infer the rate of entropy production. Since this production is necessarily positive, we can later use non-equilibrium thermodynamics to infer phenomenological laws and damage relationships (see Appendix E.3).

The total entropy in the control volume ΔV is

$$\mathcal{S}=\int_{\Delta V}\sum_i\phi_i\int_0^\infty\breve{m}_i\breve{\mathcal{S}}_i v_i d\mathrm{R}dV\tag{E.13}$$

The Second Law of Thermodynamics states that internal entropy production must be greater than or equal to zero, which is written as

$$\frac{D\mathcal{S}}{Dt}=\int_{\Delta V}\sum_i\phi_i\int_0^\infty\frac{\mathfrak{D}_i(\breve{m}_i\breve{\mathcal{S}}_i)}{\mathfrak{D}t}v_i d\mathrm{R}dV\geqslant-\int_{\Delta A}\frac{1}{T}\mathbf{q}\cdot\hat{\mathbf{n}}dA\tag{E.14}$$

where $-(\mathbf{q}/T)\cdot\hat{\mathbf{n}}$ is the external entropy flux through the surface of the closed volume (e.g., due to conduction, radiation, etc). Using (E.10) (divided by T, which is assumed uniform across grains and phases) to eliminate $\mathfrak{D}_i(\breve{m}_i\breve{\mathcal{S}}_i)/\mathfrak{D}t$ from (E.14), eventually leads to

$$\begin{aligned}&\sum_i\phi_i\int_0^\infty\left(\left(\breve{P}_i/\rho_i-\breve{\mu}_i\right)\frac{\mathfrak{D}_i\breve{m}_i}{\mathfrak{D}t}-\gamma_i\frac{\mathfrak{D}_i\breve{\mathcal{A}}_i}{\mathfrak{D}t}\right)v_i d\mathrm{R}-\gamma_1\frac{\widetilde{D}\alpha}{Dt}-\Delta\Pi\frac{\widetilde{D}\phi}{Dt}\\ &\quad+c(\Delta v)^2+\overline{\Psi}+Q-\frac{1}{T}\mathbf{q}\cdot\nabla T\geqslant 0\end{aligned}\tag{E.15}$$

Following (E.7) we argue that, because the phases are incompressible and by appealing to expansion of scales (over the scales in which T is uniform), then $\breve{\mu}_i=\breve{P}_i/\rho_i$, in which case (E.15) becomes the final total entropy production relation

$$\begin{aligned}&-\sum_i\phi_i\gamma_i\int_0^\infty\frac{\mathfrak{D}_i\breve{\mathcal{A}}_i}{\mathfrak{D}t}v_i d\mathrm{R}-\gamma_1\frac{\widetilde{D}\alpha}{Dt}-\Delta\Pi\frac{\widetilde{D}\phi}{Dt}+c(\Delta v)^2+\overline{\Psi}\\ &\quad+Q-\frac{1}{T}\mathbf{q}\cdot\nabla T\geqslant 0\end{aligned}\tag{E.16}$$

from which we construct nonequilibrium thermodynamic constraints and phenomenological laws for grain and interface coarsening and damage.

E.3. Nonequilibrium thermodynamics and damage laws

We can identify in (E.16) the various entropy sources associated with the rate of change in grain and interface surface areas driven by surface tension, deformational work, heat production and lastly thermal diffusion. Applications of this theory to lithospheric shear localization, however, do not require considerations of heat production or transfer and thus we hereafter neglect both Q and $\mathbf{q}$. Moreover, we further assume that, in a polymineralic material where both phases are of comparable viscosity, separation velocity $\Delta\mathbf{v}_i$ between phases is small enough to make $c(\Delta v)^2$ negligible relative to other heat sources; indeed, for later applications we will, for simplicity, assume $\Delta\mathbf{v}_i\approx 0$. (Indeed, when the phase velocities $\mathbf{v}_i$ are identified with the macroscopic mixture velocity $\mathbf{v}$, the interface velocity $\tilde{\mathbf{v}}$ also becomes $\mathbf{v}$, and the material derivatives relative to phases or interfaces, i.e., D_i/Dt and $\widetilde{D}/Dt$, simply become the bulk material derivative $D/Dt=\partial/\partial t+\mathbf{v}\cdot\nabla$.) Finally, we assume that the kinetic processes governing changes in grain-size within phases and changes in curvature of the interface between phases are decoupled (e.g., diffusion between neighboring grains of the same phase does not affect diffusion across the interface between the two phases) and must independently satisfy the Second Law of Thermodynamics. With these assumptions, (E.16) becomes two relations, one for entropy production due to the interaction of

the two phases across their interface, the other for grains and grain-boundaries within a given phase:

$$-\gamma_1\frac{\widetilde{D}\alpha}{Dt}-\Delta\Pi\frac{\widetilde{D}\phi}{Dt}+\mathfrak{f}_I\overline{\Psi}\ \geqslant\ 0 \tag{E.17a}$$

$$-\sum_i\phi_i\gamma_i\int_0^\infty\frac{\mathfrak{D}_i\breve{\mathcal{A}}_i}{\mathfrak{D}t}v_i d\mathrm{R}+(1-\mathfrak{f}_I)\overline{\Psi}\ \geqslant\ 0 \tag{E.17b}$$

where $\mathfrak{f}_I$ is the partitioning fraction representing how much deformational work goes into work on the interface between phases, i.e., interface "damage"; thus $(1-\mathfrak{f}_I)\overline{\Psi}$ remains to do work on the grain boundaries and generate dissipative heating, and we include the full term in (E.17b) to denote the total work available for grain-damage.

E.3.1. Interface growth and damage

Damage on the interface between phases has been dealt with extensively in two-phase damage theory by Bercovici et al. (2001a), Bercovici and Ricard (2003, 2005) and Ricard and Bercovici (2003) and related papers. However, here we briefly develop the interface damage relations using somewhat more compact non-equilibrium thermodynamics relationships and also for the sake of completeness.

Sans damage. As defined in (A.4), the interface area density is $\alpha=\mathcal{F}\eta(\phi)$ where $\mathcal{F}=1/r$ is the interface fineness (Bercovici and Ricard, 2005), or equivalently the interface curvature; and $\eta(\phi)$ is a function of ϕ that vanishes at $\phi=0$ and $\phi=1$. In the absence of damage and deformational work done on the interface, (E.17a) becomes

$$-\left(\gamma_1\mathcal{F}\frac{d\eta}{d\phi}+\Delta\Pi\right)\frac{\widetilde{D}\phi}{Dt}-\gamma_1\eta\frac{\widetilde{D}\mathcal{F}}{Dt}\ \geqslant\ 0 \tag{E.18}$$

According to the theory of non-equilibrium thermodynamics (de Groot and Mazur, 1984), $\widetilde{D}\phi/Dt$ is a thermodynamic flux (i.e., rate of change of volume fraction) driven by conjugate thermodynamic force of $-(\gamma_1\mathcal{F}d\eta/d\phi+\Delta\Pi)$ (i.e., net pressure drop across the interface squeezing one phase or the other). Likewise, $\widetilde{D}\mathcal{F}/Dt$ is a thermodynamic flux (i.e., rate of change of interface curvature) driven by a conjugate force $-\gamma_1\eta$ (surface tension). The phenomenological laws that guarantee a positive entropy production are

$$\frac{\widetilde{D}\phi}{Dt}=-K_{11}\left(\gamma_1\mathcal{F}\frac{d\eta}{d\phi}+\Delta\Pi\right)-K_{12}\gamma_1\eta \tag{E.19a}$$

$$\frac{\widetilde{D}\mathcal{F}}{Dt}=-K_{12}\left(\gamma_1\mathcal{F}\frac{d\eta}{d\phi}+\Delta\Pi\right)-K_{22}\gamma_1\eta \tag{E.19b}$$

where $\underline{\mathbf{K}}$ is a 2×2 positive definite matrix and by Onsager's reciprocal relations we write $K_{21}=K_{12}$ (since the thermodynamic forces are not explicitly functions of velocity). Using (E.19) and (E.18)becomes

$$K_{11}\left(\gamma_1\mathcal{F}\frac{d\eta}{d\phi}+\Delta\Pi\right)^2+2K_{12}\left(\gamma_1\mathcal{F}\frac{d\eta}{d\phi}+\Delta\Pi\right)\gamma_1\eta+K_{22}(\gamma_1\eta)^2\ \geqslant\ 0 \tag{E.20}$$

The choice of $\underline{\mathbf{K}}$ is non-unique, but the simplest positive definite candidates are either $K_{ij}=k_ik_j$ or $K_{ij}=\kappa_i\delta_{ij}$ where $\kappa_i>0$ The phenomenological laws (E. 19) are likely decoupled because in the equilibrium static limit of $\widetilde{D}(\phi,\mathcal{F})/Dt\to0$, one should recover the Laplace condition for surface tension on an interface, given here by $\gamma_1\mathcal{F}d\eta/d\phi+\Delta\Pi=0$, where $\mathcal{F}d\eta/d\phi=\partial\alpha/\partial\phi$ represents interface curvature (Bercovici et al., 2001a). Decoupling requires that $K_{ij}=\kappa_i\delta_{ij}$, in which case

$$\frac{\widetilde{D}\phi}{Dt}=-\kappa_1\left(\gamma_1\mathcal{F}\frac{d\eta}{d\phi}+\Delta\Pi\right) \tag{E.21a}$$

$$\frac{\widetilde{D}\mathcal{F}}{Dt}=-\kappa_2\gamma_1\eta \tag{E.21b}$$

Eq. (E.21a) states that the phase with the higher pressure tends to expel the other phase, while (E.21b) implies that in the absence of deformation, the interface coarsens with time.

Avec damage. We next restore damage and deformational work to the entropy production, as in (E.17a). However, we assume that damage goes primarily into increasing the interface density α and fineness $\mathcal{F}$, which is equivalent to decreasing r (e.g., breaking or stretching inclusions), and not into creating more volume fraction ϕ. In prior two-phase damage papers (Bercovici et al., 2001a; Bercovici and Ricard, 2003, 2005; Ricard and Bercovici, 2003) damage could be associated with void creation as a representation of microcracking, wherein voids could be filled with a mobile volatile phase (water, melt, air) by Darcy flow. However, here ϕ concerns the volume fraction of another solid silicate phase and thus it is unfeasible for damage to induce voids that are readily filled with a solid silicate. Therefore, an adjustment for damage to the phenomenological laws (E.21) that still satisfies (E.17a) is

$$\frac{\widetilde{D}\phi}{Dt}=-\kappa_1\left(\gamma_1\mathcal{F}\frac{d\eta}{d\phi}+\Delta\Pi\right) \tag{E.22a}$$

$$\frac{\widetilde{D}\mathcal{F}}{Dt}=-\kappa_2\gamma_1\eta+\frac{\mathfrak{f}_I}{\gamma_1\eta}\overline{\Psi} \tag{E.22b}$$

The coefficient $\kappa_1=\mathsf{B}^{-1}$ where B is typically related to the resistance to compaction, i.e., an effective bulk viscosity (McKenzie, 1984; Bercovici et al., 2001a; Ricard et al., 2001; Bercovici and Ricard, 2003); however, given that the two-phases here are both solid silicate, this resistance is effectively infinite, i.e., $\widetilde{D}\phi/Dt\approx0$. Finally using $\mathcal{F}=1/r$, (E.22) becomes

$$\Delta\Pi=-\frac{\gamma_1}{r}\frac{d\eta}{d\phi} \tag{E.23a}$$

$$\frac{\widetilde{D}r}{Dt}=\frac{\eta G_1}{qr^{q-1}}-\frac{\mathfrak{f}_1r^2}{\gamma_1\eta}\overline{\Psi} \tag{E.23b}$$

where (E.23a) is now simply the static (or quasi-static) Laplace condition for surface tension on the interface.

Eq. (E.23b) represents the evolution of interface roughness in which surface tension, or the tendency toward minimum surface energy, acts to coarsen or smooth the interface between the two phases, while deformational work or damage acts to distort or rend the interface.

However, we expect coarsening of the interface not to accelerate the smoother the interface gets. In particular, we preclude finite time singularities in the growth of r; i.e., if κ_2 were constant in r and $r=r_0$ at $t=0$, then $r=r_0/(1-\kappa_2\gamma_1\eta r_0t)$, which is singular at finite t. We have therefore defined $\kappa_2\gamma_1=G_1/(qr^{q+1})$ where $q\geqslant1$ to preclude unphysical growth of r.

It is also reasonable to assume that interface damage is more effective the smaller the interface curvature $1/r$ (e.g., larger inclusions), although the dependence on curvature possibly occurs through $\mathfrak{f}_I$ not merely the factor of r^2, which really arises from writing the growth equation in terms of r instead of fineness $\mathcal{F}$. However, here we assume $\mathfrak{f}_I$ is constant for simplicity and for lack of any evidence to the contrary.

In the end, (E.23b) is the final evolution equation for interface coarseness r, and is displayed in (4d) with the assumption that both phases have the same velocity $\mathbf{v}_i=\mathbf{v}$ such that $\widetilde{D}/Dt=D/Dt$.

E.3.2. Grain growth and damage

The essential physics of grain evolution is contained in the grain-boundary entropy production relation (E.17b), which we rewrite but breaking out the $\mathfrak{D}_i/\mathfrak{D}t$ operator to highlight the continuous and discontinuous population transfer in grain-size space:

$$-\sum_i \phi_i \gamma_i \int_0^\infty \left(\breve{\mathcal{C}}_i \frac{\mathrm{d}_i \breve{\mathrm{V}}}{\mathrm{d}t} v_i + \breve{\mathcal{A}}_i \Gamma_i \right) d\mathrm{R} + (1 - \mathfrak{f}_1)\overline{\Psi} \geqslant 0 \tag{E.24}$$

where we have used (C.5) and (C.7). Again, the first term in the integrand of (E.25a), proportional to v_i, represents continuous or diffusive transfer of mass between neighboring populations of grains of different size by coarsening and the tendency to reduce net grain-boundary surface energy. The second term, proportional to Γ_i, represents discontinuous mass transfer between distal populations due to breaking or fusing of grains.

In the absence of work and damage (i.e., $(1 - \mathfrak{f}_1)\overline{\Psi} = 0$), one can infer linear phenomenological laws from (E.25a) through the formalism of nonequilibrium thermodynamics. Such general laws typically couple the thermodynamics fluxes $d\breve{\mathrm{V}}/dt$ and Γ_i of each grain population of given size R in each phase i to every other grain population and phase. The resulting equations are moderately elucidating but identical to that inferred by Ricard and Bercovici (2009); however the salient points of this exercise can be summarized as follows:

- the law for continuous/diffusive grain-growth recovers Lifshitz-Slysov coarsening theory (Lifshitz and Slyozov, 1961),
- the continuous and discontinuous phenomenological laws can be decoupled,
- the law for Γ_i allows only grain fusion when there is no damage present.

These relations are shown in detail by Ricard and Bercovici (2009) for a single phase, and they are still valid for two phases, assuming the phenomenological laws between phases are decoupled. In the presence of damage, the continuous grain evolution law tends toward homogeneous (single grain-sized) distributions and not necessarily grain-reduction, which Ricard and Bercovici (2009) deemed unphysical. However, damage permits the law for Γ_i to include grain reduction through fission or breakage.

Since the development of these laws is no different than what has been demonstrated in Ricard and Bercovici (2009) we do not repeat it here. Moreover, final integro-differential phenomenological laws are of considerable complexity, which causes them to be of limited utility. Instead, we adopt the simplifying assumptions of the subsequent study by Rozel et al. (2011) to infer a practical and useful set of grain-growth laws for mean grain-size.

Following the findings of Ricard and Bercovici (2009) that damage affects only discontinuous population flux (i.e., Γ_i), we assume that the continuous grain-growth law describes coarsening only and thus satisfies positive entropy production by itself; therefore (E.25a) separates into two relations

$$\sum_i \phi_i \gamma_i \int_0^\infty \breve{\mathcal{C}}_i \frac{\mathrm{d}_i \breve{\mathrm{V}}}{\mathrm{d}t} v_i d\mathrm{R} \leqslant 0 \tag{E.25a}$$

$$\sum_i \phi_i \gamma_i \int_0^\infty \breve{\mathcal{A}}_i \Gamma_i d\mathrm{R} \leqslant (1 - \mathfrak{f}_1)\overline{\Psi} \tag{E.25b}$$

as was also reasoned by Rozel et al. (2011). Along with mass conservation and grain-size distribution laws, (E.25) will comprise the core relations for grain dynamics, as will be discussed in the following section.

Appendix F. Self-similar grain evolution laws

At this point the evolution of interface density α or curvature $1/r$ is reasonably well constrained by (E.23b). However, to complete the evolution law for the grain-size distribution (B.11), we require both $\dot{\mathrm{R}}_i$ (or equivalently $\mathrm{d}_i\breve{\mathrm{V}}/\mathrm{d}t$) and Γ_i. As stated previously, one can formally derive relations for $\dot{\mathrm{R}}_i$ and Γ_i from non-equilibrium thermodynamics, as done in Ricard and Bercovici (2009). However, here we adopt the simpler approach of Rozel et al. (2011) and assume that the grain-size distribution v_i follows a self-similar distribution, wherein the distribution shape is conserved while the distribution moments (e.g., mean, variance, skewness, etc.) as well as amplitude are all defined by a single characteristic grain-size, which evolves with time.

Normal grain-growth or coarsening without deformation or damage follows a self-similar distribution in the limit of very long times, usually in the form of log-normal distributions. As done in Rozel et al. (2011), we assume that v_i retains a nearly self-similar shape even in the presence of damage. Mathematically, we are essentially using a trial function for v_i that is known to be a solution to the system in the absence of damage. There is qualitative justification for using self-similarity in the presence of damage and grain reduction. In the same sense that during coarsening the distribution broadens (increases variance) while its mean-size grows (thus the variance and mean are proportional), the distribution is also expected to narrow (decrease variance) as the mean-size shrinks during damage and grain reduction. In particular, small grains are less susceptible to damage and reduction than are larger grains (i.e., Zener pinning is less effective on smaller grains); thus during grain reduction, the small-grain tail of the distribution propagates to smaller sizes more slowly than the large-grain tail, thereby pinching the distribution as the mean-size diminishes; hence the distribution's mean and variance are both expected to drop simultaneously.

F.1. Summary of equations governing grain evolution

Before proceeding with our self-similar trial function for v_i, we summarize the necessary equations:

- Grain-size evolution is governed by the distribution continuity law (B.11):

$$\frac{D_i v_i}{Dt} + \frac{\partial (v_i \dot{\mathrm{R}}_i)}{\partial \mathrm{R}} = \Gamma_i \tag{F.1}$$

- That grains fill all the volume constrains the distribution v_i to obey (B.4), or

$$\int_0^\infty \breve{\mathrm{V}} v_i d\mathrm{R} = 1 \tag{F.2}$$

- The kinetic laws for $\dot{\mathrm{R}}_i$ (or $\mathrm{d}_i\breve{\mathrm{m}}_i/\mathrm{d}t$) and Γ_i are constrained by mass conservation, leading to (B.19), or

$$\int_0^\infty \frac{\mathrm{d}_i \breve{\mathrm{m}}_i}{\mathrm{d}t} v_i d\mathrm{R} = 0 \tag{F.3a}$$

$$\int_0^\infty \breve{\mathrm{m}}_i \Gamma_i d\mathrm{R} = 0 \tag{F.3b}$$

- Positivity of entropy production on the grain boundary leads to (E.25b), but we further assume entropy production is positive independently in each phase, and thus

$$\gamma_i \int_0^\infty \breve{\mathcal{C}}_i \frac{\mathrm{d}_i \breve{\mathrm{V}}}{\mathrm{d}t} v_i d\mathrm{R} \leqslant 0 \tag{F.4a}$$

$$\gamma_i \int_0^\infty \breve{\mathcal{A}}_i \Gamma_i d\mathrm{R} \leqslant (1 - \mathfrak{f}_1)\Psi_i = (1 - \mathfrak{f}_1) \int_0^\infty \breve{\Psi}_i \breve{\mathrm{V}} v_i d\mathrm{R} \tag{F.4b}$$

where the effective grain boundary area $\breve{\mathcal{A}}_i$ and curvature $\breve{\mathcal{C}}_i$ are given by (C.7) and (C.6), which include grain-boundary distortion effects due to Zener pinning that therefore couple grain growth to interface curvature evolution given by (E.23b)

Eqs. (F.1)-(F.4) are sufficient to construct the grain evolution laws in both phases.

F.2. Self-similar grain evolution

We here follow the arguments of Rozel et al. (2011) and assume not only that the grain-size distribution is self-similar, but that since the terms in (F.1) must have the same spatial symmetry (or else they cannot balance), the self-similar shape of v_i will set the form of $\dot{\mathrm{R}}_i$ and Γ_i as well.

Rozel et al. (2011) considered applications to uniform systems and thus all material time derivatives were equivalent to $\partial/\partial\, t$. Here we assume that variables which are functions of both space $\mathbf{x}$ and time t are only functions of a time variable t following "particles" i.e., infinitesimal control volumes. However, our governing equations involve material derivatives in different frames, i.e., D_i/Dt, which is in the frame of phase i, and $\widetilde{D}/Dt$, which is in the frame of the interface between phases. Given that both phases are solid silicates, we adopt the simplifying assumption that they have the same velocity $\mathbf{v}$ and thus $\mathbf{v}_i = \breve{\mathbf{v}} = \mathbf{v}$; in this case all material derivatives are the same and represented by $D/Dt = \partial/\partial t + \mathbf{v}\cdot\nabla$. We will therefore write that any function $f(\mathrm{R},\mathbf{x},t) = f(\mathrm{R},\mathrm{t})$ where t measures time following a particle at velocity $\mathbf{v}$, and thus $Df/Dt = \partial f/\partial \mathrm{t}$.

A self-similar grain-size distribution is represented by

$$v_i(\mathrm{R},t,\mathbf{x}) = v_i(\mathrm{R},\mathrm{t}) = B(\mathcal{R}_i(\mathrm{t}))H(u) \tag{F.5}$$

where now $u = \mathrm{R}/\mathcal{R}_i$, B is an amplitude that depends only on the time-dependent characteristic mean grain-size $\mathcal{R}_i$ of phase i, and H is a shape function for the distribution (e.g., a log-normal form), which is only a function of the similarity variable u. Here we assume each phase's distribution has a different amplitude, mean grain-size and variance. Strictly speaking, each phase should have separate similarity variables, i.e., u_i instead of u. However, we assume the phase's distributions have the same mathematical shape H and since the form of equations for each phase are the same we denote the similarity variable by the single symbol u for convenience; in the final mean-growth law all instances of the similarity variable vanish anyway.

One can immediately constrain B by using (F.2):

$$\int_0^\infty \breve{\mathrm{V}} v_i d\mathrm{R} = \frac{4}{3}\pi\mathcal{R}_i^4 B(\mathcal{R}_i)\int_0^\infty u^3 H(u)du = 1 \tag{F.6}$$

which implies that

$$B = \frac{3}{4\pi\lambda_3\mathcal{R}_i^4} \tag{F.7}$$

where we define

$$\lambda_n = \int_0^\infty u^n H(u)du \tag{F.8}$$

The form of $\partial v_i/\partial \mathrm{t}$ determines the form of all other terms in (F.1) and this appears as

$$\frac{Dv_i}{Dt} = \frac{\partial v_i}{\partial \mathrm{t}} = -\frac{3}{4\pi\lambda_3\mathcal{R}_i^5}\frac{\mathrm{d}\mathcal{R}_i}{\mathrm{dt}}\frac{1}{u^3}\frac{du^4H}{du} \tag{F.9}$$

as explained in Rozel et al. (2011). Since Γ_i necessarily has the same shape as $\partial v_i/\partial \mathrm{t}$, we write

$$\Gamma_i = \frac{3}{4\pi\lambda_3\mathcal{R}_i^5}D(\mathcal{R}_i)\frac{1}{u^3}\frac{du^4H}{du} \tag{F.10}$$

where $D(\mathcal{R}_i)$ is an as yet to be determined amplitude function of $\mathcal{R}_i$ representing *discontinuous* grain population transfer (Rozel et al., 2011). In a similar fashion, we write that

$$\frac{\partial(\dot{\mathrm{R}}_i v_i)}{\partial \mathrm{R}} = \frac{3}{4\pi\lambda_3\mathcal{R}_i^5}C(\mathcal{R}_i)\frac{1}{u^3}\frac{du^4H}{du} \tag{F.11}$$

which implies, after integration (see Rozel et al., 2011) that

$$\dot{\mathrm{R}}_i = C(\mathcal{R}_i)\left(\frac{b}{H} + u + \frac{3}{H}\int_0^u H(u')du'\right) \tag{F.12}$$

where $C(\mathcal{R}_i)$ is an amplitude function of $\mathcal{R}_i$ representing *continuous* grain population transfer.

In principle the mass conservation relations (F.3) provide constraints on the unknown functions $C(\mathcal{R}_i)$ and $D(\mathcal{R}_i)$ and constant b. However, (F.3b) provides no additional constraints because it is automatically satisfied by (F.10); i.e.,

$$\int_0^\infty \breve{\mathrm{m}}_i \Gamma_i d\mathrm{R} \sim \int_0^\infty \frac{du^4H}{du}du \tag{F.13}$$

which identically equals zero given that $u^4H \to 0$ as $u \to 0$ or ∞ (i.e., a log-normal shaped H converges to 0 at finite u). However, (F.3a) implies that

$$\begin{aligned}\int_0^\infty \frac{\mathrm{d}_i\breve{\mathrm{m}}_i}{\mathrm{dt}} v_i d\mathrm{R} &\sim \int_0^\infty \mathrm{R}^2\dot{\mathrm{R}}_i v_i d\mathrm{R} \\ &\sim \int_0^\infty \left(bu^2 + \frac{d}{du}\left(u^3\int_0^u H(u')du'\right)\right)du = 0\end{aligned} \tag{F.14}$$

which implies

$$b = -3\int_0^\infty H(u')du' \tag{F.15}$$

and thus (F.12) becomes

$$\dot{\mathrm{R}}_i = C(\mathcal{R}_i)\left(u - \frac{3}{H}\int_u^\infty H(u')du'\right) \tag{F.16}$$

as shown already by Rozel et al. (2011).

Since (F.9), (F.10) and (F.12) have the same form according to (F.1), it is not surprising that, when substituted into (F.1), they yield the simple mean-size grain-growth law (see Rozel et al., 2011)

$$\frac{\mathrm{d}\mathcal{R}_i}{\mathrm{dt}} = C(\mathcal{R}_i) - D(\mathcal{R}_i) \tag{F.17}$$

However, the entropy production relations (F.4a) and (F.4b) are needed close the grain-growth relation by constraining the heretofore unknown functions $C(\mathcal{R}_i)$ and $D(\mathcal{R}_i)$.

F.3. Nonequilibrium thermodynamic constraints on C and D

F.3.1. Continuous grain-size evolution and coarsening

Entropy production due to coarsening, as stated in (F.4a) and using (C.6), and (F.16) along with the definition of $v_i = 3H(u)/(4\pi\lambda_3\mathcal{R}_i^4)$, yields

$$\begin{aligned}\int_0^\infty \breve{\mathcal{C}}_i\breve{\mathrm{A}}\dot{\mathrm{R}}_i v_i d\mathrm{R} = \frac{3C(\mathcal{R}_i)}{\lambda_3\mathcal{R}_i^2}\int_0^\infty \left(\frac{2}{u} + \frac{3(1-\phi_i)}{2U}\mathcal{P}(u/U)\right) \\ \times\left(u^3H - 3u^2\int_u^\infty H(u')du'\right)du \leqslant 0\end{aligned} \tag{F.18}$$

where in general $U = r/\mathcal{R}_i$. The first integral, not involving Zener pinning and the function $\mathcal{P}$, can be determined by integration by parts as shown by Rozel et al. (2011), i.e.,

$$\begin{aligned}&2\int_0^\infty \left(u^2H - 3u\int_u^\infty H(u')du'\right)du \\ &= 2\lambda_2 - \left(6\int_0^\infty udu\int_0^\infty H(u')du' - 6\int_0^\infty u\int_0^u Hdu'du\right) \\ &= 2\lambda_2 - \lim_{X\to\infty}\left[3X^2\lambda_0 - 3\int_0^X\left(\frac{d}{du}\left(u^2\int_0^u Hdu'\right) - u^2H\right)du\right] \\ &= 2\lambda_2 - \lim_{X\to\infty}\left(3X^2\lambda_0 - 3X^2\int_0^X Hdu' + 3\int_0^X u^2Hdu\right) = -\lambda_2\end{aligned} \tag{F.19}$$

The integral involving Zener pinning is a function of $U = r/\mathcal{R}_i$ and is proportional to

$$\begin{aligned}\mathcal{I}(U) &= \int_0^\infty \mathcal{P}(u/U)\left(u^3 H - 3u^2\int_u^\infty H(u')du'\right)du \\ &= -\int_0^\infty \mathcal{P}\frac{d}{du}\left(u^3\int_u^\infty H(u')du'\right)du \\ &= -\int_0^\infty \left[\frac{d}{du}\left(\mathcal{P}u^3\int_u^\infty H(u')du'\right) - \frac{d\mathcal{P}}{du}u^3\int_u^\infty H(u')du'\right]du \\ &= \int_0^\infty \frac{d\mathcal{P}}{du}u^3\left(\int_u^\infty H(u')du'\right)du \\ &= \int_0^\infty \left[\frac{d}{du}\left(\int_0^u \frac{d\mathcal{P}}{du'}u'^3du'\int_u^\infty H(u')du'\right) + \int_0^u \frac{d\mathcal{P}}{du'}u'^3du'H(u)\right]du \\ &= \int_0^\infty\int_0^u \frac{d\mathcal{P}(u'/U)}{du'}u'^3du'H(u)du\end{aligned} \tag{F.20}$$

Having sorted out these various integrals, (F.18) eventually becomes

$$\frac{3\lambda_2}{\lambda_3}\frac{C(\mathcal{R}_i)}{\mathcal{R}_i^2}\left(1 - \frac{3(1-\phi_i)}{2\lambda_2}\frac{\mathcal{R}_i}{r}\mathcal{I}(r/\mathcal{R}_i)\right) \geqslant 0 \tag{F.21}$$

which is guaranteed by the linear phenomenological law

$$C(\mathcal{R}_i) = \frac{C^*}{\mathcal{R}_i^2}\mathcal{Z}_i \tag{F.22}$$

where C^* is a positive coefficient and

$$\mathcal{Z}_i = 1 - \frac{3(1-\phi_i)}{2\lambda_2}\frac{\mathcal{R}_i}{r}\mathcal{I}(r/\mathcal{R}_i) \tag{F.23}$$

is the Zener pinning factor. The mathematical form of $\mathcal{Z}_i$ depends on assumptions about $\mathcal{P}$ and hence $\mathcal{I}$, which we will discuss below in Section F.4. However, for monotonically increasing $\mathcal{P}(\mathsf{R}/r)$, $\mathcal{I}$ is a decreasing function of $r/\mathcal{R}_i$ (e.g., see Appendix F.4). In this case, the continuous growth rate (F.16) in phase i is positive for sufficiently small mean grain-size $\mathcal{R}_i$ but approaches zero as the grain-size reaches a limit governed by the interface radius of curvature r, and changes sign if $\mathcal{R}_i$ exceeds this limit. In the limit of no Zener pinning (i.e., either $r \to \infty$ or $\phi_i = 1$) we obtain $\mathcal{Z}_i = 1$ and simple coarsening and grain-growth is recovered.

F.3.2. Discontinuous grain-size evolution and damage

The entropy production due to discontinuous grain evolution in the presence of deformational work and damage is given by (F.4b), which, with (C.7), (C.8) (F.10) and (F.11) becomes

$$\begin{aligned}\gamma_i\int_0^\infty \Gamma_1\breve{\mathcal{A}}_i d\mathsf{R} &= \gamma_i\frac{D(\mathcal{R}_i)}{C(\mathcal{R}_i)}\int_0^\infty \frac{\partial\dot{\mathsf{R}}_i v_i}{\partial\mathsf{R}}\breve{\mathcal{A}}_i d\mathsf{R} \\ &= -\gamma_i\frac{D(\mathcal{R}_i)}{C(\mathcal{R}_i)}\int_0^\infty \dot{\mathsf{R}}_i v_i\frac{\partial\breve{\mathcal{A}}_i}{\partial\mathsf{R}}d\mathsf{R} \\ &= -\gamma_i\frac{D(\mathcal{R}_i)}{C(\mathcal{R}_i)}\int_0^\infty \dot{\mathsf{R}}_i v_i\breve{\mathsf{A}}\breve{\mathcal{C}}_i d\mathsf{R} \leqslant (1-\mathfrak{f}_\mathrm{I})\Psi_i\end{aligned} \tag{F.24}$$

The final integral in (F.24) is the same as in (F.18), thus (F.24) in general becomes

$$3\gamma_i\frac{\lambda_2}{\lambda_3}\frac{D(\mathcal{R}_i)}{\mathcal{R}_i^2}\mathcal{Z}_i \leqslant (1-\mathfrak{f}_\mathrm{I})\Psi_i \tag{F.25}$$

which is satisfied provided

$$D(\mathcal{R}_i) = \frac{\lambda_3}{\lambda_2}\frac{\mathcal{R}_i^2}{3\gamma_i}\frac{\mathfrak{f}_\mathrm{G}(1-\mathfrak{f}_\mathrm{I})\Psi_i}{\mathcal{Z}_i} \tag{F.26}$$

where $\mathfrak{f}_\mathrm{G} \leqslant 1$ and represents a partitioning fraction for deformational work stored on grain boundaries (i.e., work remaining after a fraction $\mathfrak{f}_\mathrm{I}$ is stored on the interface between phase).

F.4. Zener pinning factor

To determine the Zener pinning factor $\mathcal{Z}_i$ we must state a form for $\mathcal{P}$, and there are several possibilities. The monotonically increasing form inferred by Wörner and Cabo (1987) is $\mathcal{P}(\mathsf{R}/r) = \mathcal{P}(u/U) = \mathsf{a} + \mathsf{b}_0\log(u/U)$, where $\mathsf{a} = 0.01$ and $\mathsf{b}_0 = 0.126$. In this case we would obtain $\mathcal{I} = \mathsf{b}_0\lambda_3/3$. For a general power-law relation $\mathcal{P}(u/U) = (\mathsf{b}_\mathsf{n}/\mathsf{n})(u/U)^\mathsf{n}$, we would obtain $\mathcal{I} = \mathsf{b}_\mathsf{n}\lambda_{\mathsf{n}+3}/[(\mathsf{n}+3)U^\mathsf{n}]$. We can thus write a general relation for the Zener pinning factor

$$\mathcal{Z}_i = 1 - c_\mathsf{n}(1-\phi_i)\left(\frac{\mathcal{R}_i}{r}\right)^{\mathsf{n}+1} \quad \text{where} \quad c_\mathsf{n} = \frac{3\mathsf{b}_\mathsf{n}\lambda_{\mathsf{n}+3}}{2(\mathsf{n}+3)\lambda_2} \tag{F.27}$$

in which we use $\mathsf{n} = 0$ to denote the logarithmic $\mathcal{P}$; this relations leads to the general Zener pinning factor displayed in (8).

Although the logarithmic function is based on analysis of the catenoidal shape of a pinned grain boundary, it also applies to pinning by one inclusion on an otherwise pristine boundary, and not on an ensemble of inclusions causing a corrugated or multiply dimpled boundary. The logarithmic function is really only valid for $\mathsf{R} > r$ and is thus both singular as $\mathsf{R} \to 0$ and induces a strong negative Zener pinning force for vanishing grains, when in fact the force should vanish for small grains. Instead we employ a power-law relation that goes to zero for vanishing grain-size R or u, and we constrain it to be tangent to the logarithmic law proposed by Wörner and Cabo (1987). If we use a linear law $\mathsf{n} = 1$, then it leads to $\mathcal{P} = \mathsf{b}_1 u/U$ where $\mathsf{b}_1 = 1/20$. Indeed, as shown in Secion 3, comparison to the experimental data implies that this simple linear $\mathcal{P}$ is best, in which case we obtain

$$\mathcal{Z}_i = 1 - c_1(1-\phi_i)\frac{\mathcal{R}_i^2}{r^2} \tag{F.28}$$

which is the Zener pinning factor used in the simple-shear applications in Section 4.

F.5. Final grain evolution law

The relation for mean grain-size evolution is given simply by (F.17), which can now be closed using the "continuous evolution and coarsening" function $C(\mathcal{R}_i)$ from (F.22) and the "discontinuous evolution and damage" function $D(\mathcal{R}_i)$ from (F.26) finally resulting in

$$\frac{d\mathcal{R}_i}{dt} = \frac{D\mathcal{R}_i}{Dt} = \frac{G_i}{p\mathcal{R}_i^{p-1}}\mathcal{Z}_i - \frac{\lambda_3}{\lambda_2}\frac{\mathcal{R}_i^2}{3\gamma_i}\mathfrak{f}_\mathrm{G}(1-\mathfrak{f}_\mathrm{I})\Psi_i\mathcal{Z}_i^{-1} \tag{F.29}$$

where the Zener pinning factor $\mathcal{Z}_i$ is given by (F.27), or (F.28) for the simple case of $\mathsf{n} = 1$, and we have defined $C^* = G_i/(p\mathcal{R}_i^{p+1})$ where $p \geqslant 1$ to preclude accelerated or singular grain-growth. This power-law assumption is also obtained from simple kinetic assumptions (Lifshitz and Slyozov, 1961; Ricard and Bercovici, 2009) and also what is experimentally observed (Karato et al., 1980; Hiraga et al., 2010). This development thus leads to the final governing equation for mean grain-size shown in (4e).

F.6. Log-normal distribution

As in Rozel et al. (2011) we close the self-similar formulation by assuming a log-normal self-similar distribution wherein

$$H(u) = \frac{1}{\sqrt{2\pi}\sigma u}e^{-(\log u)^2/(2\sigma^2)} \tag{F.30}$$

where σ is a dimensionless variance, and in which case two important integral quantities are

$$\Lambda_n(U) = \int_0^U u^n H(u)du = \frac{1}{2}e^{n^2\sigma^2/2}\left[\mathrm{erf}\left(\frac{\log(U) - n\sigma^2}{\sqrt{2}\sigma}\right) + 1\right] \tag{F.31}$$

and from (F.8)

$$\lambda_n = \Lambda_n(\infty) = e^{n^2\sigma^2/2} \tag{F.32}$$

Rozel et al. (2011) show that, for minerals of geophysical interest (Slotemaker, 2006; Stipp et al., 2010; Hiraga et al., 2010) the variance is constrained by $0.5 \leqslant \sigma \leqslant 1$, but we choose throughout $\sigma = 0.8$, which makes little qualitative difference in the results.

The log-normal distribution $H(u)$ has a mode (i.e., peaks) at $u_M = e^{-\sigma^2}$ and the grainsizes at the half-peak are given by $\mathsf{u}_\pm = u_M e^{\pm\sigma\sqrt{\log(4)}}$. For $\sigma = 0.8$, the mode is at $u_M \approx 1/2$ (i.e., at a grain-size $\mathsf{R} \approx \mathcal{R}_i/2$), and the distribution width at the half-peak is $(\mathsf{u}_+ - \mathsf{u}_-) \approx 2u_M \approx 1$. This half-width is therefore approximately equal to the characteristic mean grain-size $\mathcal{R}_i$, as demonstrated experimentally in Hiraga et al. (2010) (see also the discussion of the experimental grain-size distributions and uncertainties in Section 3.2).

F.7. Grain-size averaged creep laws

Silicate grains undergo a range of possible rheological responses, but for the time-scales and stresses involved with mantle-lithosphere dynamics, diffusion and dislocation creep are the two primary mechanisms of relevance. Within a given grain of size R inside phase i, the constitutive relation is

$$\breve{\underline{\dot{\boldsymbol{\varepsilon}}}}_i = \begin{cases} (a_i \breve{\tau}_i^{n-1})\breve{\underline{\boldsymbol{\tau}}}_i & \text{for } \mathsf{R} \geqslant \mathsf{R}_c \quad \text{(dislocation creep)} \\ (b_i/\mathsf{R}^m)\breve{\underline{\boldsymbol{\tau}}}_i & \text{for } \mathsf{R} \leqslant \mathsf{R}_c \quad \text{(diffusion creep)} \end{cases} \tag{F.33}$$

where $\breve{\underline{\dot{\boldsymbol{\varepsilon}}}}_i$ and $\breve{\underline{\boldsymbol{\tau}}}_i$ are the strain-rate and stress within the grain, $\breve{\tau}_i = \frac{1}{2}\breve{\underline{\boldsymbol{\tau}}}_i : \breve{\underline{\boldsymbol{\tau}}}_i$ is the second invariant of the stress, and the function

$$\mathsf{R}_c(\tau) = \left(\frac{b_i}{a_i \tau^{n-1}}\right)^{1/m} \tag{F.34}$$

defines the transition between the two creep mechanisms. Assuming the stress is the same across all grains within a control volume, so that $\breve{\underline{\boldsymbol{\tau}}}_i = \underline{\boldsymbol{\tau}}_i$, then the average strain-rate is given by

$$\underline{\dot{\boldsymbol{\varepsilon}}}_i = \int_0^\infty \breve{\underline{\dot{\boldsymbol{\varepsilon}}}}_i \breve{\mathrm{V}} v_i d\mathsf{R} = \left[\left(1 - \frac{\Lambda_3(\mathsf{R}_c/\mathcal{R}_i)}{\lambda_3}\right) a_i \tau_i^{n-1} + \frac{\Lambda_{3-m}(\mathsf{R}_c/\mathcal{R}_i)}{\lambda_3} \frac{b_i}{\mathcal{R}_i^m}\right] \underline{\boldsymbol{\tau}}_i \tag{F.35}$$

which represents a mean constitutive relation averaged over the grain-size distribution. The function Λ_n is defined by (F.31), and in particular $\Lambda_n(0) = 0$ and $\Lambda_n(+\infty) = \lambda_n$, and thus the composite rheology (F.35) switches from diffusion to dislocation creep as the average grain size $\mathcal{R}_i$ increases. Therefore accounting for the grain-size distribution in the rheological law allows both mechanisms to exist simultaneously within a sample. While this constitutive law is tractable, it is not analytically invertible, i.e., we cannot use it to write the relation for $\underline{\boldsymbol{\tau}}_i(\underline{\dot{\boldsymbol{\varepsilon}}}_i)$. Rozel et al. (2011) proposed a composite rheology given by

$$\breve{\underline{\dot{\boldsymbol{\varepsilon}}}}_i = (a_i \breve{\tau}_i^{n-1} + b_i/\mathsf{R}^m)\breve{\underline{\boldsymbol{\tau}}}_i \tag{F.36}$$

wherein the mechanism yielding the largest strain-rate dominates. The average strain-rate in this case is simply

$$\underline{\dot{\boldsymbol{\varepsilon}}}_i = \int_0^\infty \breve{\underline{\dot{\boldsymbol{\varepsilon}}}}_i \breve{\mathrm{V}} v_i d\mathsf{R} = \left(a_i \tau_i^{n-1} + \frac{\lambda_{3-m}}{\lambda_3} \frac{b_i}{\mathcal{R}_i^m}\right) \underline{\boldsymbol{\tau}}_i \tag{F.37}$$

which is a good approximation to the actual average rheology (F.35) and thus we adopt it hereafter. In the final governing Eq. (4) we eventually assume that both phases have the same velocity $\mathbf{v}_i = \mathbf{v}$ in which case there is also only one strain-rate $\dot{\boldsymbol{\varepsilon}}$ as given by (6).

Although the medium is assumed to deform according to this composite rheology, dynamic recrystallization theory stipulates that damage to grains only occurs in the fraction of the medium that is deforming by dislocation creep. As shown by (Rozel et al., 2011), this is accomplished by prescribing that the grain-damage partitioning obeys $\mathfrak{f}_{\mathrm{G}} \dot{e}_i = \mathfrak{f}_{\mathrm{G}}^* a_i \tau_i^n$ or that the partitioning fraction is given by

$$\mathfrak{f}_{\mathrm{G}} = \mathfrak{f}_{\mathrm{G}}^* \left(1 + \frac{\lambda_{3-m} b_i}{\lambda_3 a_i \mathcal{R}_i^m \tau_i^{n-1}}\right)^{-1} \tag{F.38}$$

Note that the stress is still determined as a mixture of diffusion and dislocation response for an imposed total strain-rate, but the damage to grains only occurs for the part of the strain-rate undergoing dislocation creep.

Appendix G. Statistical treatment of interface and pinning

G.1. Interface of mixed grains

We can use an idealized mixture of grains of two phases to demonstrate one representation of the interface and its effect on grain growth through pinning. Here we assume the two-phase mixture is made of spherical (or regular polyhedral) grains of each phase and that the interface morphology is only determined by the shape of the grains themselves and some contact fraction between the two phases. This assumption is a simplification since the interface morphology can be determined by more than just mean grain sizes, e.g., by non-spherical interfaces due to grain clumping, stretching or grain-boundary splitting (see Section C.3), in which case the interface 'roughness' r is independent of grain-size. However the statistical mixture method provides one way of quantifying the interface curvature r in terms of grain geometry.

The interface area in a control volume δV is given by $\delta A_{\mathrm{I}} = \int_{\delta V} \alpha dV$ (see also (A.3)) while the total grain boundary area of phase i is given by

$$\delta A_i = \int_{\delta V} \phi_i \left(\int_0^\infty 4\pi \mathsf{R}^2 v_i d\mathsf{R}\right) dV = \int_{\delta V} \phi_i \alpha_i dV \tag{G.1}$$

which defines the grain-boundary area density $\phi_i \alpha_i$. For example, in a distribution of uniform spherical grains $\alpha_i = 3/\mathcal{R}_i$, while using the self-similarity approximation (see Appendix F) $\alpha_i = 3\lambda_2/(\mathcal{R}_i \lambda_3)$, where $\mathcal{R}_i$ is the characteristic grain-size of phase i.

In the statistical mixture formulation, the interface area must be less than or equal to the smaller of the grain boundary areas i.e., $\alpha = \mathfrak{s} \min(\phi_1\alpha_1, \phi_2\alpha_2)$, which we can approximated with the function

$$\alpha = \frac{\mathfrak{s} \prod_i \phi_i \alpha_i}{\left(\sum_i (\phi_i \alpha_i)^{\mathfrak{m}}\right)^{1/\mathfrak{m}}} \tag{G.2}$$

where $\mathfrak{m}$ is a generic exponent. The quantity $\mathfrak{s}$ is the fraction of smaller grain-boundary area that is in contact with the opposite phase (e.g., $\mathfrak{s}$ is small if the grains clump, but approaches unity if they are well dispersed), and is neither constant nor uniform since it evolves as grains are mixed, deformed and damaged. Using the expressions of α_i in term of R_i,

$$\alpha = \frac{3\bar{\mathfrak{s}} \prod_i \phi_i/\mathcal{R}_i}{\left(\sum_i (\phi_i/\mathcal{R}_i)^{\mathfrak{m}}\right)^{1/\mathfrak{m}}} = \frac{3\bar{\mathfrak{s}}\phi_1\phi_2}{\left(\sum_i ((1-\phi_i)\mathcal{R}_i)^{\mathfrak{m}}\right)^{1/\mathfrak{m}}} \tag{G.3}$$

where $\bar{\mathfrak{s}} = \mathfrak{s}$ if the grains have identical radii, and $\bar{\mathfrak{s}} = (\lambda_2/\lambda_3)\mathfrak{s}$ if we use a self-similar distribution.

Using the relation $\alpha = \eta(\phi)/r$ and assuming $\eta = 3\phi_1\phi_2$ (see Appendix A) then the interface radius of curvature would be

$$r = \frac{1}{\bar{\mathfrak{s}}} \left(\sum_i ((1-\phi_i)\mathcal{R}_i)^{\mathfrak{m}}\right)^{1/\mathfrak{m}} \tag{G.4}$$

i.e., the interface radius is some average of each phase radius, times a factor that expresses how well the phases are mixed together. It has the expected behavior in that $r \to \mathcal{R}_i/\bar{\mathfrak{s}}$ if $\phi_i \to 0$, i.e., the interface is dominated by the minor phase; moreover, $r \to \mathcal{R}_i$ if the minor phase is dispersed ($\bar{\mathfrak{s}} \to 1$ and $\phi_i \to 0$) and $r > \mathcal{R}_i$ if these grains clump ($\bar{\mathfrak{s}} \to 0$ and $\phi_i \to 0$). However, while this relation expresses r as a function of phase volume fractions and grain-sizes, it still depends on an independent quantity $\bar{\mathfrak{s}}$ and thus r is an independent quantity itself.

G.2. Zener pinning in mixed grains

G.2.1. Pinning force

The classical Zener pinning force derived for the small inclusions in Section C.1 leading to (C.3) assumes a uniform size distribution of inclusions such that the number density of inclusions available to pin a grain of phase i is simply $(1-\phi_i)\left(\frac{4}{3}\pi r^3\right)^{-1}$. However, if the pinning inclusions are simply other grains of opposite phase j with a non-uniform size distribution v_j, then we must replace the number of grains per unit volume of the pinning phase $\left(\frac{4}{3}\pi r^3\right)^{-1}$ with $v_j(\mathrm{R}')d\mathrm{R}'$ for pinning grains between the sizes of R' and $\mathrm{R}' + d\mathrm{R}'$; after integrating over all pinning grain-sizes the pinning force on one grain of size R becomes

$$F_n(\mathrm{R}) = 2\pi\gamma_i(1-\phi_i)\breve{\mathrm{A}}(\mathrm{R})\mathbb{S}_j \int_0^\infty \mathrm{R}'^2 v_j(\mathrm{R}')\mathcal{P}(\mathrm{R}/\mathrm{R}')d\mathrm{R}' \tag{G.5}$$

where we introduce $\mathbb{S}_j$ where $0 < \mathbb{S}_j \leqslant 1$, to account for the fact that only a fraction of grains of phase j will be available to pin the grain of phase i, for example if phase j grains undergo clumping. If the distribution of inclusions follows a self-similar distribution according to (F.5)–(F.7), and the function $\mathcal{P}(U) = b_1 U$ as implied in Sections 3 and F.4, then this force becomes

$$F_n(\mathrm{R}) = \frac{3\gamma_i(1-\phi_i)\breve{\mathrm{A}}(\mathrm{R})}{2\mathcal{R}_j}\frac{\lambda_1}{\lambda_3}\mathbb{S}_j b_1 \frac{\mathrm{R}}{\mathcal{R}_j} \tag{G.6}$$

which is similar in form to the simple pinning force (2) or (C.3).

G.2.2. Pinning factor

We can use the pinning force (G.6) to infer the energy and shape of a grain boundary in the presence of pinning as in Appendix C.2, which leads to the entropy production relations (E.25) (or equivalently (F.4)). With our generic Zener pinning force (C.3), these entropy production relations suggest a Zener pinning factor $\mathcal{Z}_i$ given by (F.28), as derived in Appendices F.3.1, F.3.2 and F.4. Using the statistical formalism instead, and in particular (G.6), eventually leads to a Zener pinning factor

$$\mathcal{Z}_i = 1 - c_1(1-\phi_i)\mathbb{S}_j\frac{\lambda_1}{\lambda_3}\frac{\mathcal{R}_i^2}{\mathcal{R}_j^2} \tag{G.7}$$

where c_n is still as defined in (F.27). The grain-growth law would be the same as (F.29) but with the Zener pinning factor replaced with (G.7).

G.3. Relation between interface area and pinning

We can demonstrate that the statistical mixture formulation for the interface area described in Appendix G.1 gives a relation for interface pinning radius r that is consistent with the expression for the Zener pinning effect developed in Appendix G.2.

First, the comparison to experiments on synthetic peridotites presented in Section 3 implies grains undergoing static growth or coarsening in each phase eventually reach a pinned state in which they track the growth of the pinning radius r such that the Zener pinning factor $\mathcal{Z}_i \approx 0$. In this case, using (F.28) leads to

$$r^2 \approx c_1(1-\phi_i)\mathcal{R}_i^2 \tag{G.8}$$

which can be recast as

$$r = \sqrt{\sum_i (1-\phi_i)r^2} = \sqrt{c_1\sum_i (1-\phi_i)^2\mathcal{R}_i^2} \tag{G.9}$$

(in Section 3 we used (12) instead, although either relationship is appropriate). The above relation is identical to (G.4) provided that $\mathfrak{m} = 2$ and $\bar{\mathfrak{s}} \to 1/\sqrt{c_1}$ in the pinned state, which demonstrates that expressing interface area and curvature in terms of a statistical mixture of grains is consistent with the pinning physics.

Finally, we can compare the Zener pinning factor expressed in terms of r with that derived by a statistical grain mixture model to constrain the pinning fraction $\mathbb{S}_j$ and show it is related to the grain-sizes, volume fractions and contact fraction $\bar{\mathfrak{s}}$. We use the expression (G.4) for r with $\mathfrak{m} = 2$ and substitute it into the expression for $\mathcal{Z}_i$ given by (F.28); equating this $\mathcal{Z}_i$ to the $\mathcal{Z}_i$ given by (G.7) yields

$$\frac{\bar{\mathfrak{s}}\mathcal{R}_i^2}{\sum_i (1-\phi_i)^2\mathcal{R}_i^2} = \mathbb{S}_j\frac{\lambda_1}{\lambda_3}\frac{\mathcal{R}_i^2}{\mathcal{R}_j^2} \tag{G.10}$$

which implies that

$$\mathbb{S}_j = \bar{\mathfrak{s}}\frac{\lambda_3}{\lambda_1}\frac{\mathcal{R}_j^2}{\sum_i (1-\phi_i)^2\mathcal{R}_i^2} \tag{G.11}$$

This expression for $\mathbb{S}_j$ shows that the availability of secondary phase particles of phase j to pin grains of phase i depends on the contact fraction between phases $\bar{\mathfrak{s}}$ as expected. In particular, when $\phi_j \to 0$, $\mathbb{S}_j = \bar{\mathfrak{s}}\lambda_3/\lambda_1$, which shows that except for a normalizing factor, both $\mathbb{S}_j$ and $\bar{\mathfrak{s}}$ measure the extent of mixing between the two phases.

The statistical representation gives a direct estimate of the pinning size r for a grain mixture of regularly shaped grains. The resulting relations for the interface density and the Zener pinning force are consistent with each other and with the analogous relations that use r directly. Although r can thus be expressed as a function of ϕ_i and $\mathcal{R}_i$, it is still an independent quantity because of its dependence on $\bar{\mathfrak{s}}$. Indeed, the evolution equation for r (see (E.23b) or (4d)) would now become an evolution equation for $\bar{\mathfrak{s}}$ coupled to the evolution equations for $\mathcal{R}_i$ and ϕ_i from the grain-growth and mass conservation laws; i.e., the interface damage equation would now describe how the contact between phases increases through further damage, stretching and mixing.

Appendix H. Approximate analytic solutions for simple shear applications

H.1. Steady state case and effective rheology

Approximate and practical scaling laws for the solutions to the steady state system (29)–(31) and the resulting effective rheology can be obtained with relatively simple assumptions. The numerical solutions indicate that the grain-size evolution is dominated by the Zener pinning factor $\mathcal{Z}_i$ approaching 0, in which case we assume that $\mathcal{R}_i \approx r/\sqrt{\mathrm{h}_i}$ (see the definition of $\mathcal{Z}_i$ in (8) or (F.28) for the case with $\mathrm{n} = 1$, and (18) for the definition of h_i). (This result is due to the grain-damage partitioning factor of $\mathrm{f}_G/\mathrm{f}_G^*$ – see (7) – in (31) becoming very small in the diffusion creep regime, causing the first term in that equation to vanish, which then likewise requires the Zener pinning factor $\mathcal{Z}_i$ that appears in the second term to also vanish.) However we generalize this approximation by assuming that grain-sizes in both phases stay close to the mean size $\overline{\mathcal{R}} = \sum_i \phi_i\mathcal{R}_i \approx \mathrm{c}r$ where $\mathrm{c} = \sum_i \phi_i/\sqrt{\mathrm{h}_i}$ (which is valid so long as ϕ_1 and ϕ_2 do not differ drastically).

We further make approximations about the rheological states in which the system resides. In the large grain limit, which corre-

sponds to lower strain-rates, we assume dislocation creep entirely dominates in which case (29) becomes $\dot{e} \approx \mathfrak{a}_i \bar{\tau}_i^n$; if we take the volume fraction weighted average of this and assume $\tau_i \approx \bar{\tau}$ then we simply arrive at $\dot{e} \approx \bar{\tau}^n$ since $\sum_i \phi_i \mathfrak{a}_i = 1$. In the small grain limit, which corresponds to high strain-rates, we use the assumption that $\mathcal{R}_i \approx \mathfrak{c} r$, and that deformation is dominated by diffusion creep, whence (29) becomes $\dot{e} \approx \mathfrak{b}_i \bar{\tau}_i / \mathcal{R}_i^m$, which, when averaged over volume fraction ϕ_i, becomes $\dot{e} \approx \bar{\tau}/(\mathfrak{c} r)^m$; with this assumption, (30) can be used to infer that

$$\bar{\tau} \approx \left(\frac{1}{2}\mathcal{Q}\mathfrak{c}^{q+1}\right)^{\frac{m}{q+m+1}} \dot{e}^{\frac{q-m+1}{q+m+1}} \tag{H.1}$$

We can compare these scaling laws to the numerical solutions and find they are in remarkable agreement (Fig. H.1). Thus plastic behavior occurs when $q = m - 1$ and shear-localizing behavior occurs when $q < m - 1$.

H.2. Time-dependent case and grain evolution

The fully time-dependent evolution equations (24)–(26) can be solved analytically with assumptions similar to those made for the steady state case discussed in Section H.1. As above we adopt the approximation that $\mathcal{R}_i \approx \mathfrak{c} r$, where $\mathfrak{c} = \sum_i \phi_i / \sqrt{\mathfrak{h}_i}$ and assume the rheologies of phases are not appreciably different such that $\mathfrak{a}_1 = \mathfrak{a}_2 = \mathfrak{a}$ and $\mathfrak{b}_1 = \mathfrak{b}_2 = \mathfrak{b}$ (which, both being normalized are thus unity; but we will retain the symbols for completeness).

For grain-sizes less than the transitional size $\mathcal{R}_c$ (see (32)), i.e., $\mathcal{R}_i < \mathcal{R}_c$, or $r < \mathcal{R}_c/\mathfrak{c} = r_c$, we assume diffusion creep dominates such that stress in either phase approximately obeys $\tau = (\mathfrak{c} r)^m \dot{e}/\mathfrak{b}$, where, for the fixed strain-rate case considered,

$$r_c = \frac{1}{\mathfrak{c}}\left(\frac{\mathfrak{b}}{\mathfrak{a}^{1/n}\dot{e}^{1-1/n}}\right)^{1/m} \tag{H.2}$$

For $r > r_c$ dislocation creep dominates such that $\tau = (\dot{e}/\mathfrak{a})^{1/n}$. In total, (25) becomes

$$\frac{\mathrm{d}r^q}{\mathrm{d}t} = \begin{cases} \varpi\left(\mathcal{Q} - \frac{2\mathfrak{c}^m \dot{e}^2}{\mathfrak{b}} r^{q+m+1}\right) & \text{for } r \leqslant r_c \\ \varpi\left(\mathcal{Q} - \frac{2\dot{e}^{1+1/n}}{\mathfrak{a}^{1/n}} r^{q+1}\right) & \text{for } r \geqslant r_c \end{cases} \tag{H.3}$$

This relation can be condensed into a single equation

$$\frac{\mathrm{d}u}{\mathrm{d}t} = \varpi \kappa^{1/v} \mathcal{Q}^{1-1/v}(1-u^v) \quad \text{where} \quad u = (\kappa/\mathcal{Q})^{1/v} r^q \tag{H.4}$$

and

$$(\kappa, v) = \begin{cases} \left(\frac{2\mathfrak{c}^m \dot{e}^2}{\mathfrak{b}}, \frac{q+m+1}{q}\right) & \text{for } r \leqslant r_c \\ \left(\frac{2\dot{e}^{1+1/n}}{\mathfrak{a}^{1/n}}, \frac{q+1}{q}\right) & \text{for } r \geqslant r_c \end{cases} \tag{H.5}$$

Although (H.4) is integrable, there is only an analytical solution for select values of v. However, for values of $q = 2$ and $m = 3$ one obtains the implicit relations

$$3\varpi\kappa^{1/v}\mathcal{Q}^{1-1/v}t + A = \begin{cases} \log\left(\frac{\sqrt{u^2+u+1}}{u-1}\right) - \sqrt{3}\tan^{-1}\left(\frac{\sqrt{3}}{1+2u}\right) & \text{for } r \leqslant r_c, \quad v = 3 \\ 2\log\left(\frac{\sqrt{u+\sqrt{u}+1}}{\sqrt{u}-1}\right) + 2\sqrt{3}\tan^{-1}\left(\frac{\sqrt{3}}{1+2\sqrt{u}}\right) & \text{for } r \geqslant r_c, \quad v = \frac{3}{2} \end{cases} \tag{H.6}$$

where A is an integration constant. We assume that at time $t = 0$ the interfacial radius of curvature starts at $r = r_o > r_c$, i.e., in the dislocation regime (where $v = 3/2$). The time to reach the transitional radius r_c is

$$t_c = \frac{2}{3\varpi\kappa^{2/3}\mathcal{Q}^{1/3}}\left\{\log\left(\frac{(\sqrt{u_o}-1)\sqrt{u_c+\sqrt{u_c}+1}}{(\sqrt{u_c}-1)\sqrt{u_o+\sqrt{u_o}+1}}\right) + \sqrt{3}\left[\tan^{-1}\left(\frac{\sqrt{3}}{1+2\sqrt{u_c}}\right) - \tan^{-1}\left(\frac{\sqrt{3}}{1+2\sqrt{u_o}}\right)\right]\right\} \tag{H.7}$$

where u_c and u_o correspond to r_o and r_c respectively according to (H.4) with $v = 3/2$. For $t > t_c$ the system follows the diffusion regime solution with $v = 3$ (and with the initial condition that $r = r_c$ at $t = t_c$). The time to reach the steady state $u = 1$ from the transition time t_c is infinity, but the time to reach u_s, where $0 < u_s - 1 \ll 1$ is

$$t_s - t_c = \frac{1}{3\varpi\kappa^{1/3}\mathcal{Q}^{2/3}}\left\{\log\left(\frac{(u_c'-1)\sqrt{u_s^2+u_s+1}}{(u_s-1)\sqrt{u_c'^2+u_c'+1}}\right) - \sqrt{3}\left[\tan^{-1}\left(\frac{\sqrt{3}}{1+2u_s}\right) - \tan^{-1}\left(\frac{\sqrt{3}}{1+2u_c'}\right)\right]\right\} \tag{H.8}$$

where u_c' is the value of u associated with r_c by (H.4) but for $v = 3$ (i.e., u_c' differs from u_c). The total time to reach steady state t_s is the sum of (H.7) and (H.8).

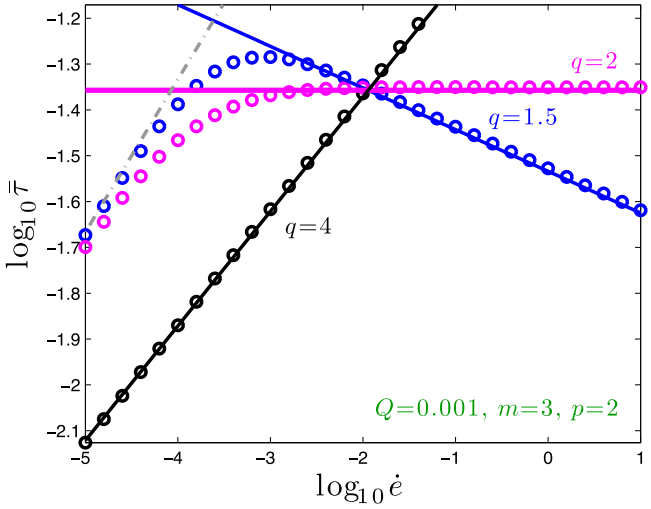

Fig. H.1. Dimensionless effective stress–strain-rate constitutive law similar to the cases shown in Fig. 8bb, solved numerically (circles) and compared to the scaling laws given by (H.1), in which the gray dashed line is the simple dislocation creep limit $\dot{e} \approx \bar{\tau}^n$.

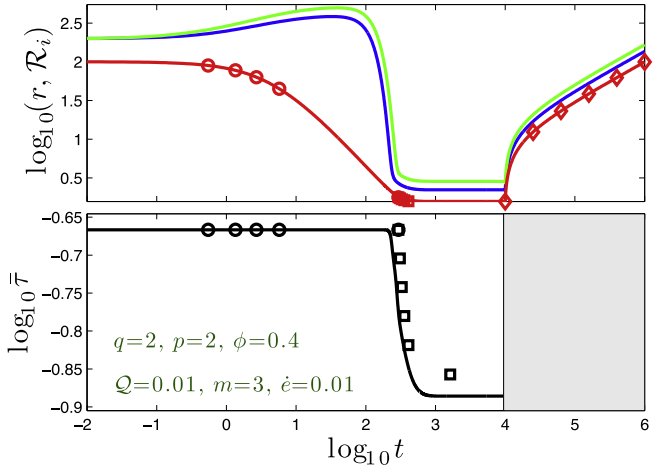

Fig. H.2. Same as Fig. 10a, but for one case (parameters indicated) in comparison to the approximate analytic solution (H.6), shown in symbols. Circles indicate when the system is in dislocation creep, squares indicate when it is in diffusion creep, and diamonds when it is recovering via pure healing, grain-growth and interface coarsening with no damage (i.e., $\dot{e} = 0$).

If deformation ceases at time t_s, then the interface coarsens (r grows) according to

$$r = \left(\varpi \mathcal{Q}(t - t_s) + r_s^q\right)^{1/q} \tag{H.9}$$

where r_s is associated with u_s. The time needed to recover the original state with interface curvature radius r_o after cessation of deformation is given by

$$t_r - t_s = \frac{r_o^q - r_s^q}{\varpi \mathcal{Q}} \tag{H.10}$$

The analytic solutions for $r(t)$ and the predicted mean stress closely match the numerical solutions (Fig. H.2). Thus, the ratio of recovery time $t_r - t_s$ to localization time t_s can be determined from the analytic solutions, as is discussed in Section 4.3 and displayed in Fig. 11.

References

Atkinson, H., 1988. Theories of normal grain growth in pure and single phase systems. Acta Metall. 36, 469–491.

Austin, N., Evans, B., 2007. Paleowattmeters: a scaling relation for dynamically recrystallized grain size. Geology 35, 343–346.

Auth, C., Bercovici, D., Christensen, U., 2003. Two-dimensional convection with a self-lubricating, simple-damage rheology. Geophys. J. Int. 154, 783–800.

Bercovici, D., 1993. A simple model of plate generation from mantle flow. Geophys. J. Int. 114, 635–650.

Bercovici, D., 1995. A source-sink model of the generation of plate tectonics from non-newtonian mantle flow. J. Geophys. Res. 100, 2013–2030.

Bercovici, D., 1998. Generation of plate tectonics from lithosphere-mantle flow and void-volatile self-lubrication. Earth Planet. Sci. Lett. 154, 139–151.

Bercovici, D., 2003. The generation of plate tectonics from mantle convection. Earth Planet. Sci. Lett. 205, 107–121.

Bercovici, D., Karato, S., 2003. Theoretical analysis of shear localization in the lithosphere. In: Karato, S., Wenk, H. (Eds.), Reviews in Mineralogy and Geochemistry: Plastic Deformation of Minerals and Rocks, vol. 51. Min. Soc. Am., Washington, DC, pp. 387–420, Ch. 13.

Bercovici, D., Ricard, Y., 2003. Energetics of a two-phase model of lithospheric damage, shear localization and plate-boundary formation. Geophys. J. Int. 152, 581–596.

Bercovici, D., Ricard, Y., 2005. Tectonic plate generation and two-phase damage: void growth versus grainsize reduction. J. Geophys. Res. 110, B03401. http://dx.doi.org/10.1029/2004JB003181.

Bercovici, D., Ricard, Y., in preparation. Plate generation with two-phase grain-damage and pinning: Source-sink model and toroidal flow. Earth Planet. Sci. Lett.

Bercovici, D., Ricard, Y., Richards, M., 2000. The relation between mantle dynamics and plate tectonics: a primer. In: Richards, M.A., Gordon, R., van der Hilst, R. (Eds.), History and Dynamics of Global Plate Motions, Geophys. Monogr. Ser., vol. 121. Am. Geophys. Union, Washington, DC, pp. 5–46.

Bercovici, D., Ricard, Y., Schubert, G., 2001a. A two-phase model of compaction and damage, 1. General theory. J. Geophys. Res. 106 (B5), 8887–8906.

Bercovici, D., Ricard, Y., Schubert, G., 2001b. A two-phase model of compaction and damage, 3. Applications to shear localization and plate boundary formation. J. Geophys. Res. 106 (B5), 8925–8940.

Braun, J., Chery, J., Poliakov, A., Mainprice, D., Vauchez, A., Tomassi, A., Daignieres, M., 1999. A simple parameterization of strain localization in the ductile regime due to grain size reduction: a case study for olivine. J. Geophys. Res. 104, 25167–25181.

Bridgman, P.W., 1922. Dimensional Analysis. Yale University Press, New Haven, CT.

Charbonneau, D., Berta, Z.K., Irwin, J., Burke, C.J., Nutzman, P., Buchhave, L.A., Lovis, C., Bonfils, X., Latham, D.W., Udry, S., Murray-Clay, R.A., Holman, M.J., Falco, E.E., Winn, J.N., Queloz, D., Pepe, F., Mayor, M., Delfosse, X., Forveille, T., 2009. A super-earth transiting a nearby low-mass star. Nature 462, 891–894.

Couturier, G., Maurice, C., Fortunier, R., 2003. Three-dimensional finite-element simulation of Zener pinning dynamics. Philos. Mag. 83 (30), 3387–3405.

Davies, G., Richards, M., 1992. Mantle convection. J. Geol. 100, 151–206.

De Bresser, J., Peach, C., Reijs, J., Spiers, C., 1998. On dynamic recrystallization during solid state flow: effects of stress and temperature. Geophys. Res. Lett. 25, 3457–3460.

De Bresser, J., ter Heege, J., Spiers, C., 2001. Grain size reduction by dynamic recrystallization: can it result in major rheological weakening? Int. J. Earth Sci. 90, 28–45.

de Groot, S., Mazur, P., 1984. Non-equilibrium Thermodynamics. Dover Publications, New York.

Derby, B., Ashby, M., 1987. On dynamic recrystallization. Scripta Metall. 21, 879–884.

Doherty, R.D., Hughes, D.A., Humphreys, F.J., Jonas, J.J., Jensen, D.J., Kassner, M.E., King, W.E., McNelley, T.R., McQueen, H.J., Rollett, A.D., 1997. Current issues in recrystallization: a review. Mater. Sci. Eng. A 238 (2), 219–274.

Etheridge, M., Wilkie, J., 1979. Grainsize reduction, grain boundary sliding and the flow strength of mylonites. Tectonophysics 58 (1-2), 159–178, microstructural processes during deformation and metamorphism.

Faul, U.H., FitzGerald, J.D., Farla, R.J.M., Ahlefeldt, R., Jackson, I., 2011. Dislocation creep of fine-grained olivine. J. Geophys. Res. 116 (B01203). http://dx.doi.org/10.1029/2009JB007174.

Foley, B., Becker, T., 2009. Generation of plate-like behavior and mantle heterogeneity from a spherical, visco-plastic convection model. Geochem. Geophys. Geosyst. 10, q08001. http://dx.doi.org/10.1029/2009GC002378.

Foley, B.J., Bercovici, D., Landuyt, W., 2012. The conditions for plate tectonics on super-earths: Inferences from convection models with damage. Earth Planet Sci. Lett. 331–332, 281–290.

Furusho, M., Kanagawa, K., 1999. Reaction induced strain localization in a lherzolite mylonite from the hidaka metamorphic belt of central Hokkaido, Japan. Tectonophysics 313, 411–432.

Ganesan, S., Poirier, D.R., 1990. Conservation of mass and momentum for the flow of interdendritic liquid during solidification. Metall. Trans. B 21, 173–181.

Gordon, R., 2000. Diffuse oceanic plate boundaries: strain rates, vertically averaged rheology, and comparisons with narrow plate boundaries and stable interiors. In: Richards, M.A., Gordon, R., van der Hilst, R. (Eds.), History and Dynamics of Global Plate Motions, Geophys. Monogr. Ser, Vol. 121. Am. Geophys. Union, Washington, D.C, pp. 143–159.

Gurnis, M., Zhong, S., Toth, J., 2000. On the competing roles of fault reactivation and brittle failure in generating plate tectonics from mantle convection. In: Richards, M.A., Gordon, R., van der Hilst, R. (Eds.), History and Dynamics of Global Plate Motions, Geophys. Monogr. Ser, vol. 121. Am. Geophys. Union, Washington, DC, pp. 73–94.

Hager, B., O'Connell, R., 1979. Kinematic models of large-scale flow in the earth's mantle. J. Geophys. Res. 84, 1031–1048.

Hager, B., O'Connell, R., 1981. A simple global model of plate dynamics and mantle convection. J. Geophys. Res. 86, 4843–4867.

Hall, C.E., Gurnis, M., Sdrolias, M., Lavier, L.L., Mueller, R.D., 2003. Catastrophic initiation of subduction following forced convergence across fracture zones. Earth Planet. Sci. Lett 212, 15–30.

Harun, A., Holm, E.A., Clode, M.P., Miodownik, M.A., 2006. On computer simulation methods to model Zener pinning. Acta Mater. 54 (12), 3261–3273.

Hellman, P., Hillert, M., 1975. Effect of second-phase particles on grain growth. Scand. J. Metall. 4 (5), 211–219.

Herwegh, M., Berger, A., Ebert, A., 2005. Grain coarsening maps: a new tool to predict microfabric evolution of polymineralic rocks. Geology 33 (10), 801–804.

Hilairet, N., Reynard, B., Wang, Y., Daniel, I., Merkel, S., Nishiyama, N., Petitgirard, S., 2007. High-pressure creep of serpentine, interseismic deformation, and initiation of subduction. Science 318 (5858), 1910–1913.

Hillert, M., 1965. On the theory of normal and abnormal grain growth. Acta Metall. 13, 227–238.

Hillert, M., 1988. Inhibition of grain growth by second-phase particles. Acta Metall. 36 (12), 3177–3181.

Hiraga, T., Tachibana, C., Ohashi, N., Sano, S., 2010. Grain growth systematics for forsterite ± enstatite aggregates: effect of lithology on grain size in the upper mantle. Earth Planet. Sci. Lett. 291, 10–20.

Hirth, G., Kohlstedt, D., 1996. Water in the oceanic upper mantle: implications for rheology, melt extraction and the evolution of the lithosphere. Earth Planet. Sci. Lett. 144, 93–108.

Hirth, G., Kohlstedt, D., 2003. Rheology of the upper mantle and the mantle wedge: a view from the experimentalists. In: Eiler, J. (Ed.), Subduction Factor Mongraph, vol. 138. Am. Geophys. Union, Washington, DC, pp. 83–105.

Holyoke, Caleb, W.I., Tullis, J., 2006. Formation and maintenance of shear zones. Geology 34 (2), 105–108.

Jin, D., Karato, S., Obata, M., 1998. Mechanisms of shear localization in the continental lithosphere: inference from the deformation microstructures of peridotites from the Ivrea zone, northwestern Italy. J. Struct. Geol. 20, 195–209.

Kameyama, M., Yuen, D., Fujimoto, H., 1997. The interaction of viscous heating with grain-size dependent rheology in the formation of localized slip zones. Geophys. Res. Lett. 24, 2523–2526.

Karato, S., 1989. Grain growth kinetics in olivine aggregates. Tectonophysics 168, 255–273.

Karato, S., Toriumi, M., Fujii, T., 1980. Dynamic recrystallization of olivine single crystals during high temperature creep. Geophys. Res. Lett. 7, 649–652.

Katz, R.F., 2008. Magma dynamics with the enthalpy method: benchmark solutions and magmatic focusing at mid-ocean ridges. J. Petrol. 49 (12), 2099–2121.

Kaula, W., 1980. Material properties for mantle convection consistent with observed surface fields. J. Geophys. Res. 85, 7031–7044.

Korenaga, J., 2007. Thermal cracking and the deep hydration of oceanic lithosphere: a key to the generation of plate tectonics? J. Geophys. Res. 112. http://dx.doi.org/10.1029/2006JB004502.

Korenaga, J., 2010. On the likelihood of plate tectonics on super-earths: does size matter? Astrophys. J. Lett. 725 (1), L43–L46.

Landuyt, W., Bercovici, D., 2009a. Formation and structure of lithospheric shear zones with damage. Phys. Earth Planet. Int.. http://dx.doi.org/10.1016/j.pepi.2009.03.005.

Landuyt, W., Bercovici, D., 2009b. Variations in planetary convective via the effect of climate on damage. Earth Planet. Sci. Lett. 277, 29–37.

Landuyt, W., Bercovici, D., Ricard, Y., 2008. Plate generation and two-phase damage theory in a model of mantle convection. Geophys. J. Int. 174, 1065–1080.

Lebrun, J.-F., Lamarche, G., Collot, J.-Y., 2003. Subduction initiation at a strike-slip plate boundary: the cenozoic Pacific-Australian plate boundary, south of New Zealand. J. Geophys. Res. 108, 2453. http://dx.doi.org/10.1029/2002JB002041.

Lee, K., Jiang, Z., Karato, S., 2002. A scanning electron microscope study of effects of dynamic recrystallization on the lattice preferred orientation in olivine. Tectonophysics 351, 331–341.

Lenardic, A., Jellinek, M., Moresi, L.-N., 2008. A climate change induced transition in the tectonic style of a terrestrial planet. Earth Planet. Sci. Lett. 271, 34–42.

Lenardic, A., Kaula, W., 1994. Self-lubricated mantle convection: two-dimensional models. Geophys. Res. Lett. 21, 1707–1710.

Lifshitz, I., Slyozov, V.V., 1961. The kinetics of precipitation from supersaturated solid solutions. J. Phys. Chem. Solids 19, 35–50.

Manohar, P., Ferry, M., Chandra, T., 1998. Five decades of the zener equation. ISIJ Int. 38 (9), 913–924.

Martin, W., Baross, J., Kelley, D., Russell, M.J., 2008. Hydrothermal vents and the origin of life. Nat. Rev. Microbiol. 6 (11), 805–814.

McKenzie, D., 1984. The generation and compaction of partially molten rock. J. Petrol. 25, 713–765.

McKenzie, D., 1985. The extraction of magma from the crust and mantle. Earth Planet. Sci. Lett. 74, 81–91.

McKenzie, D., 1987. The compaction of igneous and sedimentary rocks. J. Geol. Soc. Lond. 144, 299–307.

McKenzie, D., Holness, M., 2000. Local deformation in compacting flows: development of pressure shadows. Earth Planet. Sci. Lett. 180, 169–184.

Mehl, L., Hirth, G., 2008. Plagioclase preferred orientation in layered mylonites: evaluation of flow laws for the lower crust. J. Geophys. Res. 113 (B05202). http://dx.doi.org/10.1029/2007JB005075.

Montési, L., Hirth, G., 2003. Grain size evolution and the rheology of ductile shear zones: from laboratory experiments to postseismic creep. Earth Planet. Sci. Lett. 211, 97–110.

O'Neill, C., Lenardic, A., 2007. Geological consequences of super-sized earths. Geophys. Res. Lett. 34, 19204–19208.

Ricard, Y., Bercovici, D., 2003. Two-phase damage theory and crustal rock failure: the theoretical 'void' limit, and the prediction of experimental data. Geophys. J. Int. 155, 1057–1064.

Ricard, Y., Bercovici, D., 2009. A continuum theory of grain size evolution and damage. J. Geophys. Res. 114, B01204. http://dx.doi.org/10.1029/2007JB005491.

Ricard, Y., Bercovici, D., Schubert, G., 2001. A two-phase model of compaction and damage, 2. Applications to compaction, deformation, and the role of interfacial surface tension. J. Geophys, Res. 106 (B5), 8907–8924.

Ricard, Y., Vigny, C., 1989. Mantle dynamics with induced plate tectonics. J. Geophys. Res. 94, 17543–17559.

Richards, M., Yang, W.-S., Baumgardner, J., Bunge, H.-P., 2001. Role of a low-viscosity zone in stabilizing plate tectonics: Implications for comparative terrestrial planetology. Geochem. Geophys. Geosyst. 2, 2000GC000115.

Rios, P., 1987. Overview No. 62: a theory for grain boundary pinning by particles. Acta Metall. 35 (12), 2805–2814.

Roberts, C., 2008. Grain Growth and The Zener Pinning Phenomenon: A Computational and Experimental Investigation. Ph.D. thesis, Carnegie Mellon University.

Rozel, A., Ricard, Y., Bercovici, D., 2011. A thermodynamically self-consistent damage equation for grain size evolution during dynamic recrystallization. Geophys. J. Int. 184 (2), 719–728.

Shimizu, I., 1998. Stress and temperature dependence of recrystallized grain size: a subgrain misorientation model. Geophys. Res. Lett. 25, 4237–4240.

Skemer, P., Warren, J.M., Kelemen, P.B., Hirth, G., 2009. Microstructural and rheological evolution of a mantle shear zone. J. Petrol.. http://dx.doi.org/10.1093/petrology/egp057.

Slotemaker, A.K., 2006. Dynamic Recrystallization and Grain Growth in Olivine Rocks. Ph.D. thesis, Utrecht Universiteit.

Smith, C.S., 1948. Grains, phases, and interfaces: an interpretation of microstructure. Trans. AIME 175, 15–51.

Solomatov, V., El-Khozondar, R., Tikare, V., 2002. Grain size in the lower mantle: constraints from numerical modeling of grain growth in two-phase systems. Phys. Earth Planet. Int. 129, 265–282.

Southam, G., Westall, F., 2007. Geology, life and habitability. In: Tilman Spohn (Gerald Schubert, Ed.-in-Chief) (Ed.), Treatise on Geophysics, Planets & Moons, vol. 10. Elsevier, Amsterdam, pp. 421–437.

Spiegelman, M., 1993a. Flow in deformable porous media, part 1, simple analysis. J. Fluid Mech. 247, 17–38.

Spiegelman, M., 1993b. Flow in deformable porous media, part 2, numerical analysis – the relationship between shock waves and solitary waves. J. Fluid Mech. 247, 39–63.

Spiegelman, M., 1993c. Physics of melt extraction: theory, implications and applications. Philos. Trans. R. Soc. Lond., Ser. A 342, 23–41.

Stein, C., Schmalzl, J., Hansen, U., 2004. The effect of rheological parameters on plate behaviour in a self-consistent model of mantle convection. Phys. Earth Planet. Int. 142, 225–255.

Stipp, M., Tullis, J., Scherwath, M., Berhman, J., 2010. A new perspective on paleopiezometry: dynamically recrystallized grain size distributions indicate mechanism changes. Geology 38 (8), 759–762.

Tackley, P., 1998. Self-consistent generation of tectonic plates in three-dimensional mantle convection. Earth Planet. Sci. Lett. 157, 9–22.

Tackley, P., 2000a. The quest for self-consistent generation of plate tectonics in mantle convection models. In: Richards, M.A., Gordon, R., van der Hilst, R. (Eds.), History and Dynamics of Global Plate Motions, Geophys. Monogr. Ser, vol. 121. Am. Geophys. Union, Washington, DC, pp. 47–72.

Tackley, P., 2000b. Self-consistent generation of tectonic plates in time-dependent, three-dimensional mantle convection simulations, 1. Pseudoplastic yielding. Geochem. Geophys. Geosyst. 1, 2000GC000036.

Tackley, P., 2000c. Self-consistent generation of tectonic plates in time-dependent, three-dimensional mantle convection simulations, 2. Strain weakening and asthenosphere. Geochem. Geophys. Geosyst. 1, 2000GC000043.

Toth, G., Gurnis, M., 1998. Dynamics of subduction initiation at preexisting fault zones. J. Geophys. Res. 103, 18053–18067.

Tozer, D., 1985. Heat transfer and planetary evolution. Geophys. Surv. 7, 213–246.

Trompert, R., Hansen, U., 1998. Mantle convection simulations with rheologies that generate plate-like behavior. Nature 395, 686–689.

Urai, J., Means, W., Lister, G., 1986. Dynamic recrystallization in minerals. In: Hobbs, B., Heard, H. (Eds.), Mineral and Rock Deformation: Laboratory Studies. Am. Geophys. Union, Washington, DC, pp. 166–199.

Valencia, D., O'Connell, R., Sasselov, D., 2007. Inevitability of plate tectonics on super-earths. Astrophys. J. 670, L45–L48.

Valencia, D., O'Connell, R.J., 2009. Convection scaling and subduction on earth and super-earths. Earth Planet. Sci. Lett. 286 (3-4), 492–502.

van Heck, H., Tackley, P., 2008. Planforms of self-consistently generated plates in 3d spherical geometry. Geophys. Res. Lett. 35, L19312. http://dx.doi.org/10.1029/2008GL035190.

van Heck, H., Tackley, P., 2011. Plate tectonics on super-earths: equally or more likely than on earth. Earth Planet. Sci. Lett. 310 (3–4), 252–261.

Vigny, C., Ricard, Y., Froidevaux, C., 1991. The driving mechanism of plate tectonics. Tectonophysics 187, 345–360.

Voorhees, P.W., 1992. Ostwald ripening of two-phase mixtures. Ann. Rev. Mater. Sci. 22, 197–215.

Walker, J., Hayes, P., Kasting, J., 1981. A negative feedback mechanism for the long-term stabilization of Earth's surface temperature. J. Geophys. Res. 86, 9776–9782.

Warren, J.M., Hirth, G., 2006. Grain size sensitive deformation mechanisms in naturally deformed peridotites. Earth Planet. Sci. Lett. 248 (1-2), 438–450.

White, S., Burrows, S., Carreras, J., Shaw, N., Humphreys, F., 1980. On mylonites in ductile shear zones. J. Struct. Geol. 2, 175–187.

Wörner, C., Cabo, A., 1987. On the grain growth inhibition by second phases particles. Acta Metall. 35 (11), 2801–2804.